Cardiff University

Design and Implementation of Multi-Port DC-DC Converters for Electrical Power Systems

By

Emad Alhani

Ph.D.

A thesis submitted in accordance with the requirements for the award of the degree of Doctor of Philosophy of the Cardiff University
May 2023

Supervised by:

Dr. Fatih Anayi

Declaration

I certify that this thesis has never been submitted before for a degree, nor has it been considered for another degree or qualification at another university. My thesis consists of my work and includes no collaboration results except where specifically indicated.

Emad Alhani

2023

Acknowledgements

The greatest praise goes to Allah (God), who has given me the wisdom, health, and patience to accomplish this task.

With the deepest gratitude, I would like to extend my best wishes to my primary supervisor, Dr. Fatih Anayi, for the outstanding guidance, intellectual support, and encouragement he provided throughout my graduate studies. Throughout my time studying under Dr. Fatih Anayi, I have learned a great deal academically and personally. The comments and advice you provided regarding my research, as well as my life and career, were invaluable. Additionally, I wish to thank my second supervisor, Dr. Yevgen Melikhov, for his generous support and academic guidance.

My sincere thanks go out to the many people who have contributed to the success of this research and thesis. The author would like to thank Libya's higher education ministry. Without their funding, this work would not have been possible. Thanks to them for their financial support and the invaluable PhD Scholarship.

It is also highly appreciated that the academic and technical support staff within the school helped with the construction of the equipment used for the experimental work, as well as the design of the printed circuit boards. Thanks are due to the Postgraduate Research Coordinator and the other administrative staff members.

It is my deepest wish to express my heartfelt appreciation to my mum, who has always supported and encouraged me throughout my life and my academic pursuits. Thank you to all my family members and relatives who have inspired and motivated me.

Abstract

The thesis proposes developing, analysing, and verifying these DC-DC converters to improve the current state-of-the-art topology. Four new DC-DC converters for applications like light emitting diode, lighting microgrids DC, PV applications, and electric vehicles are as follows.

In this study, the two-input converter is presented. The two-input converter that has been proposed serves as the interface between the two input sources and load. Using two switches and two diodes, the proposed converter minimises switching losses and contains eight components in total, making it compact and low volume. As a result, the highest average efficiency is 92.5%, and the lowest is 89.6%.

In this research, the new three-port converter that has been proposed serves as the interface between the input source, a battery, and a load. In addition, the converter is suitable for use in standalone systems or satellite applications. A low-volume converter is designed with three switches and two diodes, thereby minimizing switching losses and ten components in total. Regarding efficiency, the highest average is 92.5%, and the lowest is 90.9%.

Also, this study proposes a single-switch high-step-up converter for LED drivers and PV applications. A further benefit of the proposed converter over conventional classical converters is that it utilises only one active switch. These results align with simulation results, and its gain is 6.8 times greater than classical converters. Furthermore, stress across switches and diodes is smaller than the output voltage, approximately 50%. Semiconductor losses were limited with a low duty cycle of 0.7. This makes the highest average efficiency 95% and the lowest 93.9%.

The new four-port converter is presented for applications such as microgrid structures and electric vehicles. As part of the integrated converter, two or three converters are combined by sharing some components, such as switches, inductors, and capacitors, to form a single integrated converter. As a result of the four-port converter proposed, battery power can be managed, and output voltage can be regulated simultaneously.

Table of Contents

List of Figures

List of Tables

Abbreviation

AC	Alternating Current
BTU	British Thermal Units
CCM	Continuous Conduction Mode
CDSs	CubeSat Design Specifications
DC	Direct Current
DCM	Discontinuous Conduction Mode
DI	Dual-Input
DIDO	Dual-Input Dual-Output
DIM	Dual Input Mode
DISO	Dual-Input Single-Output
DMPPT	Distributed Maximum Power Point Tracking
DO	Dual Output
DOM	Dual Output Mode
DPG	Distributed Power Generation
EPS	Electrical Power System
ESS	Energy Storage Systems
EV	Electric Vehicle
FB-TPC	Full-Bridge Three-Port Converter
FF	Fill Factor
FOC	Fraction Open Circuit
FSC	Fraction Short Circuit
HEV	Hybrid Electric Vehicle
HIDs	High-Intensity Discharge Lamps
HVDC	High Voltage Direct Current
KCL	Kirchhoff's Current Law

KVL	Kirchhoff’s Voltage Law
LED	Light-Emitting-Diode
LEO	Low Earth Orbit
MIMO	Multi-Input Multi-Output
MMCs	Modular Multilevel Converters
MOSFET	Metal Oxide Semiconductor Field Effect Transistor
MPC	Multiport Converter
MPPT	Maximum Power Point Tracking
OCC	One-Cycle Control
OCFs	Open-Crcuit Faults
P&O	Perturb and Observe
PCB	Printed Circuit Board
PFC	Power Factor Correction
PFM	Pulse-Frequency Modulation
PI	Proportional Integral
PSC	Partial Shading Condition
PV	Photovoltaics
RES	Renewable Energy Sources
SC	Supercapacitor
SCFs	Short-Crcuit Faults.
SIDO	Single-Input Dual-Output
SISO	Single-Input Single-Output
SITO	Single-Input Triple-Output
SoC	State of Charge
SSPS	Secondary-Side Phase-Shift
STC	Standard Testing Condition (nominal condition)
TPC	Three-Port Converter

TPHBC	Three-Port Half-Bridge Converter
TPHBC-PF	Three-Port Half-Bridge Converter with Primary Freewheeling
TPHBC-PR	Three-Port Half-Bridge Converter with Post Regulation
TPHBC-SR	Three-port Half-Bridge Converter Synchronous Regulation
UPSs	Uninterruptible Power Supply System

Chapter 1 Introduction

1.1 Background for Satellite Applications

The growing cost of launching spacecraft into space, around \$100k/kg, is a key driver of efforts to reduce the mass and weight of its electrical system. In the case of the international space station, the solar panels per kilowatt cost would be over \$3M/kW, presuming a mass of 1000 kg of the solar panel and starting power of 32 kW [1]. Thus, a satellite platform's cost heavily depends on its mass. Additionally, it is commonly accepted that the electrical system of the satellite platform accounts for about 25% of its total dry mass and 35% when the user power system is included [2]. The mass of the space power system is a significant design constraint.

Solar arrays, batteries, and an interface Power Conditioning Unit (PCU) make up the satellite platform power system. In Low Earth Orbit (LEO) applications, the PCU connects the solar arrays and the batteries to a distribution bus, typically 28V. Upon delivery, the system provides power to various user loads, including propulsion, altitude control, and data handling. Throughout the satellite's operational life, the solar arrays produce the electrical power during solar insolation and supply the power necessary to provide the satellite's bus, which supplies power to the payload. The solar arrays mentioned above are costly and heavy; consequently, one of the biggest challenges is transforming solar energy.

The conversion of solar energy normally involves two steps. In the first step, solar energy must be converted into uncontrolled electrical energy. Solar array materials have a strong bearing on the efficiency and mass of electricity, and the increasing efficiency depends on material engineering, which is beyond the scope of power electronics research. An electronic circuit or interface is then used to transform the power into a controllable and usable electrical power that can drive a distribution bus in the second step. In the second conversion step, power electronics engineers are responsible for developing smart solutions to achieve low mass and high-efficiency power management.

According to Fig.1.1, different conditions of operation lead to different nonlinear terminal characteristics of solar arrays are illustrated. A point on every I-V curve for certain irradiance levels and temperatures produces the maximum power. This point represents maximum power. Nevertheless, this point constantly fluctuates according to variations in irradiance, temperature, and other environmental conditions. To achieve maximum solar power harvesting, there is a need to install a power electronics interface that can change the PV's load characteristics and force the PV system to follow this optimum path.

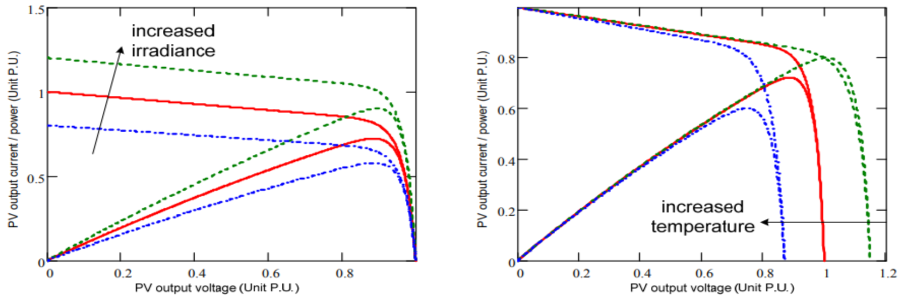

(a) **(b)**

Fig 1.1 An illustration of the terminal I-V characteristics of a solar array, (a) variations in irradiance, and (b) variations in temperature [2].

Maximum Power Point Tracking (MPPT) for the PV arrays in the satellite PCU is very important in missions where the solar intensity changes dramatically. Due to the decrease in the overall mass of the power system, MPPT is advantageous when a smaller solar array is required to manage a given power budget requirement. Additionally, a bus that has been regulated rather than unregulated will enable a more efficient design of payload converters with less mass and volume by impacting the filtering and derating of power components. Therefore, the mass of the converter itself may also be reduced. Hence, MPPT and bus regulation can potentially reduce the total mass of satellite power systems.

In contrast, during pre-launch operations, the launch phase, eclipse periods, and when the solar array output is insufficient, the battery will provide electric power to the satellite. To extend the battery's service life, overcharge and over-discharge protection are essential. Therefore, satellite power systems should always have battery protection.

On the other hand, in the traditional satellite power system architectures illustrated by Fig.1.2, MPPT is normally achieved by using multiple independent converters for solar panels, battery charging and discharging control, and bus regulation. However, control complexity and conversion steps are increased. As a result of the added complexity, size, weight, cost, and decrease in reliability, as well as increased losses associated with such architectures, their wide adoption has been slow. Despite its potential profitability, MPPT technologies have difficulty being justified because the mass of MPPT regulators and control is complex. This dissertation proposes a single conversion stage to maintain a regulated distribution bus while achieving MPPT and battery regulation efficiently, as shown in Fig.1.3. Power processing components and control tasks integrated into the three-port converter reduce the size, weight, complexity, and cost-effective, which makes it an ideal choice for satellite power systems.

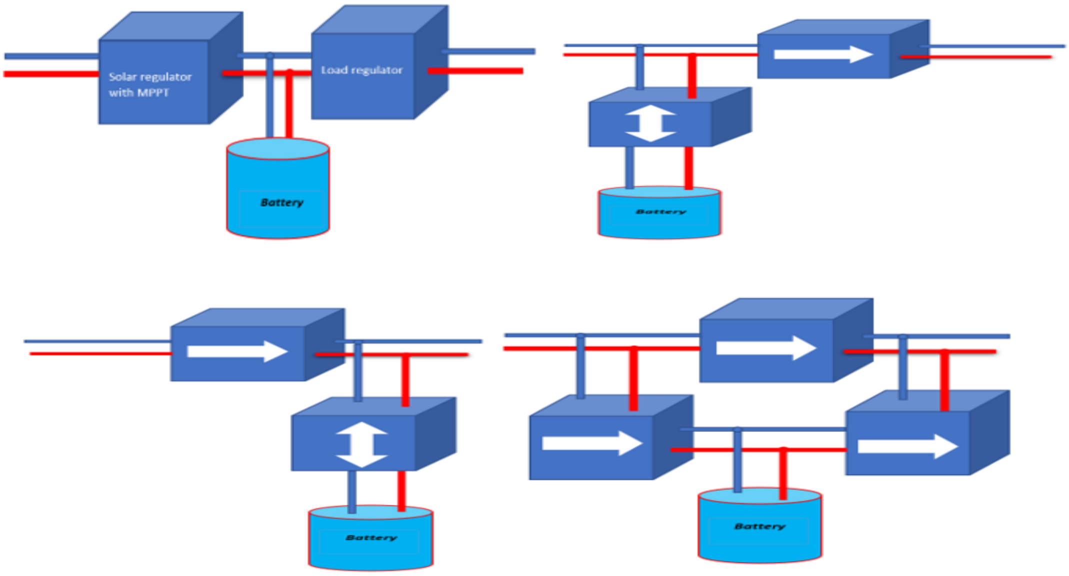

Fig 1.2 Satellite platform power converter solutions [2].

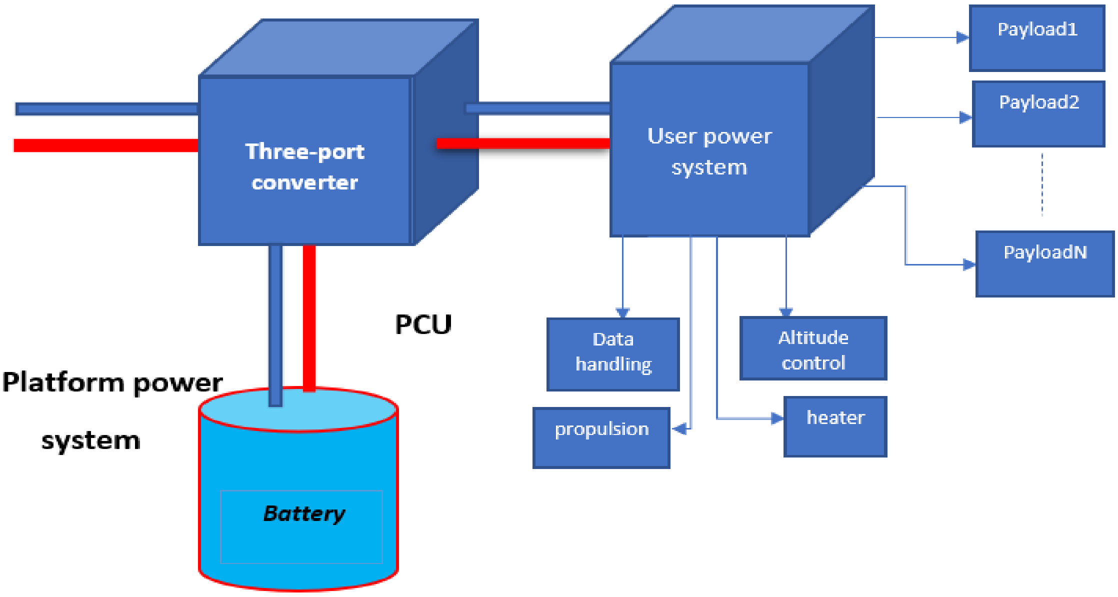

Fig 1.3 Solar panels and batteries supply platform power, while various user loads sink platform power [2].

1.2 Nanosatellite Technology

Nanosatellite technology has attracted significant interest in recent years. Academic and industrial space communities have become increasingly interested in nanosatellites. In contrast to traditional and sophisticated satellites, they are less expensive and require less time to develop. However, they may be able to perform space technology demonstrations. Due to the miniaturization of satellite technology, space communities are increasingly interested in developing small spacecraft missions based on CubeSat standards [3]. In addition to providing easy access to space, they are also an excellent alternative for several space research and educational projects such as solar sails [4], Earth observation [5] and tether experiments, as they have a relatively low-cost budget, can be implemented rapidly and can be launched from one deployment unit for a relatively inexpensive launch. To ensure the success of the Nanosat mission, it must provide sufficient power to each subsystem, both during daylight and during eclipses, by utilizing the battery cells for power storage. In addition, this power should be sufficient to meet the requirements of the subsystem. The ability to achieve all these objectives depends on the proper design of the nanosatellite Electrical Power System (EPS).

Generally, CubeSats belong to the pico-to-nano class of satellites. These satellites are designed and constructed according to a specific set of standards on advanced capabilities and functionality as outlined in the mission's CubeSat Design Specifications (CDS). As shown in Fig. 1.4 1U, 2U, 3U, and 6U CubeSat mechanical layouts are illustrated and compared [3].

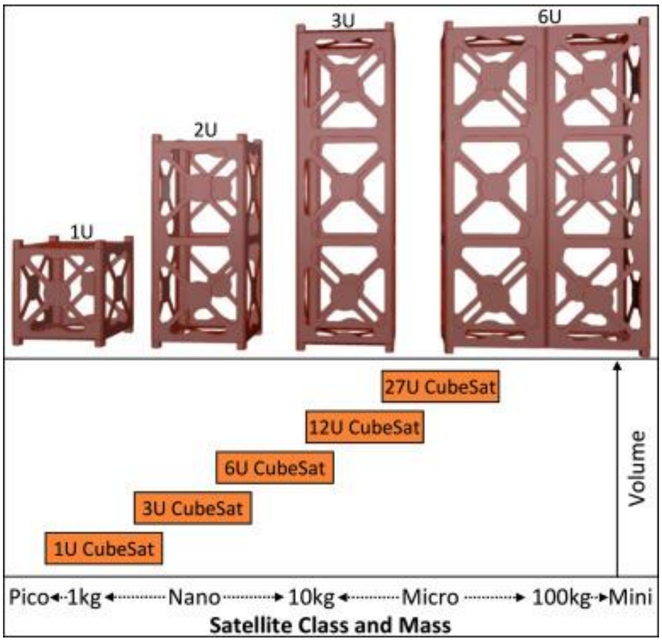

Fig 1.4 CubeSat specifications in the framework of overall small satellite classifications [3].

As described in Fig. 1.4, an industry-standard 1U unit consists of a 10 cm cube ($10x10x10\ cm^3$) weighing up to 1.33 kg. There are two ways in which a 1U CubeSat can be used: either as a standalone satellite or in conjunction with other CubeSats to form a larger satellite. Due to the great success of small CubeSats such as the 1U and 3U units, an advanced standard for larger CubeSats (6U, 12U and 27U) was proposed to enable much greater CubeSat capabilities [6]. The CubeSat standard uses mass and volume to classify small satellites instead of the usual classification of small satellites based only on their mass. A comparison of the CubeSat standard with a generally accepted classification for small satellites is presented in Fig. 1.4.

1.3 Background for PV applications

Many academics and industry representatives have expressed an interest in power DC-DC converters in the last few decades due to the significant improvement in power electronics. In today's era of modern power conversion systems, DC-DC converters are essential components of almost every application, ranging from low-power applications such as Light-Emitting Diode (LED) drivers to high-power applications such as grid-connected inverters [7]–[10], motor drive [11] and Distributed Power Generation (DPG) system [12].

DC-DC converters have indeed been developed over a prolonged period of time, but complex problems still exist, and related research is still under development in depth and breadth. As part of this thesis, we focus on improving the topology design of DC-DC converters to improve their performance by enhancing voltage conversion ratio, power efficiency, reliability, and cost.

As part of the power conversion stage of many applications powered by renewable energy sources, a high-efficiency, high step-up DC-DC converter is required. As an example, grid-connected inverters [7]–[10] and High-Intensity Discharge lamps (HIDs) [13], electric drives [14] and Uninterruptible Power Supply Systems (UPSs) [15],[16] are common examples. Here is a brief description of some emerging applications that require high-step-up DC-DC power converters that will be discussed in more detail in the following sections.

1.1.1 Grid Connected Photovoltaic Inverter

Solar Photovoltaic (PV) technology is one of the most important aspects of renewable energy, especially in countries that make good use of solar radiation and have a high level of electricity production. A stand-alone system or one connected to the grid could be used for the application. During 2014, PV grid-connected power systems grew by 1.9 gigawatts in Germany, 2.4 gigawatts in the United Kingdom, and 0.9 and 0.4 GW in France and Italy, respectively. During the same period, Japan, China, and the United States have added 9,7, 10.6, and 6.2 gigawatts, respectively. Consequently, this adds a further 177 GW to the total global installed capacity [17] currently in use. A typical grid-connected PV power system is shown in Fig.1.5 below.

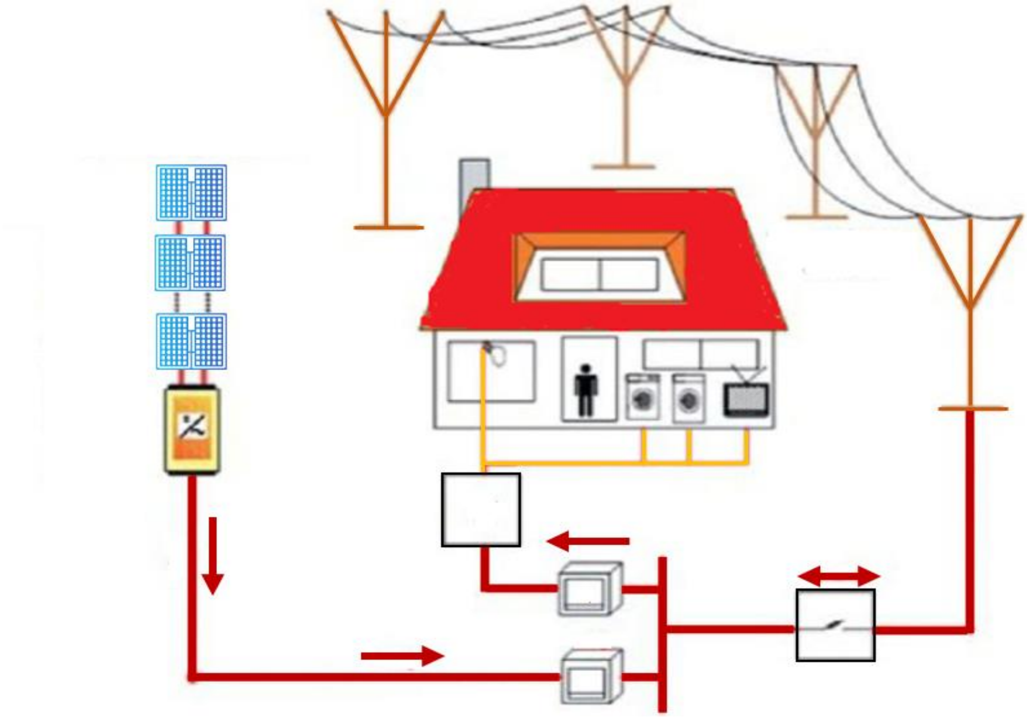

Fig 1.5 Renewable energy system connected to the single-phase grid [17].

Typically, PV panels are connected in series with a power converter to obtain a DC link voltage that can be used to track the PV's Maximum Power Point (MPP) range to calculate the final power. In the case of partial shading, or when there is a mismatch between shading and MPP, there is a significant increase in MPP losses. Alternately, another configuration is to use a modular approach to increase the MPPT efficiency of the system and reduce costs by using independent DC-DC converters for each PV panel. In this case, each module is equipped with a DC-DC converter integrated into it. In this way, every panel can be configured differently, and the output power can be optimized by decoupling them. Despite this, having two power electronic converters in this topology is common. It is necessary to use a stepping-up boost converter for the first conversion stage to raise the relatively low DC voltage from the solar panel to a certain level that can be synthesised for the alternating current AC line voltage, which in most cases is 380 - 400 V_{DC}. Another type of converter is the DC-AC inverter, which injects sinusoidal currents into the grid. Using high-step-up DC-DC converters, a Maximum Power Point Tracking (MPPT) algorithm is implemented to stabilise the voltage level on the DC bus, providing the PV array with maximum efficiency. Undoubtedly, the quality of the DC-DC converter at the core of the solar photovoltaic system plays a vital role in the overall performance of the solar system since the DC-DC converter is the key component that interfaces the solar PV system with the DC-AC inverter and enhances its functionality.

An important drawback of a grid-connected power system is that the system contributes to the grid only a portion of the power added to the grid by using solar energy, which is only available during daylight hours on a daily basis. To overcome this problem, photovoltaic inverter systems usually employ an energy storage system, such as a battery, which can improve the system's performance and provide reliability for the power supply [18]. Using the ESS, it is attempting to provide a backup function so that solar energy can be transferred to the ESS during sunny periods. When solar energy is unavailable at night, the ESS delivers energy to the DC bus. This results in providing the grid with stable and fast-response AC power. An integrated grid-connected PV system that incorporates ESS can be achieved using a bidirectional DC-DC converter (boost and buck) to switch power flow in both directions (forwards and reverses) during power transfer.

1.3.1 LED Driver

Since LEDs feature several advantages such as high-power density, high luminous efficiency, long lifespan, mercury-free, and rapid response, they have enormous potential as replacements for conventional lamps in residential, automotive, decorative, and medical applications [19],[20]. In order to achieve high illuminance in the application scenarios, LEDs are used in numerous quantities. There is a need for a high output voltage level when LEDs are connected in series. Because of the LEDs' current-voltage characteristic and the negative coefficient of temperature for parallel-connected LEDs, it is necessary to implement the current balancing technology to regulate the current through the different LED strings [21]. There is a need for a boost voltage level of around 300 V for LED strings that are powered by 24 V batteries or PV panels for LED applications. Due to this, LED drivers need high voltage converters since they usually have a high voltage conversion ratio.

1.3.2 EV

To tackle air pollution, the British government will ban all new sales of petrol and diesel cars by 2030 to curtail the risk of serious health issues due to air pollution [22]. The secondary objective of automotive companies such as BWM, Mercedes-Benz, Ford, and BYD is to meet the market demand for vehicles by offering Electric Vehicles (EV), Hybrid Electric Vehicles (HEV), and fuel cell vehicles. There is still a significant technical challenge involved in the design of power DC-DC converters of high efficiency, low cost, and small volume. The fuel cell vehicle drive system shown in Fig.1.6 can be considered a typical one. Boosting the low fuel cell voltage needed to power the electric motors requires high step-up DC-DC converters, which are an indispensable component. In most cases, the fuel cell is boosted to a voltage level of 200~400V and is compatible with the battery pack when used correctly [23]. The second installation phase is installing the inverter that drives the electric motor.

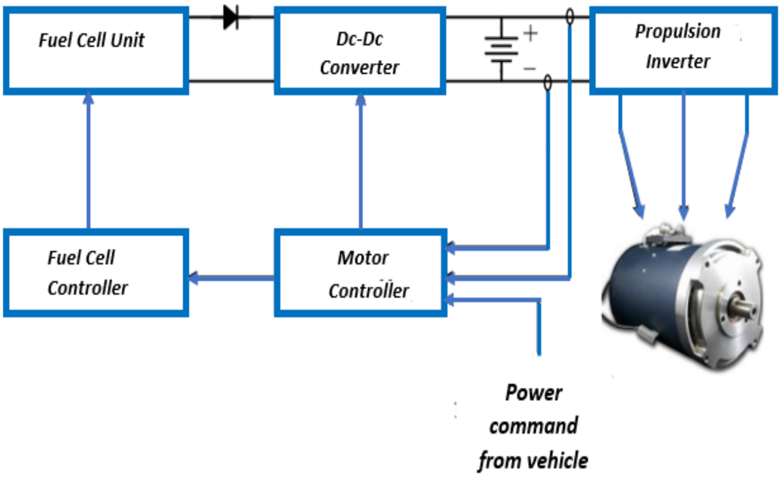

Fig 1.6 The drive train of an electric vehicle [22].

1.3.3 High Intensity Discharge (HID) Lamp

Due to the superior performance and numerous advantages of High-Intensity Discharge (HID) lamps, they are preferable for using automobile headlamps instead of conventional halogen lamps, such as higher performance, longer life, better light beam focus, and better colour rendering capabilities than conventional halogen lamps. Although the HID lamp is capable of delivering significant advantages, when it comes to the actual operation, it is similar to the other discharge lamps. It is required to be controlled by ballast to maintain steady state power when it operates. There is a typical ballast circuit in Fig.1.7 which can be used to ignite a lamp and power it at the same time.

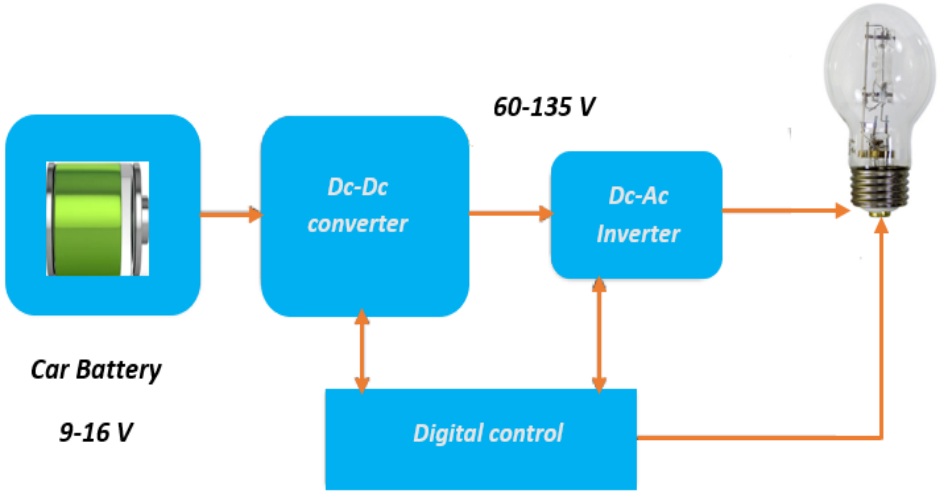

Fig 1.7 Block diagram of a high intensity discharge lamp ballast.

The ballast has three components: a high step-up DC-DC converter, an inverter, and an igniter. There are various sources of powering HIDs, such as the automobile battery, which provides a much lower voltage input than the voltage for which the ballast is designed to operate. Thus, to provide the extra step-up power required in the solar ballast, a DC-DC converter with high step-up capabilities must be installed in the ballast to provide the battery voltage at (380 V-400 V) during starting up and at (60-135 V) during steady-state operation. Due to these factors, it is crucial that a high-quality step-up DC-DC converter may be used on the lamp that can produce a tenfold gain in voltage.

1.1.2 Uninterruptible Power Supply UPS

To protect sensitive loads from outages, an Uninterruptible Power Supply (UPS) is increasingly used to supply power to them during outages on the utility power grid under normal or abnormal conditions [15],[16]. As a result of UPSs having long been used for providing seamless power to a wide range of critical loads, such as medical equipment, communication systems, computers, and servers, UPSs have gained in popularity. Any UPS utilises DC-DC power electronics converters to interface different power sources and loads to regulate the voltage. Regarding UPS topology, it includes a Power Factor Correction (PFC) circuit, which usually consists of a front-end AC-DC converter that converts the AC-line voltage ($90-265\ Vrms$). Inverters, to operate properly, require a regulated DC link voltage of (380 - 400 V), provided by this supply. The UPS is designed to act as a backup power source in case of a mains failure or utility outage. The UPS can power the load from the battery backup powered by 48 V. To raise the voltage of the battery bank to that required by the DC bus, and it is necessary to use a high step-up converter.

1.2 Outline of Thesis

This dissertation will be outlined in the following manner.

In chapter 1, an overview of the Multi-Port Converter used in applications such as satellite platform power systems is presented in chapter one. As a result of its reduced component count and fewer conversion stages than traditional architectures with several independent converters, the Multi-Port Converter can reduce mass and increase efficiency in space applications. Moreover, the chapter briefly introduces the traditional converters that can be used in various applications, such as those related to high step-up conversions, light drivers, Uninterruptible Power Supplies (UPS), Electric Vehicles (EVs), etc.

In chapter 2, a review of the literature related to Multi-Port Converters is presented. Three types of converters are discussed in the literature review: isolated, non-isolated, and partially isolated. This chapter compares these converters to select the most suitable topology to integrate PV with an energy storage system. Moreover, a literature review will provide an overview of current state-of-the-art methods of developing step-up boost converters as a first step to defining the work. There are several challenges related to non-isolated DC-DC boost converters. A simplified circuit, lower cost, and higher efficiency system platform are proposed.

Chapter 3 proposes a new non-isolated DC-DC converter for PV grid-connected power generation systems, integrating two input sources. In addition to the traditional advantages of Multi-Port Converters (MPCs), the proposed design has many other advantages, including using one-stage conversion, fewer components, and a low operation duty ratio. Even under changing and unpredictable output demands, the converter continuously supplies the load and regulates the output voltage. The converter can supply the load and regulating the output voltage. A laboratory prototype has been developed to validate the theoretical analysis, and experimental results have been provided.

Chapter 4 proposes a new non-isolated Three-Port DC-DC Converter for standalone and space applications that integrate battery storage and an input source. Aside from the traditional benefits of Multi-Port Converters MPC, this circuit incorporates one-stage conversion, resulting in fewer components. The converter continuously supplies the load for standalone systems and regulates the output voltage by managing the power flow between the ports. The converter can supply the load and always regulate the output voltage. Experimental results have been presented to validate the theoretical analysis.

In chapter 5, a new high-step converter employs two topologies that share the same switch, which is suitable for LED drivers and PV applications. There is also a description of how the topology is developed. The design of the converter is validated through simulation. Furthermore, to verify the operational principles, experimental test results of a prototype are presented.

Chapter 6 proposes a novel Four-Port Converter suitable for renewable energy applications. Furthermore, the topology implements a single-stage energy conversion, as well as sharing a common reference ground between inputs and outputs. In addition, the operation of the circuit and its topology are described first. Due to independent duty cycle values, the input current and output voltage are tightly regulated. Control systems are designed based on the pole placement method, which is useful in MIMO converters. A detailed analysis of the four-port converter is presented, and the design of the converter is validated through simulation.

In chapter 7, conclusions, and future works. A summary of the entire study and a discussion of how well the objectives and research aim have been achieved. It also suggests potential areas for further investigation based on the study's findings.

1.3 The aim and objectives

Power electronics converters are key for interfacing and conditioning many applications' source and load power levels.

This research aims to develop integrated single-stage power converter structures that allow interface and control of multiple power sources and storage devices while improving overall system functionality.

The main objectives and research contributions are:

- To develop a new high step-up DC-DC converter topology benefits many applications, though the focus here is on domestic solar PV applications and LED drivers.
- To develop Two-Input Converter for various applications, such as DMPPT PV applications, DC motor drive systems, and LED drivers.
- To propose and develop a Three-Port DC-DC Converter since it can provide high efficiency, and several components are shared. The proposed converter has many applications, such as satellite applications, DC motor drive systems, and LED drivers.
- To develop a Multi-Input-Multi-Output topology. This topology is proposed for microgrids, electric vehicles, and satellite applications with battery backups.

1.4 Contribution to knowledge

This thesis is primarily composed of four contributions. Firstly in chapter 3, a novel non-isolated Two-Input DC-DC Converter for PV grid-connected power generation systems was proposed. This design offers many advantages over traditional Multi-Port Converters (MPCs), such as using one-stage conversion and fewer components. Secondly, in chapter 4, a new Three-Port DC-DC Converter with integrated battery storage and an input source for space applications was proposed. Additionally, this circuit incorporates one-stage conversion, reducing component count. By managing the power flow between the ports, the converter continuously supplies the load and regulates the output voltage. Thirdly chapter 5 proposes a new non-isolated DC-DC converter for

LED driving and PV applications. An important characteristic of this converter topology is the integration of Luo and Cuk DC-DC converters. Using a single power semiconductor switch, the proposed topology reduces voltage stress across diodes and power semiconductor switches while maintaining a continuous input current. In addition, this topology has the advantage of extending the static voltage gain compared to a conventional boost converter. Lastly, chapter 6 proposes a novel Four-Port Converter suitable for renewable energy applications, including electric Vehicles, DC microgrids, and space applications. Besides that, the topology implements a single-stage energy conversion and has a common ground for inputs and outputs.

1.5 Limitations of Work Undertaken

This work focused on developing new type of DC-DC converters, which has a combination of properties that make it unique compared to existing DC-DC converter topologies. The limitations of the work undertaken can be broadly considered as follow:

The proposed converters have been analysed in steady-state CCM operation, and their efficiencies have been calculated. For any DC-DC converters, the performance could be characterised in other ways, including their performances under unbalanced conditions. In addition, thermal studies and stability analysis and their transient performances must be investigated with closed-loop voltage and current controllers.

1.6 Publications Arising from this Research

The research work carried out in this thesis has resulted in following journal papers:

- Alhani E**,** Anayi F, Melikhov Y,“Integrated Three-Port DC/DC Converter for Different Applications.” Submitted for peer review in: IEEE access Journal.

- Alhani E**,** Anayi F, “The design of a hybrid DC/DC converter for LED lighting systems using a single switch” Submitted for peer review in: Energy Reports Journal.

- Alhani E**,** Anayi F, “Not-isolated DC/DC converter with multiple inputs and one output for photovoltaic power generation systems” Submitted for peer review in: Energy Reports Journal.

Chapter 2 A Literature Review Multiport Power Converters

2.1 Introduction

Recent years have seen a rise in the popularity of renewable energy sources such as solar energy due to their clean, environmentally friendly nature and abundance in nature [24] The downside of solar energy is that they are intermittent, and they are not generally reliable. It is necessary to use power electronic converters to connect these sources to the load to solve this problem. With the aid of these power converters, renewable energy sources can be tracked for maximum power. The electrical power system can be managed for a satellite system. T renewable energy sources can be interfaced with the energy storage system [25] to store energy for eclipse and peak demand and distribute the power effectively to load. Conventional connecting an energy source with a load involves a single DC-DC converter with two ports [26],[27]. It is necessary to have two or more power converters if more than one input power source or Energy Storage System (ESS) will be used, as shown in Fig.2.1. These power converters can be either connected to a power source, which means they are producing unidirectional power flow, or they can be connected to the ESS in which case they are producing a bidirectional power flow. Because these converters are normally cascaded, it will increase the cost, the complexity of the system, the number of components, and a reduction in system efficiency [28], [29].

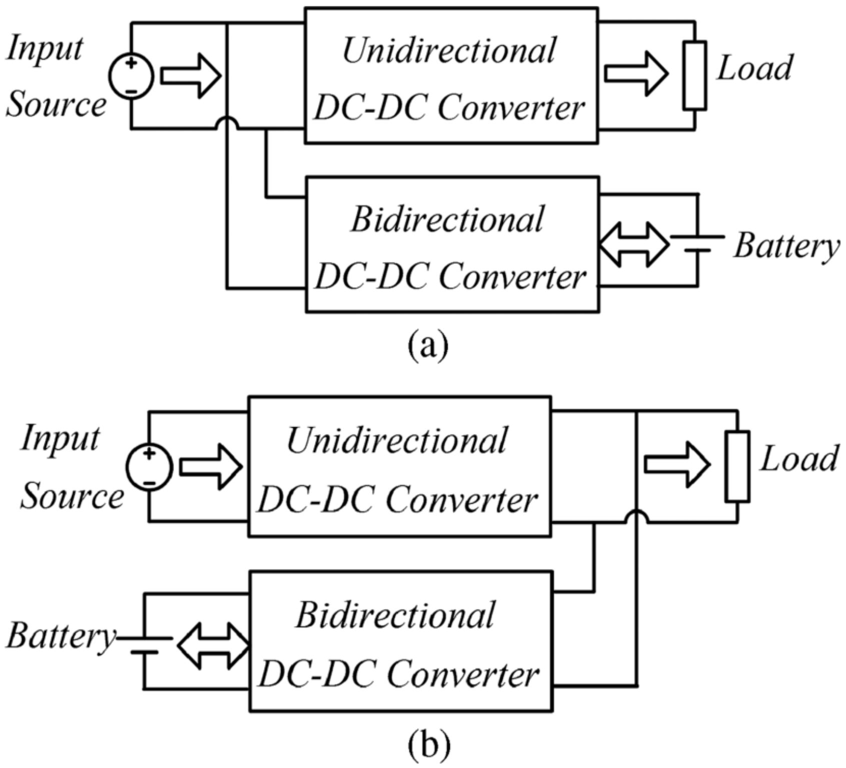

Fig 2.1 Traditional multiport connection in a standalone power system: (a) Multi-Input ports. (b) Multi-output.

Compared to single-port converters, multi-port converters, and especially three-port converters, as shown in Fig.2.2, can provide a better design and implementation experience, which is especially useful for renewable energy systems, electric vehicles, aerospace applications, and DC distribution power systems [30],[31]. Due to this fact, multi-port converters offer some advantages compared to single-port converters, including reducing the cost and mass of the system and improving power density by sharing components such as switches, capacitors, etc., and storage elements [32],[33]. As well as increasing the system's reliability, it uses central control, which reduces the number of communication channels required, causing no communication delays or errors in the process. A multiport converter is also an excellent way to improve the dynamic performance of the system by enabling multiple inputs and multiple outputs (MIMO) [30],[34].

$$P_O = P_{in} + P_{BAT} \tag{2.1}$$

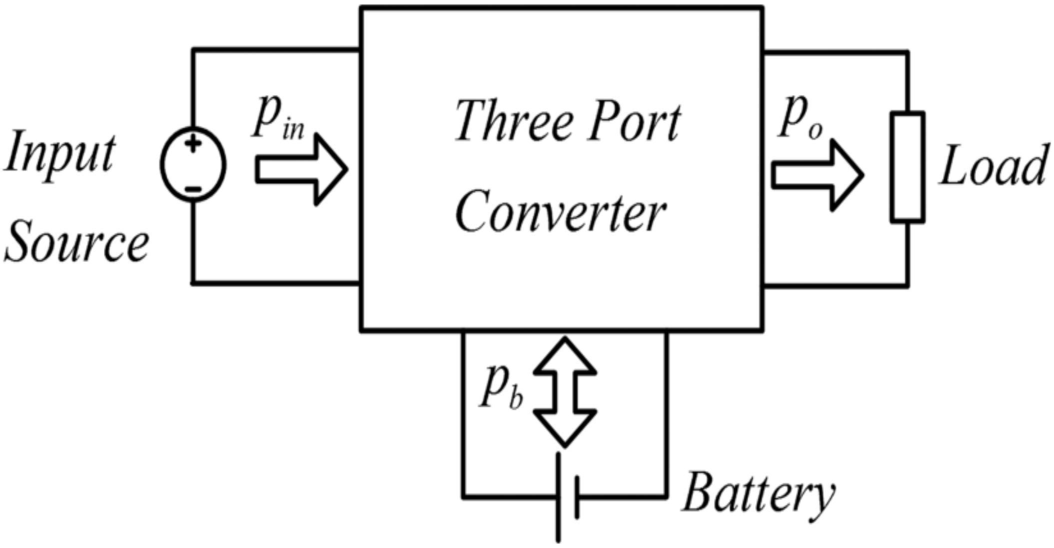

Fig 2.2 Three-port converter TPC.

There are three main ways in which multi-port converters can be expressed in (2.1), and these can be categorised according to their operation mode into three types, Single-Input Single-Output conversion (SISO), Single-Input Dual-Output conversion (SIDO), and Dual-Input Single-Output conversion (DISO). If only two ports are active, and the power at each port is equal, SISO mode is present. During SIDO mode, some generated power will be transferred to the storage element if the input power exceeds the output power. In DISO, some power is supplied to a load when the input power exceeds the demand.

The Multi-Port Converter (MPC) has been proposed in several papers over the last few years [34]–[48]. A Three-Port Converter (TPC) has three ports and is the most common type of MPC, is a Three-Port Converter (TPC). Three categories of MPC can be distinguished: non-isolated converters, isolated converters, and partly isolated converters.

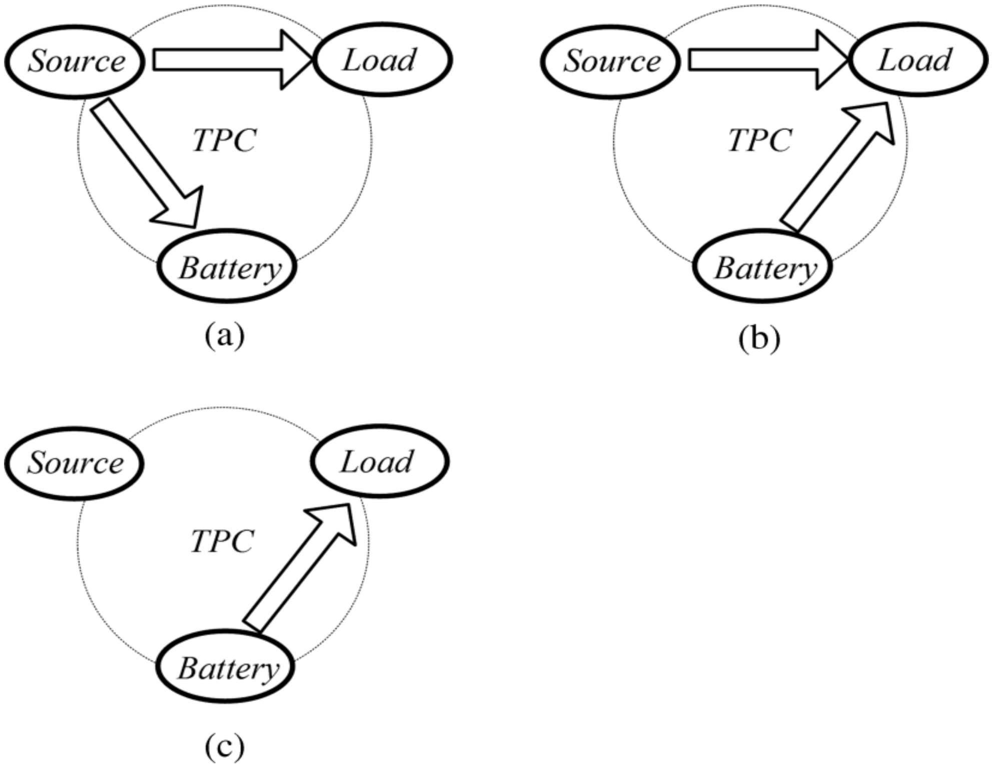

Fig 2.3 The general configuration of a renewable energy generation system using a three-port converter: (a) SISO mode. (b) SIDO mode. (c) DISO mode.

TPC can be divided into three categories, as shown in Fig.2.4 below. Each category has a level of complexity, number of components, reliability, and power ratio. As part of this chapter, the most recent MPC will be reviewed; this review is meant to aid in selecting the most suitable topology for each application.

2.1.1 Non-Isolated Multiport Converter

When the isolation feature between the ports of the power converter is not required in some applications, a non-isolated power converter is used. There are some benefits associated with this type of topology, such as its low cost, high-power density, and high efficiency [49]. As a result of this topology, all ports share the same ground, and all are directly connected. Due to this reason, it is referred to as non-isolated. Furthermore, this topology has the disadvantage that the voltage gain between the ports is not particularly high. Consequently, multi-stage converters may be used in some situations when high voltage gains are required [50]. Generally, the non-isolated multiport converters proposed in the literature are based on various standard DC-DC converters, including buck, boost, buck/boost, Cuk, SEPIC, and Zeta converters, which are well-known.

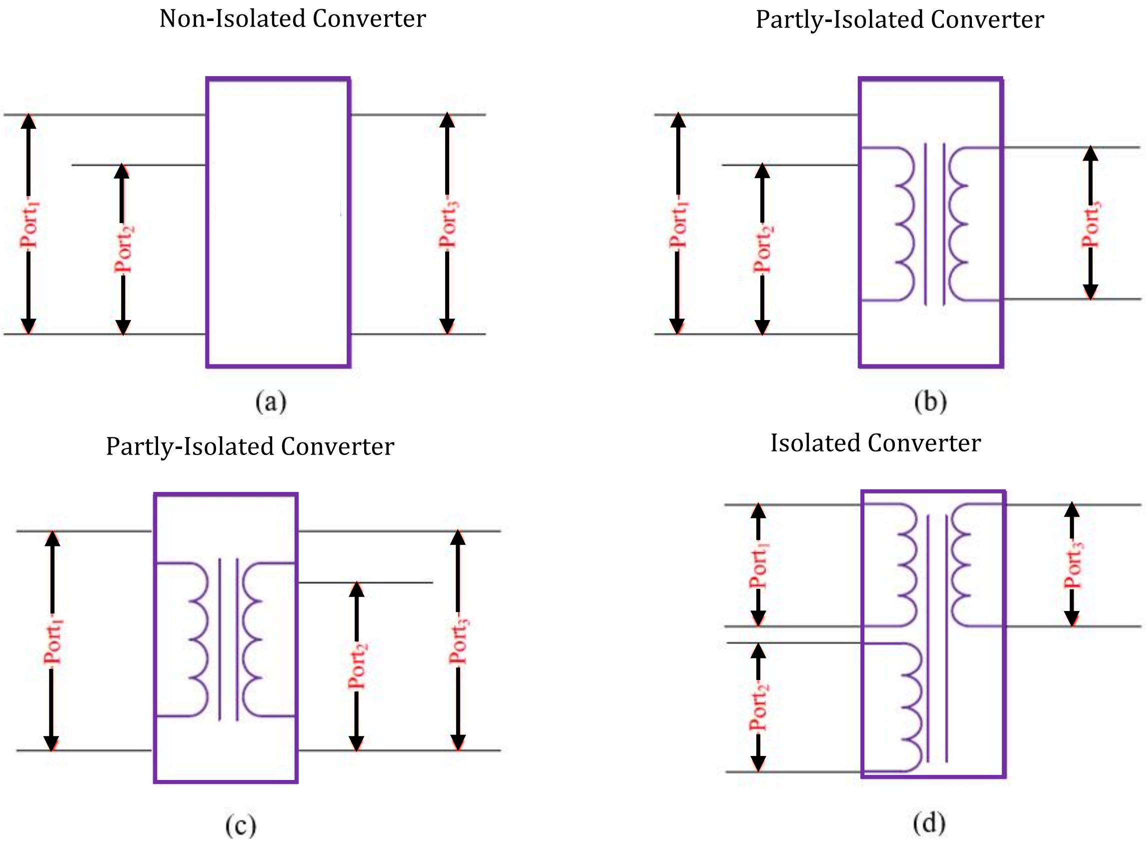
Non-Isolated Converter

Partly-Isolated Converter

(a)

(b)

Partly-Isolated Converter

Isolated Converter

(c)

(d)

Fig 2.4 MPC category: (a) Non-isolated converter. (b), (c) partly isolated converter. (d) Isolated converter.

According to [27], Fig.2.5 illustrates a simple buck-boost converter with a multi-input based on a simple design. Using this topology, N input sources with different characteristics can be connected. This topology has the advantage of having a low component count and being simple to control which is two of its main advantages. A single inductor, diode, and capacitor are shared between the inputs of the given design. Although this topology is unidirectional, the ports in the topology can transmit power in only one direction. Due to this, ESS cannot be implemented on this topology, as it is unsuitable for this purpose.

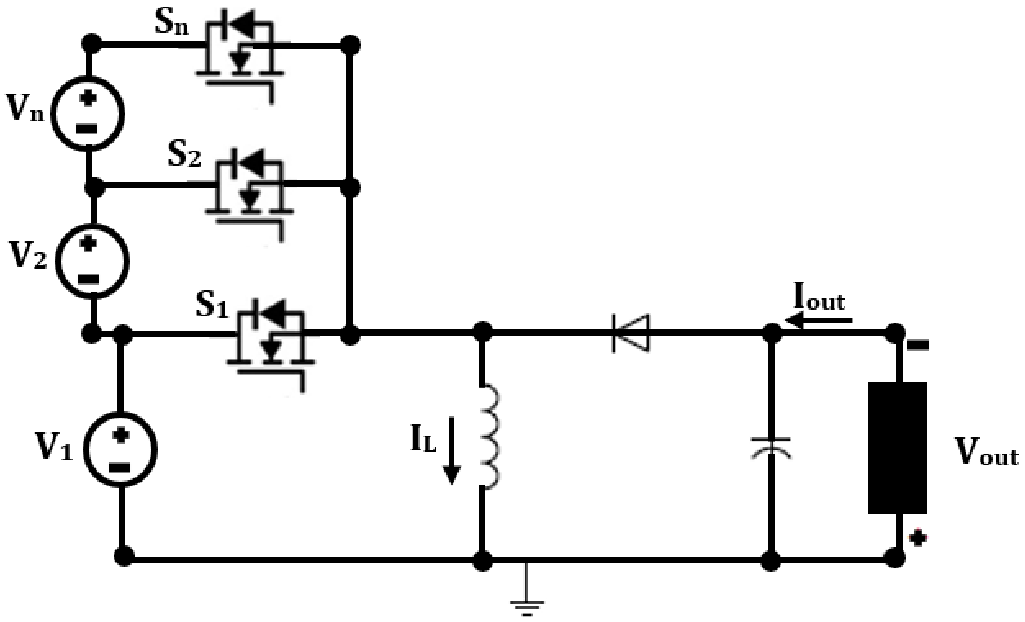

Fig 2.5 Multi-input buck-boost converter [27].

Based on the multi-port converter proposed in [51], Fig.2.6 illustrates a multiport converter. Furthermore, the output voltage of the new proposed converter has the advantage of a positive polarity, which can be achieved without using an additional transformer in addition to the advantages of the previous converter. It is very convenient to use this new converter because it has a bidirectional power flow that does not require an additional converter; it can be used as a buck converter, a boost converter, and a buck-boost converter. In addition to operating in Continuous Conduction Mode (CCM), the converter can also operate in Discontinuous Conduction Mode (DCM).

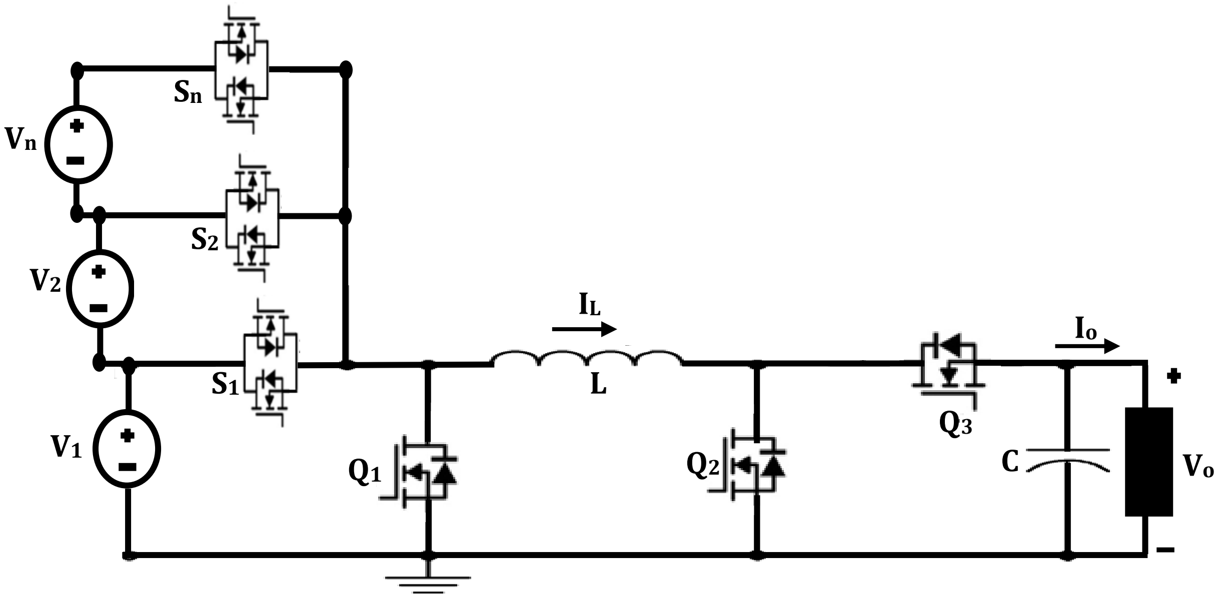

Fig 2.6 Multi-input buck-boost converter [51].

According to the paper of [52], there is a boost-type, three-port non-isolated converter shown in Fig.2.7. In this study, an integrated circuit is proposed that is capable of interfacing one renewable energy source, a battery, and a load simultaneously. There is an advantage to this topology which is an equal distribution of the power between the three ports at the same time. Two filter capacitors are connected in parallel with the PV panel and battery to smooth the pulsation current of the PV panel and battery. Specifically, the converter is designed to operate in three different modes, namely, Dual-Outputs (DOs), Dual-Inputs (DIs), Single-Inputs, and Single-Outputs (SISOs).

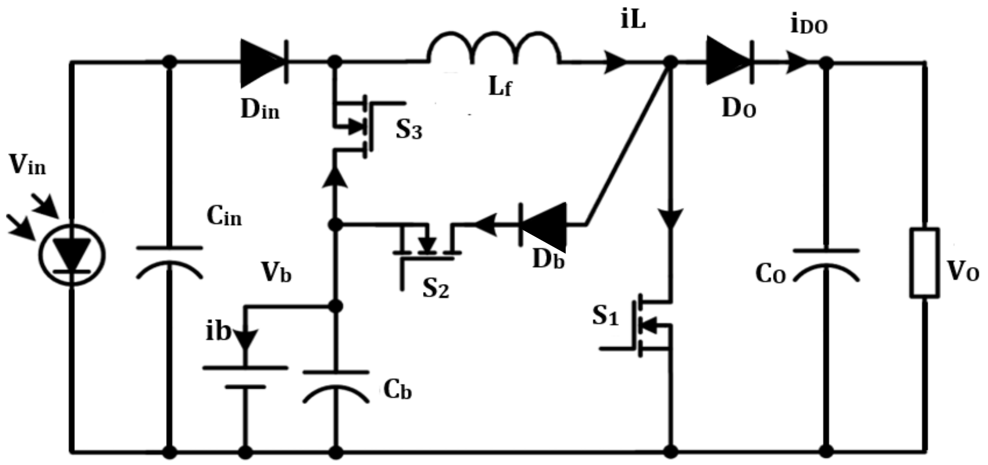

Fig 2.7 Boost three-port converter proposed in [52].

The authors of [53] proposed a non-isolated, single-switch DC-DC converter. Combining a cascade buck converter with a buck-boost converter is a great way of reducing the number of components in the system. As mentioned previously, the function of the combined buck and buck-boost converter comes down to one switch that can handle the Maximum Power Point Track (MPPT), the battery charging, as well as the operation of the load, which in this case is the water pump, at a constant flow rate at the same time. An illustration of the proposed circuit is shown in Fig.2.8.

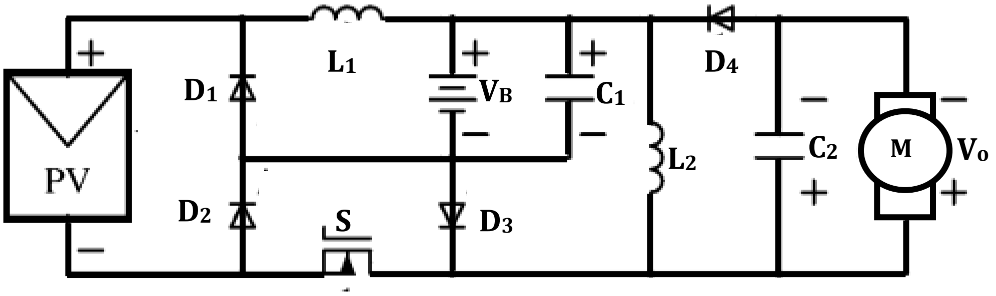

Fig 2.8 Single-switch non-isolated DC-DC converter [53].

Based on the findings of [42], the authors proposed a non-isolated "three-port converter with high step-up", as seen in Fig.2.9. The method of coupling inductors is used to achieve a high voltage gain for the converter. For the purpose of suppressing the leakage inductance effect, two clamped circuits are used. The proposed converter has two different paths of power flow, one which is the main voltage source that delivers power to the load, and the other which is the battery that supplies power to the load. As a result of the proposed TPC, three different modes have been developed. This leads to the input power source and ESS being able to transfer power independently to the load by taking advantage of the two distinct power flow paths. Power can also be transferred from the input power source and the ESS to the load simultaneously, as well as the power to the load while simultaneously charging the ESS from the input power source.

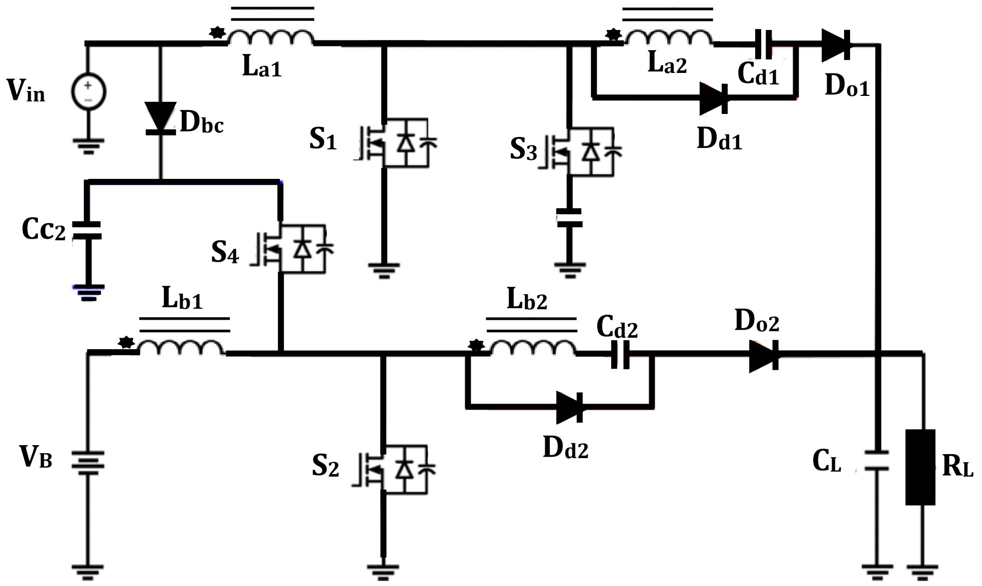

Fig 2.9 Non-isolated high step-up three-port DC-DC converter for hybrid energy systems [42].

According to [54], a battery-integrated boost converter comprises just one switch, diode, and capacitor, as shown in Fig.2.10. A series combination. A direct path can be provided for charging the battery by combining solar power and battery, allowing the solar energy source to deliver the maximum power. With the proposed converter, it is possible to facilitate the tracking of Distributed Maximum Power Points (DMPPT). As the PV module becomes an open circuit during the night and the diode prevents the flow of current the other way, the proposed converter cannot provide power during the night.

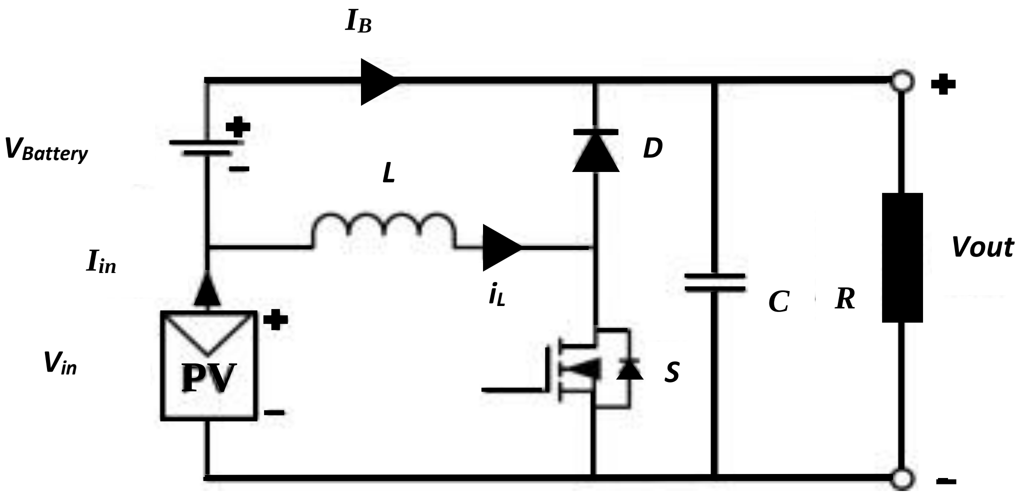

Fig 2.10 Three-port battery-integrated boost converter [54].

Based on the findings of [55], the author proposed a non-isolated “dual-input dual-output boost converter”, as seen in Fig.2.11. The proposed converter operates in DI and DO modes with an inductor current hysteresis comparator for mode switching is an effective form of energy management. However, controlling five switches for the TPC operation is more complex and decreases efficiency.

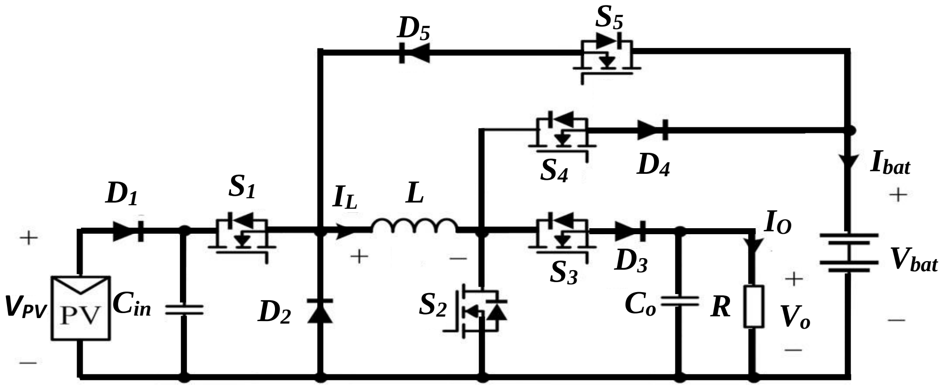

Fig 2.11 Proposed a non-isolated “dual-input dual-output boost converter [55].

2.1.2 Partly Isolated Converter

In Three-Port Converter that is partly isolated, at least two ports share the same ground with each other and are directly connected to each other. As well as this, at least one port on the device is connected to a transformer that generates high frequencies [56]. Galvanic isolation may be provided for some ports with this type of arrangement. The high-frequency transformer provides the isolation feature and increases voltage gain by changing the transformer's turn ratio and achieving the isolation feature.

The authors of [57][58], [59] proposed a partly isolated three-port converter with three types of ports: one for solar energy, one for batteries, and one for outputs. As shown in Fig.2.12, the proposed circuit is based on the principles of an active clamped forward converter and the half-bridge converter to achieve the desired results. On the primary side of the transformer, there is an addition of one switch and one diode, while on the output side, there are two switches that replace the traditional half-bridge converter's output diode.

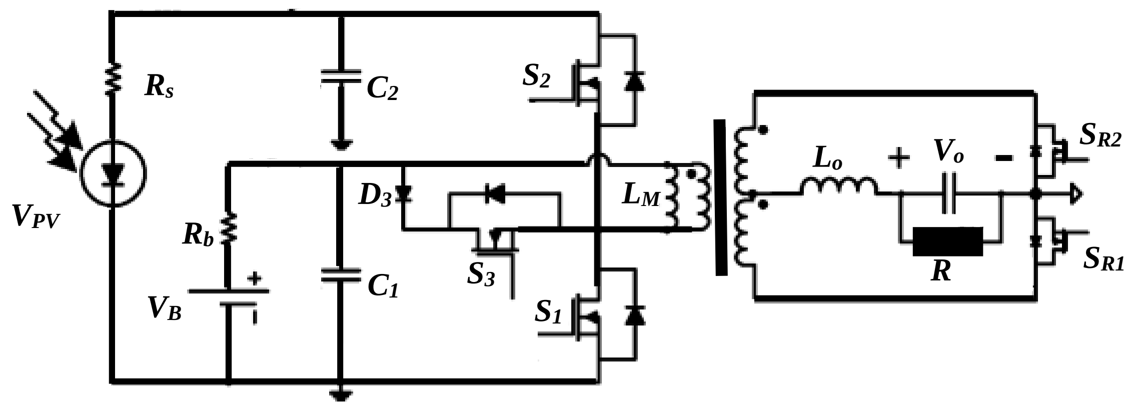

Fig 2.12 The converter proposed in [59].

It has been proposed, however, that the authors of [60]. have developed a family of three-port half-bridge converters. These converters have three topologies: three-port half-bridge converters with post-regulation, three-port half-bridge converters with synchronous regulation, and three-port half-bridge converters with primary freewheeling. In terms of stand-alone renewable power systems, converters are suitable for use in this field. A schematic diagram for this converter can be seen in Fig.2.13. This shows that when the converter's output voltage is raised, the effectiveness of the converter is reduced due to a reverse recovery loss associated with the body diode of the output switches.

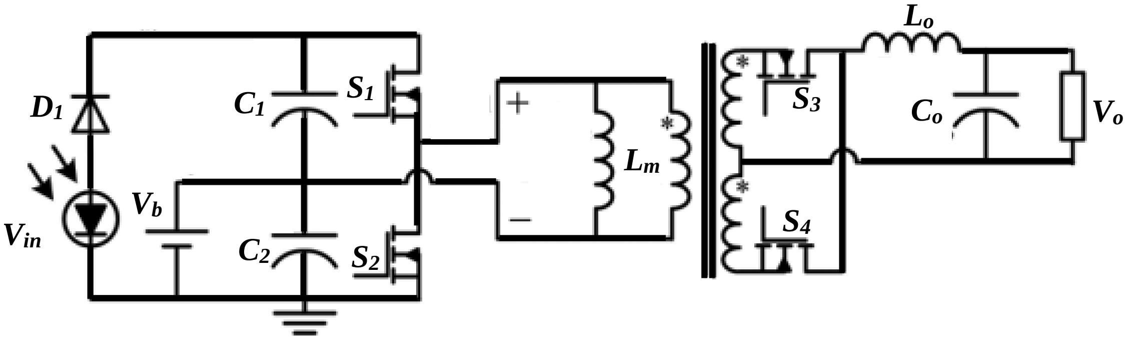

Fig 2.13 The three-port half-bridge converter with synchronous regulation [60].

As shown in Fig. 2.14, a Full-Bridge Three-Port Converter (FB-TPC) that is controlled by Pulse Width Modulation (PWM) and Secondary-Side Phase Shift (SSPS) is presented in [61]. As the picture below shows, the converter is developed by combining an interleaved buck/boost converter and a phase-shift full bridge converter on the secondary side, in which the primary active switches are shared. The system's primary and secondary sides have been achieved with zero voltage switching so that the power can be easily transferred between any two ports without any problem. In [62], a distributed DC grid design for PV applications has been implemented in which the proposed topology has been applied.

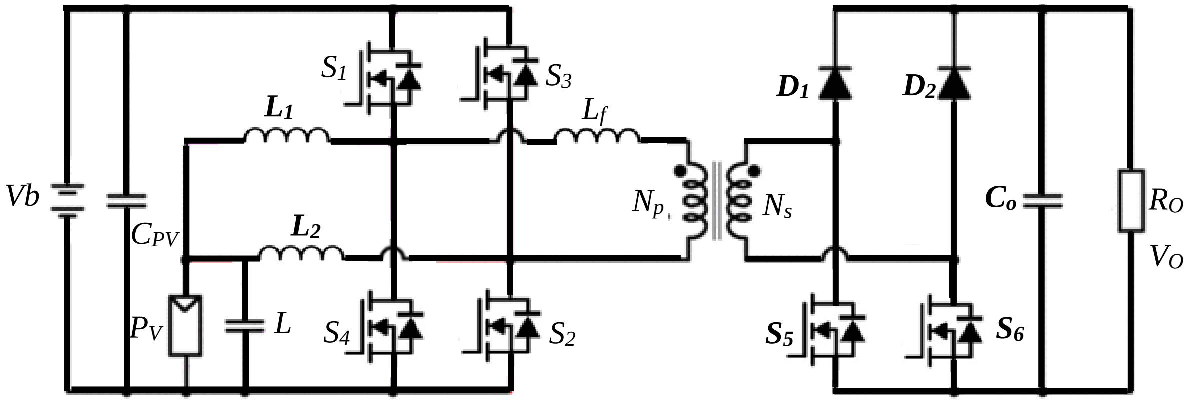

Fig 2.14 The pulse width modulation (PWM) plus secondary-side phase-shift controlled full-bridge three-port converter proposed in [61].

The proposed topology, as shown in Fig. 2.15, utilises a current-fed dual active bridge structure, which is characterized by galvanic isolation between the battery and the dc bus, a wide range of Zero Voltage Switching (ZVS), and a bidirectional flow of power between any two ports of the system. A voltage multiplier cell is used on the DC bus side of the bridge to achieve a high voltage conversion ratio between the DC bus and the supercapacitor (SC). Topologies like this may lead to fluctuations in battery current [63], and the complexity of the circuit or component ratings may increase [64].To achieve reverse power flow and continuous charge/discharge current, [64] uses 22 active switches, while another existing four-port converter [65] uses eight switches.

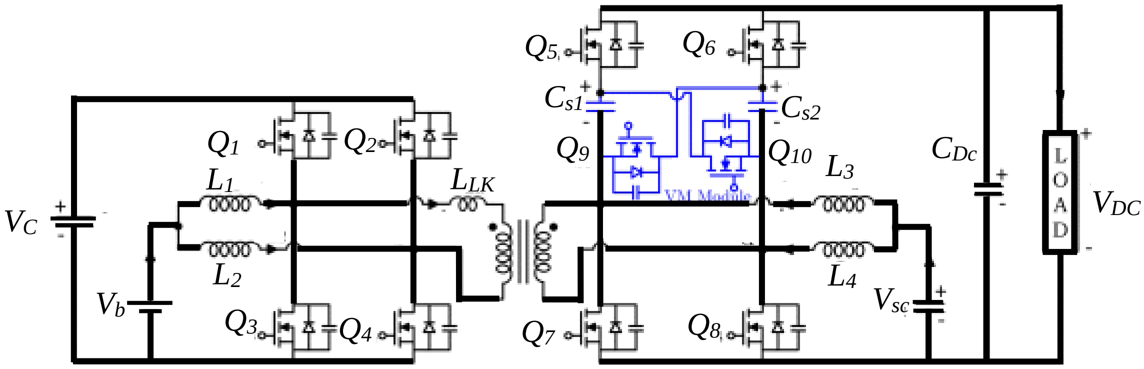

Fig 2.15 A current-fed dual active bridge structure [63].

2.1.3 Isolated Converter

An isolation converter can also be referred to as a traditional half-bridge converter or a full-bridge converter [66],[67]. The high-frequency multi-winding transformer in the isolated converter connects all the ports. This means that all ports in this topology are fully galvanically isolated. By using bidirectional power switches, it is possible to enable bidirectional power flow between the ports of this topology. However, there is a high number of components present in this system. It is hard to share some of these components between ports as they all require their components. Increasing the turn ratio of the high-frequency transformer can achieve a high voltage gain, which can lead to a higher voltage output.

An example of a triple DC-DC converter is shown in Fig. 2.16 [68]. All ports of the circuit can achieve a bidirectional flow of power, which is a desirable feature. There is no problem matching different voltage levels at each port as long as using a three-winding high-frequency transformer with different turn ratios is possible. To control the flow of power, phase shift control is used. An example of such work can be found in [69]. Zero Voltage Switching (*ZVS*) is extended by introducing a simple and effective duty ratio control method on top of the previous work to enhance its effectiveness. Two series resonant tanks have been added to the full-bridge structure to achieve higher switching frequencies and lower losses during switching [70].

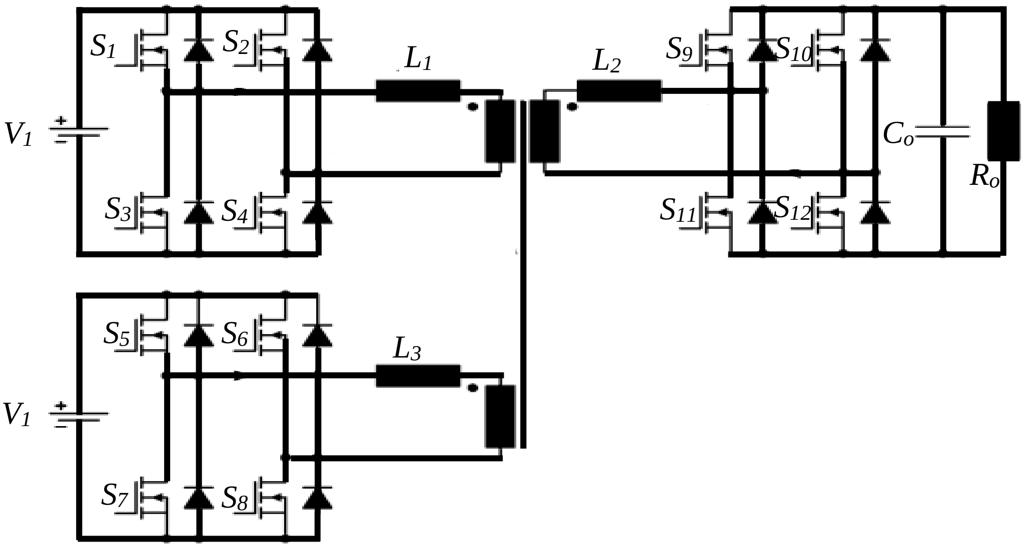

Fig 2.16 Isolated triple-active-bridge converter full bridge [68].

In [71], the authors proposed a DC-DC converter consisting of three ports and three half bridges, one of which is a boost half-bridge topology and the other half-bridge bridges. It is achieved using a high-frequency transformer that connects both half-bridges to achieve high voltages and galvanic isolation between them. There is a smaller ripple in current when using a current-fed topology, which is regulated as a boost converter. This is compared to voltage-fed topologies. This result boosts voltage reduces the transformer current requirement and provides a current mode control to offer more control flexibility.

Two current-fed topologies are employed on the low voltage side by [66],[72] for interfacing low voltage devices such as a low voltage battery and an ultracapacitor, as shown in Fig.2.17.

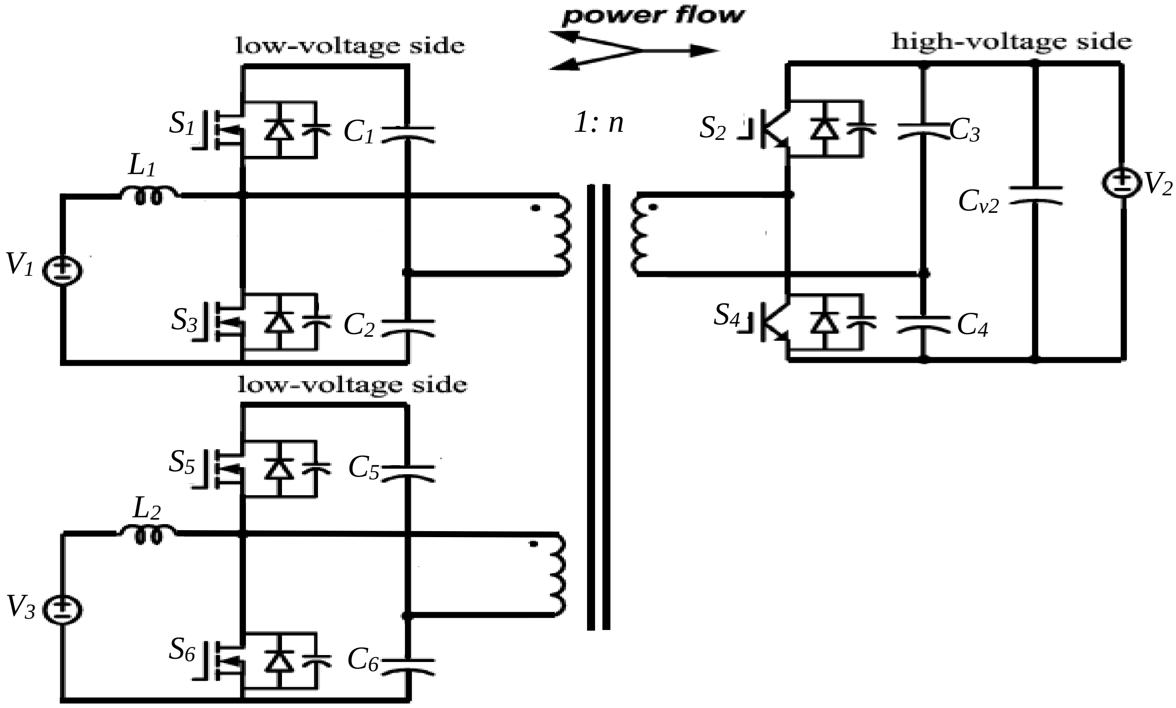

Fig 2.17 Isolated triple-active-bridge converter half bridge [66],[72].

In addition, switching losses are usually one of the key factors affecting system efficiency, especially during light loads. Several series-resonant converters have been proposed to reduce switching losses and achieve full-ZVS operation [73],[74]. An isolated three-port bidirectional series-resonant converter is proposed for energy storage applications that feature the first harmonic-synchronized pulse width modulation, as shown in Fig.2.18. Using additional resonant components in this design structure will result in increased system costs, reduced power density, and worse dynamic performance.

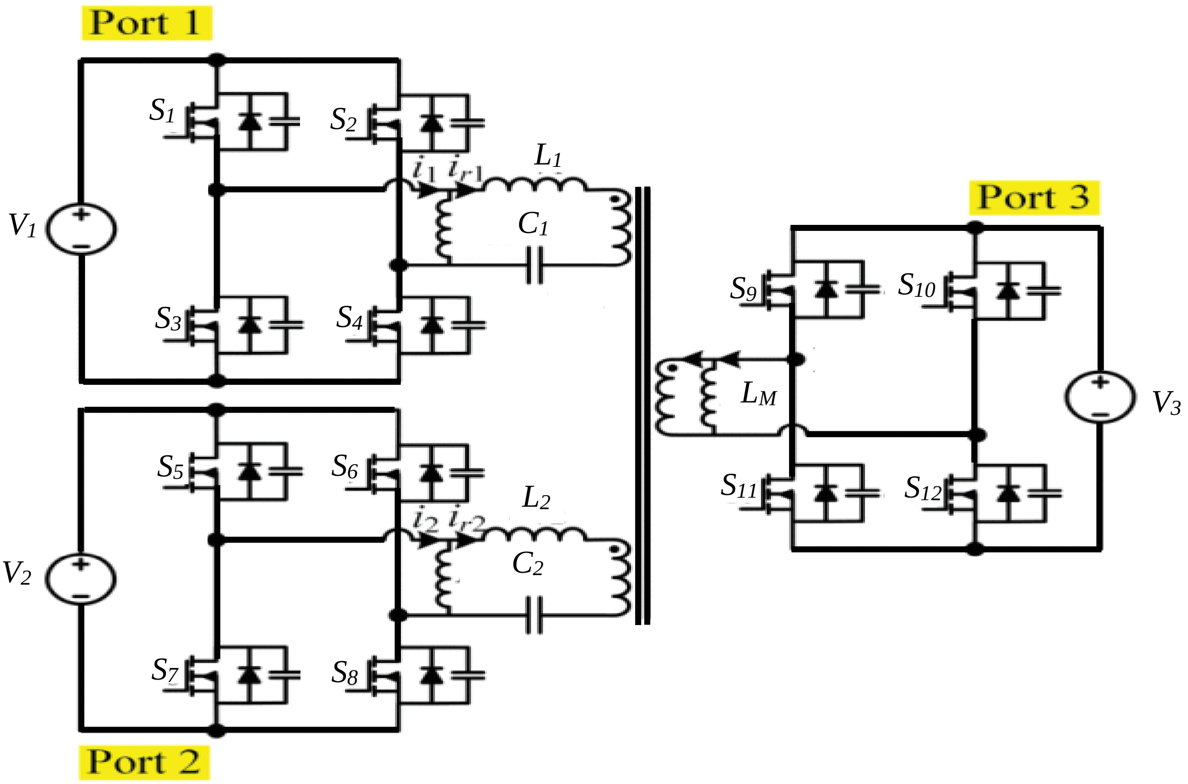

Fig 2.18 An isolated three-port bidirectional series-resonant converter with first harmonic-synchronized pulse width modulation [74].

2.1.4 Comparison of Different Multi-port Converters

The advantages and disadvantages of each of the groups of MPC are different. Galvanic isolation is used in a fully or partially isolated multi-port converter so that all the ports are galvanically isolated from each other to prevent shock hazards. In such a setup, it is very easy to achieve ZVS. As well as this, there is a greater likelihood of achieving a high voltage-regulated ratio due to the use of a high-frequency transformer. Despite this, they are heavier, larger, and incur more magnetic losses because of the use of the high-frequency transformer and the inclusion of more switches in the half-bridges and full bridges. As a result, the efficiency and power density of the converter is reduced. A trade-off is often necessary between advantages and disadvantages, as it is difficult to choose between them all.

In contrast to the isolated multi-port converter, the voltage-regulated ratio of the non-isolated multi-port converter is limited by the converter's duty cycle, and it isn't easy to achieve ZVS using such a converter. In contrast to the isolated converter, the non-isolated converter has several advantages over the isolated converter, including high efficiency and high-power density, together with a low cost due to its numerous shared components that make it more cost-effective. A coupled inductor switched capacitor, switched inductor, and multiplier circuit could mitigate the drawbacks of non-isolated converters.

2.2 Topology Review of Typical High Voltage Step-Up Converters

This section aims to give a brief overview of the typical topologies of boost converters to improve their performance. When it comes to non-isolated converters, switching capacitors, switching inductors, and coupled inductors can all be used to improve voltage boost ratios by a significant amount. Transformers and non-isolated converters are usually combined to form isolated converters. In this way, high voltage conversion ratios could be achieved by changing the turn ratio of transformers.

2.2.1 Cascaded Converters

To reach a higher output voltage, as shown in Fig.2.19, multiple boost converters are connected in series to reach a higher output voltage to overcome the voltage gain limitation of traditional boost converters [75],[76].

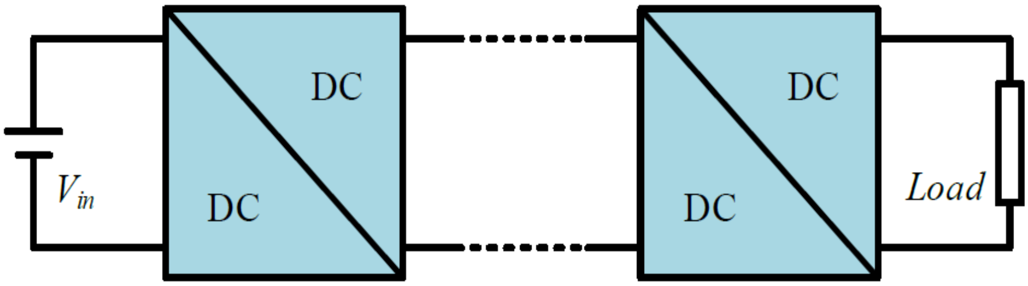

Fig 2.19 Configuration of cascaded DC-DC converter [75],[76].

Previous boost converters have their output ports connected to the input ports of subsequent boost converters. Thus, a cascaded converter has a voltage step-up conversion ratio that is increased to the product of the voltage gain of each boost converter in the cascade. Fig.2.20 shows that in the cascaded connection of two boost stages. This approach enabled a high voltage conversion ratio without using the unity duty cycle. There is a decrease in the voltage stress placed on the switch Q_1 and the diode D_{o1} in the first-stage converter compared to a single conventional non-isolated boost converter. This reduces the switching loss and conduction loss of switch Q_1, along with a better reverse recovery performance for diode D_{o1} compared to a single conventional non-isolated boost converter. Due to the intermediated voltage of capacitor C_{f1}, the second conversion stage reduces the input current. However, the voltage stress of semiconductor components in the second stage is equal to that of a conventional non-isolated boost converter, as the voltage stress of semiconductor components is equal to that of the output voltage. This cascaded structure is not without its downside, which is the complexity of controlling two switches. To ensure the stable operation of the cascade converter, two closed-loop control circuits are required, and this causes the cost of the converter to increase.

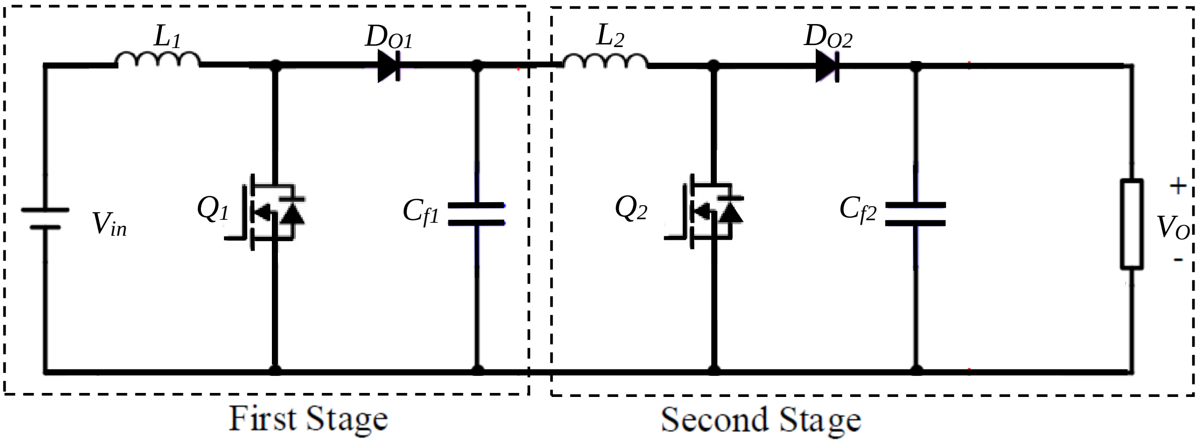

Fig 2.20 Cascade converter with two stages boost converters [75],[76].

2.2.2 Quadratic Boost Converter

This quadratic boost converter has been proposed to reduce the complexity of the control process of cascading two boost converters together to achieve a high voltage conversion ratio by using only one switch for a high voltage conversion ratio shown in Fig.2.21. [77]–[79]. Rather than using a switch Q_1 to control the circuit's feedback, the diode D_1 is used instead, which reduces the number of switches and closed feedback loops in the circuit. In Fig. 2.21, a quadratic boost converter operates similarly to a cascaded converter. Similarly, the quadratic boost converter can achieve high voltage gains without being hampered by extreme duty cycles of switches, as in cascaded converters. The main disadvantage of this method is that energy is converted twice, which can impact the system's efficiency. Moreover, high-rated components are required due to the high voltage and current stress on switch Q and the diode D_{o2}, creating an increased conduction loss on the circuit.

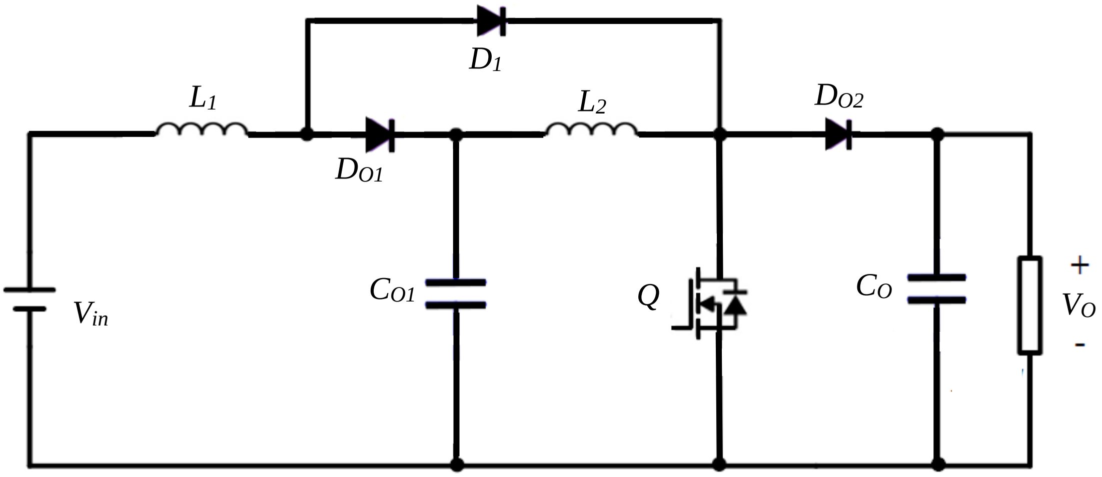

Fig 2.21 Quadratic boost converter [79].

2.2.3 Switched Capacitor Converters

Fig 2.22 shows the basic topology of switched capacitor converters that involve only the transfer of electrical energy as its operating principle [80]. The voltage of the switched capacitor is increased to V_{in} when switches Q_1 and Q_2 are on and Q_3 are off. When Q_3 is on and Q_1 and Q_2 are off, the capacitor C is connected in series with the voltage source V_{in} to provide power to the load. Due to this, it is possible to obtain a high output voltage by doubling the input voltage due to the above process.

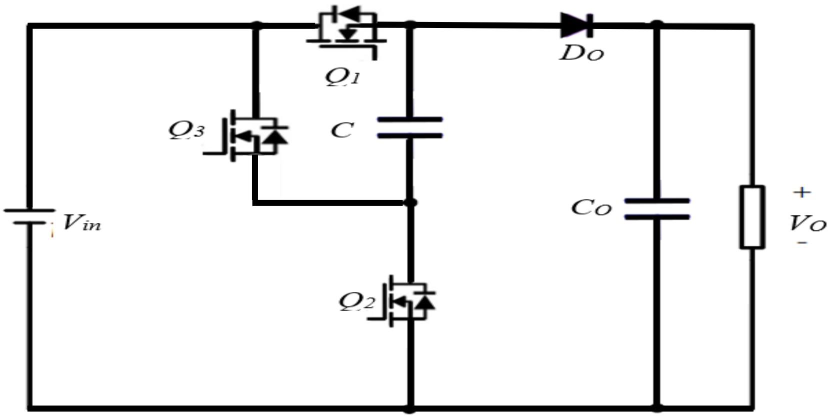

Fig 2.22 Topology of switched capacitor converter [80].

This switched capacitor cell, known as the voltage lift circuit, is integrated inside the boost converter so it boosts the voltage output [81]–[83]. A wide range of voltage conversion ratios can be obtained by controlling the duty cycle of the switches to regulate the output voltage. This voltage lift cell is integrated with the conventional boost converter, as shown in Fig.2.23, and is used to improve the voltage gain of the converter. When switch Q is switched on, the power source V_{in} and the inductor L_b charge the capacitor C_1. C_1 is connected in series to V_{in} and L_b on turning off the switch, resulting in a high output voltage.

Furthermore, components can maintain a lower current ripple due to the inductor L_b. Because the static voltage gain involves the number of voltage lift cells, it is necessary to obtain a high voltage step-up ratio with a large number of components to obtain the high voltage step-up ratio. A voltage stress is also referred to as a voltage differentiation value of a switch, which is the difference between the output voltage and the input voltage.

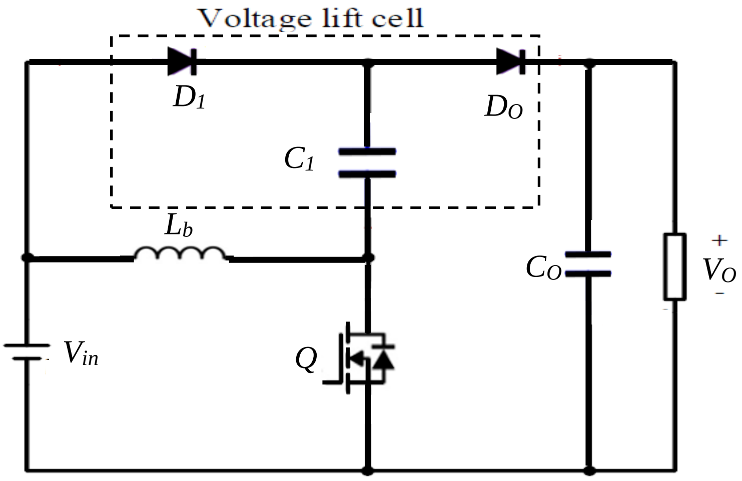

Fig 2.23 Topology of the voltage lift circuit [82].

2.2.4 Switched Inductor Converters

It is interesting to note that switched inductor converters, which use the same operating principles as switched capacitor converters, are characterised by the fact that they use a series connection between inductors and voltage sources to obtain a high output voltage [84]–[87]. It can be seen from Fig.2.24 that when switch Q is initiated, two inductors, L_1 and L_2, start to be charged by the diodes D_1 and D_2. Through the diode D_3, power is transferred from the input source, together with both inductors L_1 and L_2, to the load after the switch has been turned off. Accordingly, the output voltage will equal the maximum of the input voltage and the voltage of either L_1 or L_2, assuming that the inductors' L_1 and L_2 voltages are the same. As a result, the system's power efficiency is deteriorating because the voltage stress caused by switch Q equals the output voltage, which decreases power efficiency [84].

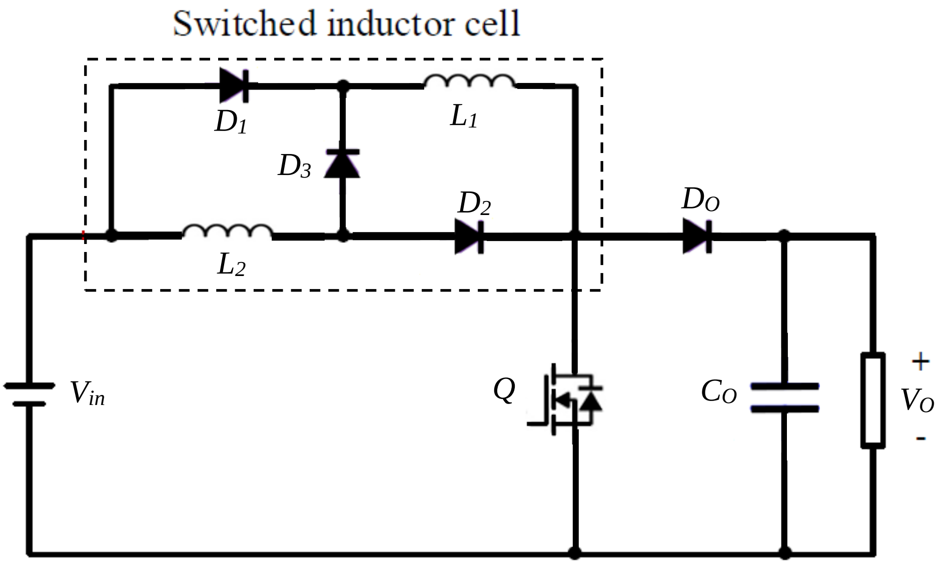

Fig 2.24 Topology of the switched inductor converter [86].

A two-switched-inductor boost DC-DC converter can be seen in Fig.2.25. The active network converter is called a two-switched-inductor boost DC-DC converter. A switched inductor cell is transformed into an active network converter by eliminating the diode D_3 and substituting active switches Q_1 and Q_2 for diodes D_1 and D_2. The power is transferred into the inductors L_1 and L_2 by conducting the two switches. Diode D_o transfers power from the input and switched inductors to the output when the switches are off. The duty cycle of both switches is the same.

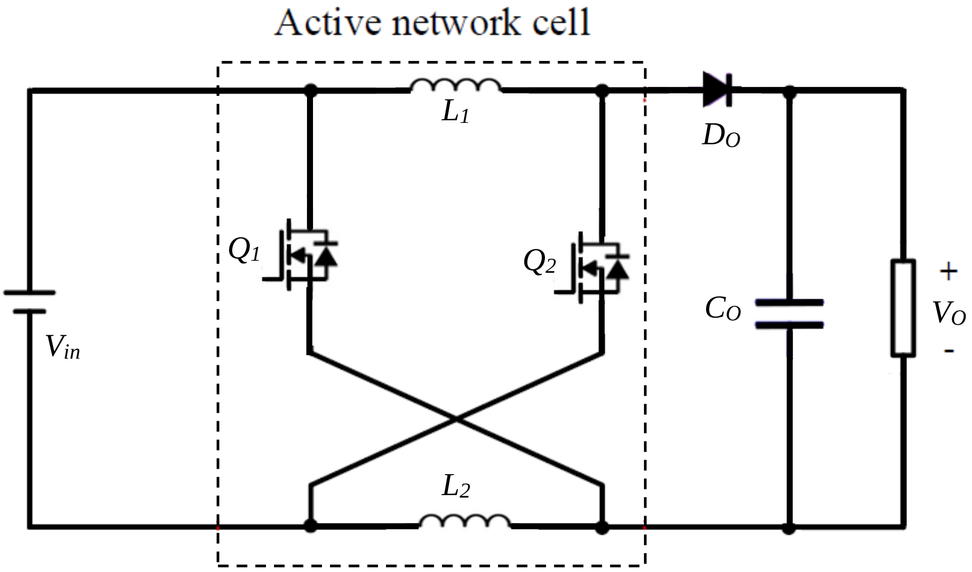

Fig 2.25 Topology of the active network converter [86].

The energy stored in the inductors is approximately equivalent to the magnitude of the voltage input, as with the switched capacitor converter. Due to the limitations of switched inductor converters in terms of voltage gain, they cannot meet the needs of many applications. Although the voltage gain in the active network can be increased by replacing the inductors L_1~L_2 in the network cell for switched inductors, the converter will have a significant increase in volume, weight, and cost [88]. There is also a possibility that the currents of two inductors will be different when the characteristic of the two inductors differs. When the switched inductors are discharged in series, the voltage spike of the switches is also high. There is also a high reverse recovery loss in diode D_o because the voltage stress is equal to the sum of the diode's input and output voltage.

2.2.5 Integrated Converters

There is no method, according to the discussion above, that can achieve high voltage step-up ratios without causing any disadvantages in the process. There are limitations to the voltage gain of both the non-isolated conventional boost converter and the three-level boost converter imposed by their duty cycle. Cascaded converters and quadratic boost converters could be used to increase voltage gain, which used several cells in a series connection, leading to an increase in voltage gain. Still, the use of many components necessitated a complex system for control. The energy stored in the capacitors has been successfully applied to increase the output voltage of the switched capacitor converters and multiplier circuits. Consequently, switched inductor converters are designed to provide high voltage gain by installing the charged inductors in switched inductor converters. Despite this, in all of these cases, the voltage gain has been significantly increased with an increment in the number of components used in each case.

The high voltage gain is produced by using high turn ratios of transformers in transformer-based converters, including isolated converters, and coupled inductor converters, resulting in a large volume, a high weight, and a high loss of power for transformer-based converters. A transformer with a core loss and a winding loss will lower power generation efficiency. To achieve the high efficiency and high voltage step-up ratios required for DC-DC converters, extensive research has been conducted in topologies that integrate the capacitive and magnetic methods. Some circuits, such as coupled inductors and voltage multiplier circuits [89]–[93], coupled inductors and switched capacitors [94]–[97], three-state switching cells and autotransformers [98], and three-state switching cells and voltage multiplier circuits [99], can be incorporated into converters to enhance the voltage gain.

2.3 Classification of DC-DC converters by Voltage Gain

A comparison of typical DC-DC converters with high voltage gains is presented in the final part of the study to identify their respective advantages and disadvantages. Based on the level of voltage gain the converter has, they can be classified as shown in Fig.2.26, either through extensive or limited voltage gains. The voltage conversion ratio of the typical boost and buck-boost converters is limited due to their conventional design. In addition, there is also a limitation as to the gain ratio of the voltage of the three-level converters. With an extreme duty cycle of switches, they can only achieve a high voltage gain. Multiple converter cells can extend the voltage step-up conversion ratio of wide static voltage gain converters and switched capacitors, switched inductors, and transformers. There is a significant increase in components when cascaded converters, capacitor/inductor converters, and MMC converters are used to achieve high-voltage gain.

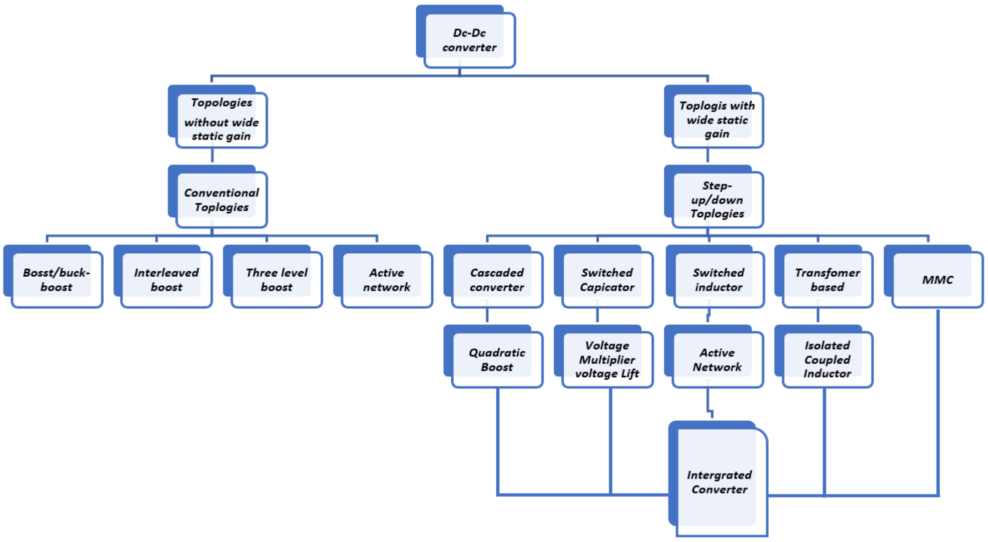

Fig 2.26 Classification of boost converters by voltage conversion ratio [100].

2.4 Switching Strategy

A semiconductor component will require three kinds of power consumption: conduction loss, switching loss, and driving loss. Power switch driving losses are the costs associated with turning power switches on and off, a factor that is often overlooked. Furthermore, the conduction loss only affects the on-state resistance of the device and its on-time t_{on} in one cycle as long as the corresponding devices are conducted. Therefore, installing components with a low on-state resistance could be beneficial to reduce the conduction loss level. Switching loss occurs when switches are turned on and off, which can be reduced by decreasing the switching frequency, reducing the switching loss. Despite this, with the decrease in switching frequency, there will be an increase in the volume of passive components.

2.5 Failure Mechanism

Based on the field experience, it has been found that semiconductor components such as diodes, IGBTs, and MOSFETs have the greatest vulnerability [101],[102], whose failure may have serious implications for personal safety. Consequently, from academic and industry perspectives, fault tolerance is important for power converters.

2.5.1 Failure Type

Two types of faults can be categorised as Short-Circuit Faults (SCFs) and Open-Circuit Faults (OCFs). SCF is a condition which can occur in DC-DC converters causing over-rated currents to flow through components such as the output capacitor and load, resulting in overheating and eventual failure of the entire system and even explosion. Several factors can cause OCF to be less destructive than SCF, which will cause the power system to be shut down and other components not to be damaged. However, the unexpected failure of some critical applications, such as military and aeroplanes, will place passengers in potential danger if the system goes down unexpectedly.

2.5.2 Diode Failure Indications

In particular, diodes have a high potential for failure, especially when operated at high voltages or currents. It is well-known that the resistance drops to zero or very low values when a diode is short-circuited in both the forward and the reverse direction. In rare cases, an open circuit failure may occur and leads to diode resistance becoming extremely high or infinite in both directions [103].

2.5.3 Transistor Failure Indications

Several transistors are used in high voltage and current situations while maintaining a minimum amount of internal power dissipation. These transistors include IGBTs and MOSFETs. The voltage, current, and power that can be output by a device can exceed its rated capability in the case of fault conditions. Consequently, it is easy for short-circuits to occur within the transistors. Additionally, when the silicon chip is overheated, the transistors on the silicon chip would become open-circuit, and they would be vulnerable to unsoldering when the chip is overheated.

2.6 Summary of existing solutions

The work proposed in this study will focus on developing new type of DC-DC converters, which has a combination of properties that make it unique compared to existing DC-DC converter topologies. The work undertaken can be broadly considered as follows:

2.6.1 Development of new Multi-Port Converters

A review of MPC topologies for integrating PV with ESS is presented. Based on the literature review, the non-isolated topologies are cost-effective, highly efficient, and useful for low-power applications like satellite applications. Thus, a satellite platform's cost heavily depends on its mass. The mass of the space power system is a significant design constraint. The non-isolated converter is the best topology to integrate the PV with ESS because the sharing component will be cost-effective. In this study, the third and fourth chapters have focused on developing new type of DC-DC converters, which has a combination of properties that make it unique compared to existing DC-DC converter topologies. Integrating different input sources to enhance the efficiency of the system, which is low-cost by sharing components and reducing power conversion stages by reducing component counts, making the design compact with low volume. Table 2.1 gives the existing solutions and their downside.

Table 2.1 Review of MPC topologies

Existing Solutions	Downside
Non-isolated-multi-port converters	no isolation, low voltage gain
Partly-isolated-multi-port converters and Fully-isolated-multi-port converters	weight, size, and magnetic losses increase, so, the efficiency and power density reduce

2.6.2 Achieve high voltage step-up ratios.

According to the discussion above, no method can achieve high voltage step-up ratios without causing any disadvantages. To achieve the high efficiency and high voltage step-up ratios required for DC-DC converters, extensive research has been conducted in topologies that integrate the capacitive and magnetic methods. Some circuits, such as coupled inductors and voltage multiplier circuits [89]–[92], [104]. In this study, the fifth and sixth chapters have included high voltage step-up ratios as part of their application requirements by using two methods, such as multiplier circuits and cascading two topologies to share components and reduce power conversion stages which reduce component counts, enhance the efficiency of the entire system and achieve high gain with low cost. Table 2.2 gives high voltage step-up ratios methods.

Table 2.2 High voltage step-up ratios methods

Existing Solutions	Downside
Quadratic boost Converters	many components, which leads to a complex control
Three-Level Boost Converters	extreme duty cycle, and the voltage gain is limited
Switched Capacitor Converters	the cost and design complexity are high when a large amount of switched capacitor cells is applied
Transformer-Based Converters	weight, size, and magnetic losses increase, so the efficiency and power density are reduced
Coupled Inductors	a large volume, a high weight, and a high loss of power, so high cost and design complexity

2.7 Summary

A selection of MPC topologies for the literature review has shown that the non-isolated topologies are cost-effective, highly efficient, and practical for use in low-power applications due to their capabilities. The integration of PV with ESS is presented in this chapter. Those isolated or partially isolated topologies are best suited for applications where high power is required. In conclusion, non-isolated converters are the best topology to integrate PV with ESS based on the aforementioned conclusion. Thus, it will be the topic of the subsequent two chapters. According to the analysis above, a substantial amount of work has been done on high-voltage step-up DC-DC converters based on the topologies failure mechanisms described above. For a high voltage step-up ratio to be achieved, several typical topologies can be utilized, such as cascaded converters, switched capacitor converters, and switched inductor converters. Nevertheless, some particular limitations are associated with each topology, such as a high number of switches, high volume, low power efficiency, and an issue relating to leakage inductance.

Chapter 3 Not-isolated DC-DC Converter with Multiple Inputs and One Output for Photovoltaic Power Generation Systems

3.1 Introduction

Power electronics have largely influenced the development of various industrial applications in recent years [105]–[107]. The pollution caused by petrochemical energy resources is causing dramatic climate change on the earth. Therefore, clean energy generation systems are more and more important. For achieving environmentally friendly objectives, photovoltaic power generation (PV) is becoming increasingly prevalent [108]–[110]. Due to their small size, PVs can be located near the load points, thus reducing transmission costs and losses greatly. In order to provide the required voltage and power, PV modules are traditionally connected in series and parallel. Nevertheless, MPPT cannot be applied to each PV module individually. Power electronic devices such as multi-port converters could be very useful in power management.

This chapter describes a novel single-ended primary-inductor converter (SEPIC)-based Two-Input DC-DC Converter. By using a series capacitor to couple energy from the input to the output, the structure inherits all the advantages of the SEPIC converter. The proposed converter has the capability of combining several alternative energy sources. It is also possible to flexibly distribute the load power among different power sources. Due to its buck-boost characteristic, this converter is suitable for maximising the power produced by solar panels. Even if one or more power inputs fail to provide energy to the load, the converter presented can operate. Through the use of shared components, two converters are combined into one integrated converter that implements all the functions of two converters. Compared to the traditional DC-DC converters, this DC-DC converter has a high-power density while requiring fewer components to be built. A thorough analysis of the converter's steady-state operation and dynamic modelling is conducted. To verify the proposed circuit, the hardware prototype was constructed and tested. Besides the above features, the converter is suitable for a standalone or a grid-connected.

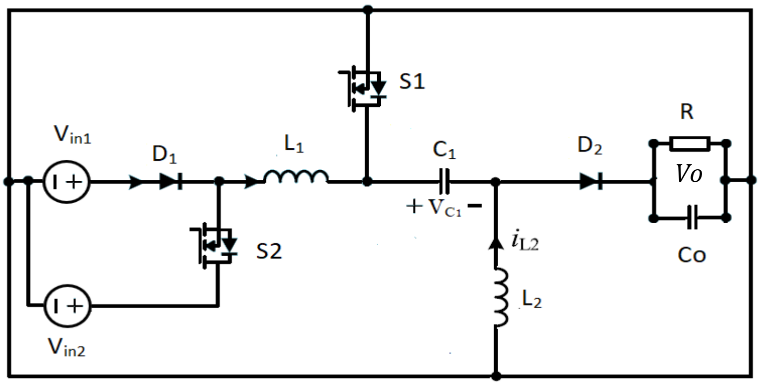

Fig 3.1 Two-Input topology.

3.2 Operation Principle

3.2.1 Proposed Circuit

As shown in Fig.3.1, a two-input converter has been proposed. The converter has two main switches, S_1 and S_2, and two diodes, D_1 and D_2. A pair of inductors is formed by L_1, L_2 and C_1 couples energy from the input to the output, and C_o smooths the output voltage. With the proposed structure of the converter, the converter would be more suitable for generating clean energy from various renewable sources, such as solar panels, whose output is strictly dependent on the environment. It will be discussed in the following section the operation principles of proposed topology. The following sections will provide a detailed discussion of the converter's advantages. Due to its simplicity, the proposed converter consists of a two-input structure that is analysed. Compared to other structures described in [111], the proposed structure utilises fewer components. A DC-DC converter with two inputs is constructed using seven switches [112].

Additionally, capacitor voltage ripples are not considered. The components are also considered ideal, and parasitic parameters are not considered. For the use of the converter in renewable energy systems, the steady-state and dynamic behaviour has been analysed. Accordingly, the steady state of the proposed converter can be described as follows.

3.2.2 Circuit Operation Principles

As shown in Fig. 3.2 and discussed in more detail below, the steady-state waveforms of the proposed converter are depicted. In order to analyse the operation modes, four modes of operation are to be considered, as shown in Fig. 3.3.

Switching mode I [$t_0 < t < t_1$]: [view Fig. 3.3(a)]: During this interval of time, both power switch S_1 and power switch S_2 are ON. The diode D_1 is reverse biased due to V_{in2} being greater than V_{in1}. Energy is absorbed by L_1 from $V_{in2,}$ and i_{L1} increases linearly. Through capacitor C_1, L_2 is charged, and i_{L2} increases linearly.

Switching mode II [$t_1 < t < t_2$]: [view Fig. 3.3(b)]: During this interval of time, the power switch S_1 is ON, and the power switch S_2 is OFF. Linearly an increase in i_{L1} is observed after L_1 absorbs energy from the input source. Through capacitor C_1, L_2 is charged, and i_{L2} increases linearly.

Switching mode III [$t_2 < t < t_3$]: [view Fig. 3.3(c)]: During this interval of time, the power switch S_1 is OFF and the power switch S_2 is ON. By releasing energy through C_1 and V_{in2}, L_1 transmits energy to load R. Also, in this case, L_2 releases energy to load R. This results in linear decreases of i_{L1} and i_{L2}.

Switching mode IV [$t_2 < t < t_3$]: [view Fig. 3.3(d)]: During this interval of time, both power switch S_1 and power switch S_2 are OFF. Through C_1 and D_2, L_1 releases energy to load R. Also, in this case, L_2 releases energy to load R. This results in linear decreases of i_{L1} and i_{L2}.

If S_1 and S_2 are turned ON initially, switching mode I, switching mode II, and switching mode IV may appear in a switching cycle orderly when $d_1 > d_2$ [view Fig. 3.2(a)]. In contrast, states switching mode I, switching mode III, and Switching mode IV will appear when $d_1 < d_2$ [view Fig. 3.2(b)], where d_2 is the duty cycle of switch S_2.

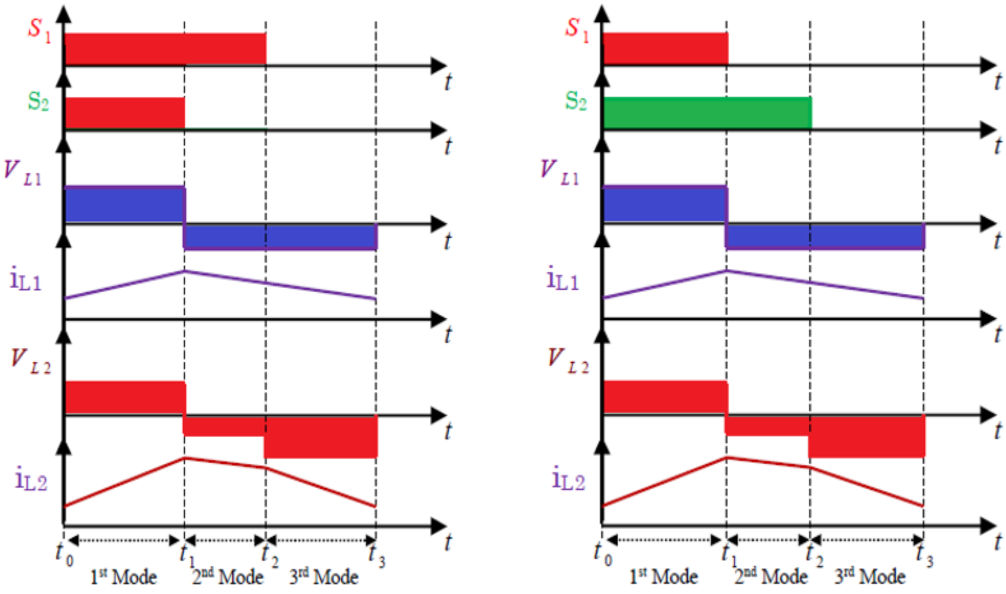

(a) (b)

Fig 3.2 Typical Steady-state waveforms of proposed converter in (a) with d1 > d2, (b) with d1 < d2.

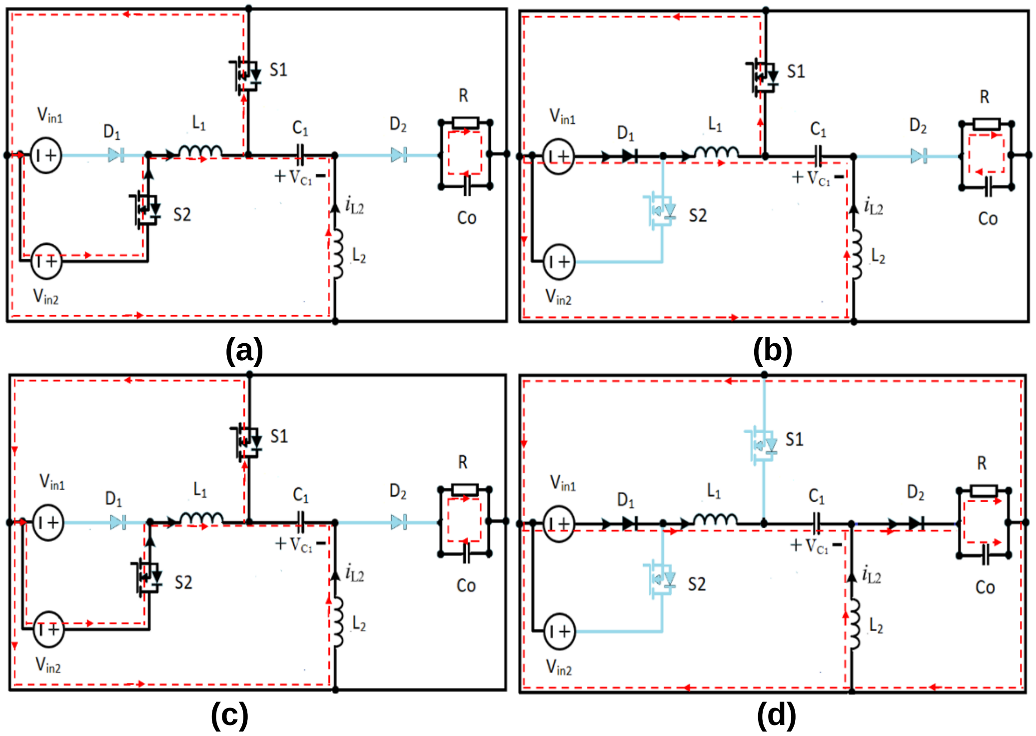

Fig 3.3 Equivalent circuit in DIDO mode. (a) Switching mode I. (b) Switching mode II. (c) Switching mode III, (d) Switching mode IV.

3.3 Steady-State Analysis

With $d_1 > d_2$, according to Fig.3.2 (a), both examples (a) and (b) can be deduced with the same result as $d_1 < d_2$. Therefore, Volt-second balance requirements are applied to L_1 and L_2. It is assumed that the average inductor voltage of a steady state equals zero. This leads to the following equation for the output voltage of the proposed converter.

$$V_O = \frac{d_1[(V_{in2})\,(d_2)+(V_{in1})(1-d_2)]}{(1-d_1)} \tag{3.1}$$

In the case where one of the inputs fails. Therefore, input port V_{in1} is considered to have failed in this case. There will be two switching modes (Switching mode I and Switching mode III) [view Fig.3.3. (a), (c)]. As a result, the output voltage equation of the proposed converter can be rearranged and deduced by using the following formula:

$$V_O = \frac{V_{in2}\, d_1}{1 - d_1} \qquad (3.2)$$

3.3.1 Power Device Voltage Stress Analysis

In order to select the best power switches and diodes, voltage stresses on semiconductors are an important factor to consider. In order to simplify the voltage stress analysis, the ripple voltage across the capacitors has been neglected. In this regard, it is necessary to calculate the voltage stresses. These equations are given below.

$$V_{stress-S1} = V_{stress-D2} = V_O + V_{c1} \qquad (3.3)$$

$$V_{stress-S2} = V_{stress-D1} = V_{in2} \qquad (3.4)$$

3.4 Experimental results

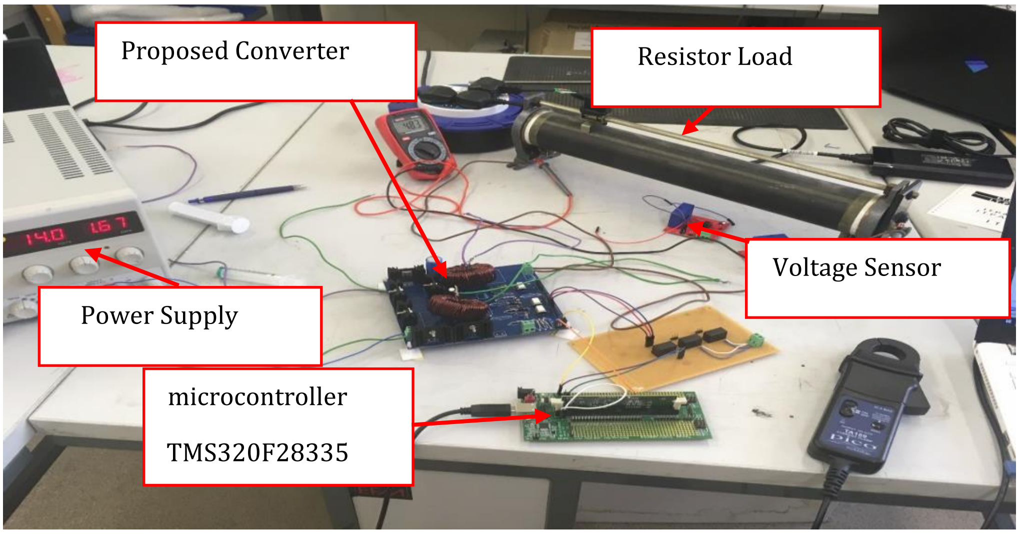

Fig 3.4 Hardware setup.

An experimental hardware prototype is implemented to confirm the feasibility of the converter proposed, and the analysis is done as shown in Fig.3.4. As an alternative to renewable energy sources, a constant voltage source was used in the experiments. Specifications for the circuit are presented in Table 3.1. This table indicates that the first input source is a 10 V, while the second is a 12 V battery. The control system also includes the microcontroller TMS320F28335 as part of its implementation. In this experiment, the output voltage is set to 48 V. A representation of the results is given in Fig. 3.5. The gate signals of the switches can be seen in Fig.3.5 (a) below. Power switches $S_{1,}$ and S_2 are applied with duty cycles of 35 & 75% and 60% & 70%, respectively, when the signals are applied to both power switches.

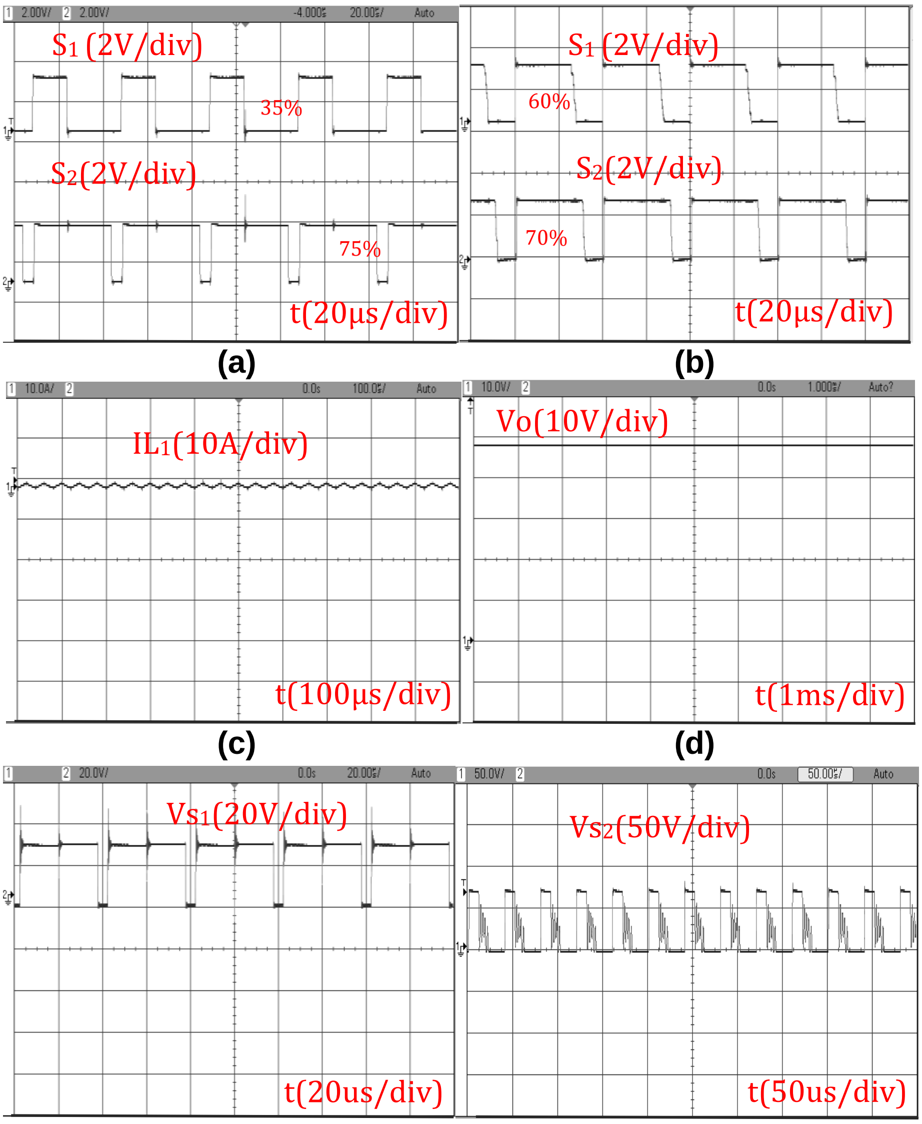

(a) **(b)**

(c) **(d)**

(e) **(f)**

Fig 3.5 Specifications of the circuit, (a), (b) Driver signals, (c), Inductor currents of L1, (d), Capacitors voltage Co, and (e), (f) voltage across switches.

According to Fig.3.5(c) waveform of the input current i_{L1} is shown. Diagram 3.5. (d) shows the voltages across output capacitor C_2. Under the conditions described, it is shown that the output voltage reference is 48 V. As shown in Fig.3.5 (e) and (f), the voltage across the switches is given. The efficiency of the converter being presented is demonstrated in Fig.3.6. As depicted in this figure, the converter exhibits high efficiency across the complete range of load, and the efficiency reaches its maximum value of 92.5% when the load power is 10 W. From the results of the proposed converter, it can be concluded that the theoretical analysis and its feasibility have been validated.

Table 3.1 Parameters of the main prototype.

Parameter	value
V_{in1}	10 V
V_{in2}	12 V
V_o	48 V
L_1	300 μH
L_2	300 μH
C_1, Co	C_1 = 100 μF, C_o= 1000 μF
f_s	25kHz

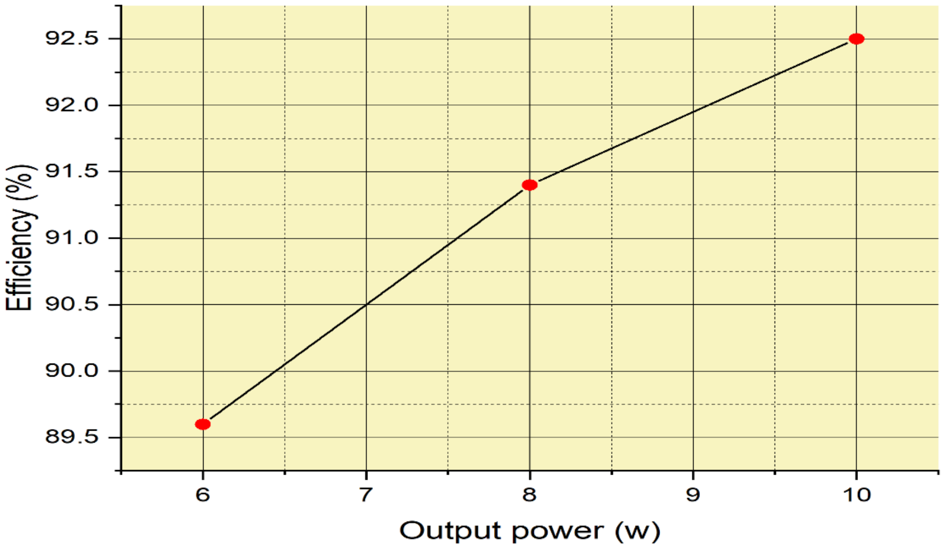

Fig 3.6 The efficiency of the presented converter for various output powers.

Table 3.2 Performance comparison of similar converter topology.

Interpretation	**Proposed Converter**	[113]	[114]	[115]	[116]	[117]	[118]
Power switch count	2	4	2	6	6	3	5
Diode count	2	2	2	6	0	3	5
Inductor count	2	2	1	2	4	2	1
Capacitor count	2	2	2	1	4	1	5
Total component count	8	10	7	15	14	9	16
Number of operating modes	4	5	2	4	2	2	2
Facility to integrate two input sources	Yes	Yes	Yes	Yes	Yes	Yes	Yes
Complexity of circuit	Low	Low	Low	High	High	High	High
Count of conducting devices during each operating mode	Low	Low	Low	High	High	High	Low
Topology	Sepic	Cuk	Buck-Boost	Buck-Boost	Buck, Boost	Boost	Buck-Boost
IPF	Yes	Yes	Yes	No	Yes	Yes	Yes
Input to output flow of power way	shared	shared	shared	shared	shared	shared	shared
fsw(kHz)	20	20-80	15	20	NR	20	20-150
Flow of Power	Buck-Boost	Buck-Boost	No	Buck-Boost	Boost	Boost	Buck-Boost

IPF=independent power

3.5 Comparison with related topologies

The proposed MIC is compared with existing nonisolated MICs in Table 3.2. The most important parameters are the independent power flow from the input sources and the topology of the operation, such as buck, boost, or both buck–boost, as well as the number of components. MIC topologies are defined as buck and boost, indicating a bidirectional converter, which bucks in one direction and boosts in the other. In the MICs in [114] and [116], a high number of components are used in [116], and they are capable of operating in buck and boost modes. There is a lower component count in the MICs in [117] and [113] compared to [114] and [116], but power can be transferred from the input ports only in boost mode. Compared to the proposed MIC, the MIC in [118] appears to have a lower component count, but power flow can only be done in boost mode instead of buck-boost. In addition, there should be eight components in the proposed MIC. There is no doubt that the proposed MIC will have a low number of components, less than 15, which is required by [115], considered the closest competitor in terms of the capability of bidirectional buck-boost operation. There would be fewer components in the MIC in [114] than in the proposed MIC, but it would provide power in only a boost mode and not bidirectionally.

3.6 Extension into Multiple-ports Converter

The circuit diagram in Fig.3.7 illustrates the proposed multi-input DC-DC converter. A new topology is introduced in this section, consisting of a switch and one diode. Thus, an additional input source can be added as a result.

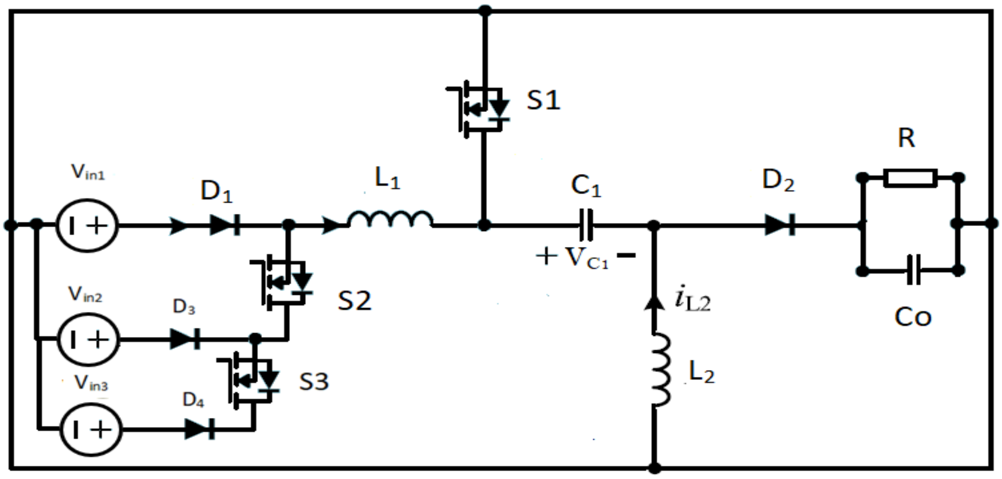

Fig 3.7 Presented multi-input-single-output converter.

3.7 Summary

This chapter proposes designing and implementing a Two-Input–Single-Output DC-DC converter. During the study, the operation of the proposed converter is analysed. In addition, each cell's input current is determined by its duty cycle and is independent of whatever input is used. A set of experimental results is also presented to verify the converter's validity and feasibility among the advantages gained of the proposed topology that it can be applied to clean energy generation systems using MPPT on PV modules or hybrid energy generation systems involving the use of batteries. Several input sources can be added to the proposed topology that can be applied to various applications.

Chapter 4 A Three-Port DC-DC Converter for Integrated PV-Battery Systems

4.1 Introduction

According to the conducted literature review, PV power is limited to the available solar energy, which is uncontrolled. In reality, the MPPT algorithms track the maximum possible power from the exerted solar energy. No solution better than the Energy Storage System (ESS) solves solar energy intermittency [119]. According to [120],[121], the battery requires low maintenance, and its cost becomes reasonable. Based on these reasons, the battery-integrated PV module becomes very attractive, as reviewed in [30],[122],[123]. This chapter aims to propose a new non-isolated three-port DC-DC converter that improves the circuit described in Chapter 3. The proposed circuit is enhanced with a bidirectional power flow port composed of S_3 and diode D_3 to interface with the energy storage unit, as shown in Fig.4.1(a). By integrating an input source with battery storage, this converter will boost its voltage, reduce the effects of solar energy intermittency, and increase solar energy performance. By combining three converters into one, the converter becomes an integrated converter. This converter has higher power density and fewer components compared to traditional DC-DC converters. As part of the development process, a hardware prototype was built and tested to verify the proposed circuit. This converter has been designed as a stand-alone device for applications such as power satellites. As an added benefit, it might be used in electric vehicles.

4.2 Operation Principle

4.2.1 Proposed Circuit

The converter presented has buck-boost characteristics and is suitable for charging and discharging solar panels to maximise power output. This design can be used as a step-down/step-up capability. To control the power of the inputs independently, it is necessary to take advantage of the duty ratios of the switches. The output voltage can also be calibrated to meet the set point by properly charging or discharging the battery. They use a series capacitor to couple energy from the input to the output.

Consequently, short-circuit outputs can be handled more smoothly. The proposed converter consists of two inductors, as shown in Fig.4.1(a). L_1 is connected at the input side of the converter and, by doing so, causes the ripple current in the inputs to be reduced, a continuous input current to be obtained, and a second inductor at an output port. The design includes a SEPIC switch (S_1), a battery charging switch (S_3), a discharging switch (S_2), three diodes D_1, D_2, and D_3, an output port capacitor (C_2), and a coupling capacitor (C_1).

Further, according to the topology synthesis principle in Fig.4.1(a), another integrated three-port converter can be derived based on boost topology, as illustrated in Fig. 4.1(b). This would result in fewer components besides deriving a new three-port converter from the proposed topology synthesis method.

In order to conduct a steady-state analysis, it is necessary to assume the following conditions:

- In order to smooth out the output voltage, coupling capacitor C_1 and the output capacitor C_2 are large enough to provide a smooth voltage.

- All components are ideal, and there is no conversion loss.
- There is no consideration for the battery's internal resistor.

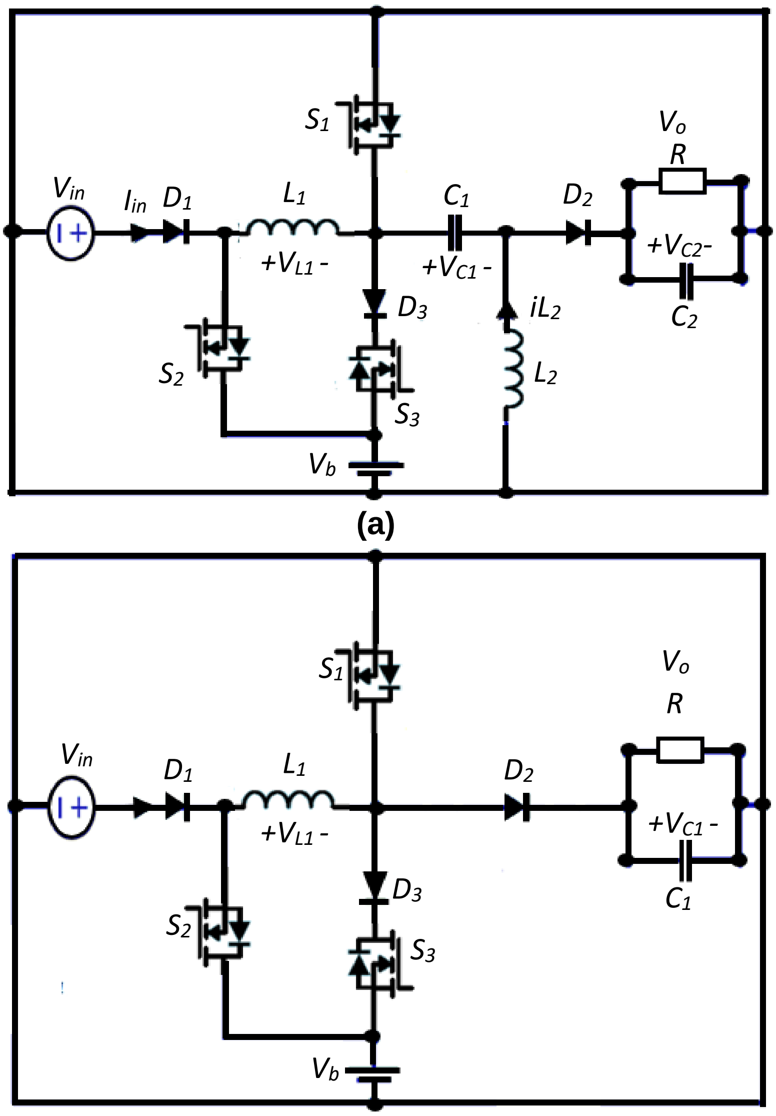

(b)

Fig 4.1 Present converter structure (a) Two-input converter proposed on sepic (b) Two-input converter proposed based on boost.

4.2.2 Operation Modes

There are three possible modes of operation for the converter, each of which will be discussed in this chapter. The next section below explains how a satellite can operate in different modes during its orbital cycle. Based on what is shown in Fig.4.2,

1. Single Input Mode (SIM)

   The battery source in this mode of operation supplies the power to the load. During this operation mode, the input source is not in use as a result of the operation mode. In this mode, the input source is the eclipse period, as depicted in Fig. 4.2(A).

2. Double Input Mode (DIM)

   It is also possible that the input power might not have been able to meet the load adequately due to insufficient input power. As a result, the batteries' discharge is necessary to provide power to the load. In this case, the second mode of operation is applicable, as seen in Fig. 4.2(B).

3. Double Output Mode (DOM)

   DOM will become active as soon as the input source produces a higher output power. The battery circuit must be open to being charged in this case. At this stage of the process, power is provided to the battery by the input source, as depicted in Fig. 4.2(C).

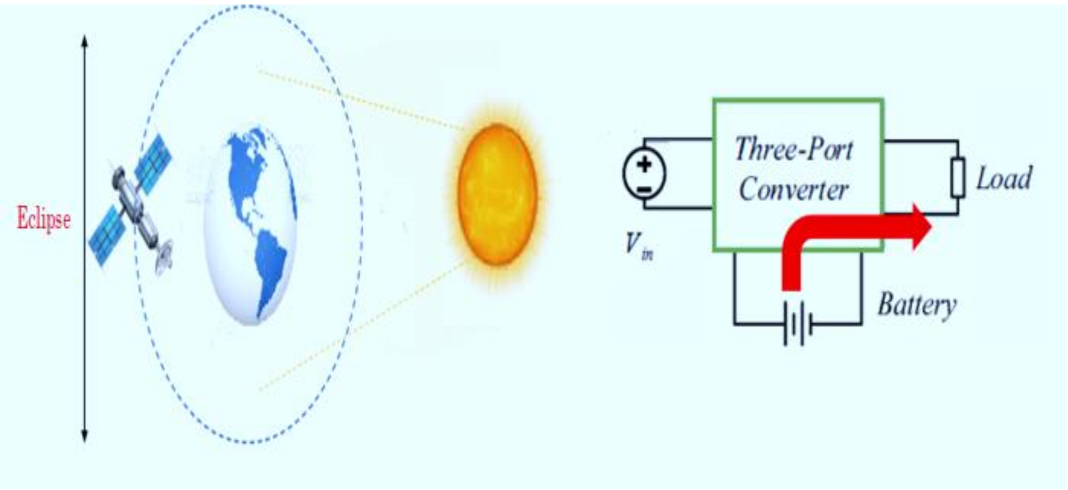

stage (A) Operation (eclipse).

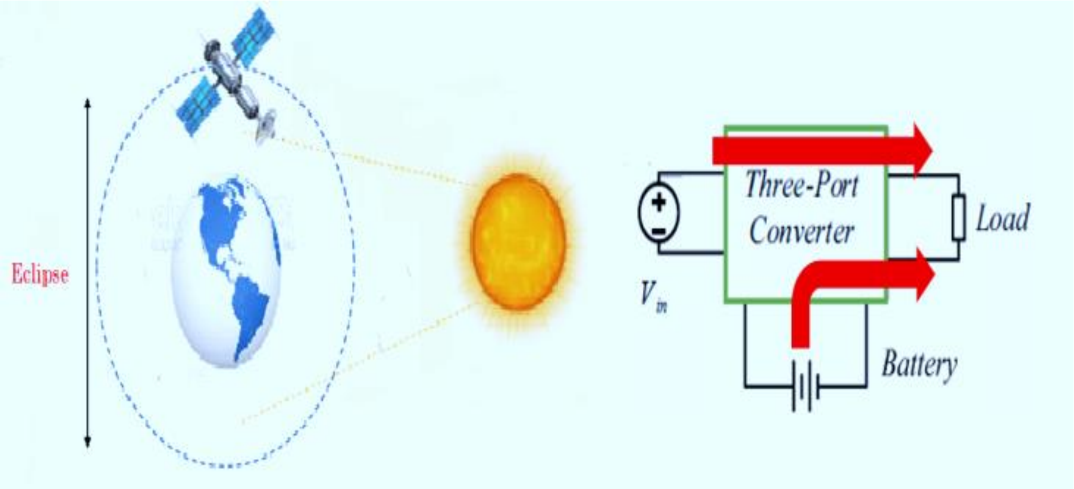

Stage (B) operation (the initial insolation).

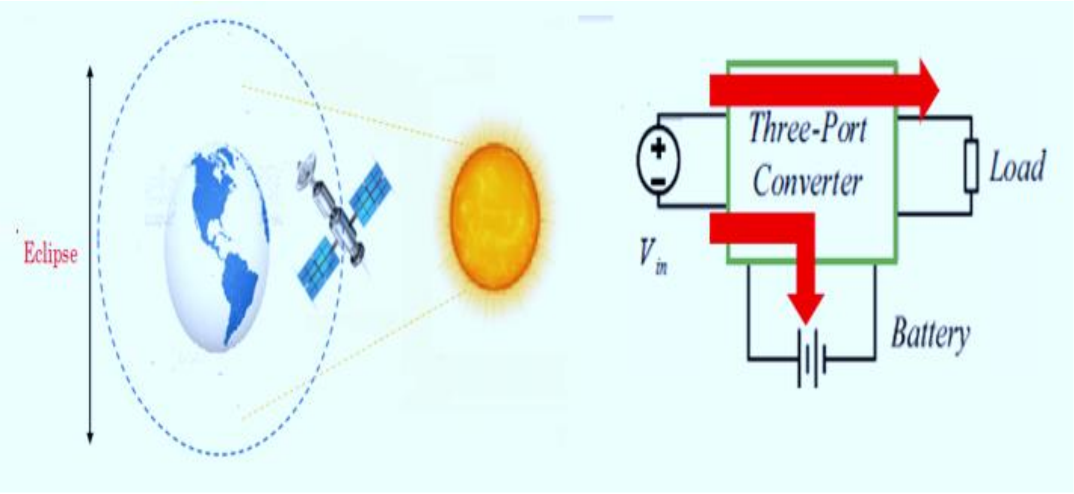

Stage (C) operation (increased insolation).

Fig 4.2 Three possible modes of operation for the converter.

4.2.3 Steady-State Analysis

1. Double Input Mode (DIM):

To enhance the input, the battery discharging is essential for the load to achieve a high energy level. This means that when the battery is discharged, both Vin input source and the battery produce energy that will feed the load. To accomplish this goal, the current only has one path (through S_2) that could be followed. As a result, the amount of discharge is controlled by the duty cycle of switch S_2 and the duty cycle of switch S_3 which is off state when discharge occurs. It is shown in Fig.4.3 that the proposed converter exhibits a switching pattern and a steady-state waveform at steady-state. It is during this state that three types of operation modes will be described in the following manner:

State 1 ($t_0 < t < t_1$): This mode allows the power switches S_1 and S_2 to be turned ON simultaneously while S_3 is kept OFF. The switch S_2 has been turned ON, causing the diode D_1 to be reverse-biased. As a result of switch S_1 is turned ON, the diode D_2 is reverse biased. It is evident that, in this interval, the battery power source energies the inductor L_1 during operation. During this mode, the capacitor C_2 discharges to provide power to the load. It can be seen in Fig. 4.5(a). how the current flows through the converter

State 2 ($t_1 < t < t_2$): During this interval, S_1 is ON, and S_2 and S_3 are OFF. Due to reverse-biased voltages, the diode D_2 is not operating. i_{L1} increases linearly as energy is absorbed by L_1. The capacitor C_1 charges L_2 respectively, and the i_{L2} increases linearly. During this mode, the capacitor C_2 discharges to provide power to the load. Fig.4.5(b) shows the current flow paths in the converter.

State 3 ($t_2 < t < t_3$): During this interval, all three power switches S_1, S_2 and S_3, are OFF. Through C_1 and D_2, L_1 releases energy to load R. Also, in this case, L_2

releases energy to load R. This results in linear decreases of i_{L1} and i_{L2}. According to Fig.4.5(c), the converter's current flow paths can be seen. By applying the voltage-second balance to the inductors. Hence, the output voltages can be deduced for this mode as follows.

$$V_{bat} d_1 + V_{in}(d_1 - d_2) - (V_{in} - V_{C1} - V_o)(1 - d_2) = 0 \tag{4.1}$$

$$V_{C1} d_1 - V_o(1 - d_1) = 0 \tag{4.2}$$

$$V_O = \frac{d_1[V_{bat}\, d_2 + V_{in}\,(1 - d_1)]}{1 - d_1} \tag{4.3}$$

2. Double Output Mode (DOM):

It is important to note that, in DOM, the Input source is used in two ways: to supply power to the load V_o and as a V_{bat} battery charging source simultaneously. In this case, switch S_2 is always turned OFF. The battery acts as an output. The battery can charge overabundant power generated by the Vin input source. One switching cycle can have three possible switching states. It is shown in Fig. 4.4. which is the steady-state waveform of the gate signals for the switches and the inductor currents i_{L1} and i_{L2}. Fig.4.6 shows the equivalent circuits for each state. During this operation mode, three types of states will be described the as follow:

State 1 ($t_0 < t < t_1$): As a result of this interval, S_1 is ON, and S_2 and S_3 are OFF. Due to reverse-biased voltages, the diode D_2 is not operating. i_{L1} increases linearly as energy is absorbed by L_1. The capacitor C_1 charges L_2 respectively, and the i_{L2} increases linearly. During this mode, the capacitor C_2 discharges to provide power to the load. Fig.4.6(a) shows the current flow paths in the converter.

State 2 ($t_1 < t < t_2$): During this interval, S_1 is OFF, and S_3 is ON. It is similar to switching mode 1. Diode D_2 is reverse-biased. Both the input source and the L_1 are used to charge the battery. L_1 releases energy, resulting in a decrease in i_{L1}.

Through capacitor C_1, L_2 releases energy to the battery. Linearly, i_{L2} decreases. During this mode, the capacitor C_2 discharges to provide power to load R. According to Fig.4.6(b), it can be seen the current flow paths of the state.

State 3 ($t_2 < t < t_3$): S_1, S_2 and S_3 are all OFF at this interval. The diode D_2 is switched ON to act as a freewheel diode. As a result of L_1 releasing energy, C_1 and D_2 can load R with energy. In the same way, L_2 releases energy into load R, respectively. There is, consequently, a linear decrease in i_{L1} and i_{L2}. According to Fig. 4.6(c)., the state's current flow paths can be seen. By applying the voltage-second balance to the inductors, the output voltages can be deduced for this mode in the following manner.

$$V_{c1} = V_{in} \tag{4.4}$$

$$V_{C1}d_1 + d_3 (V_{bat} - V_{c1}) + V_o(1 - d_1 - d_3) = 0 \tag{4.5}$$

$$V_O = \frac{V_{in}(d1+d3) - V_{bat}d_3}{1-d_1-d_3} \tag{4.6}$$

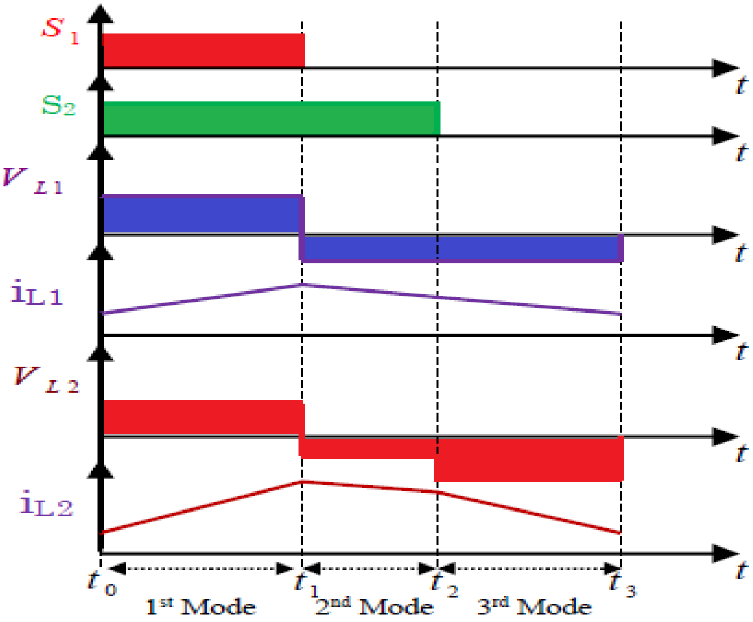

Fig 4.3 The proposed converter's steady-state waveforms DIM.

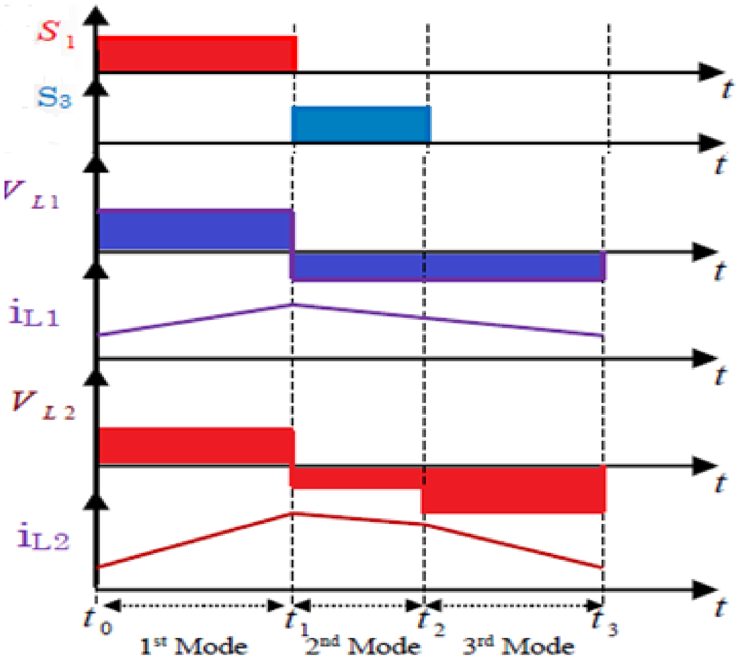

Fig 4.4 The proposed converter's steady-state waveforms DOM.

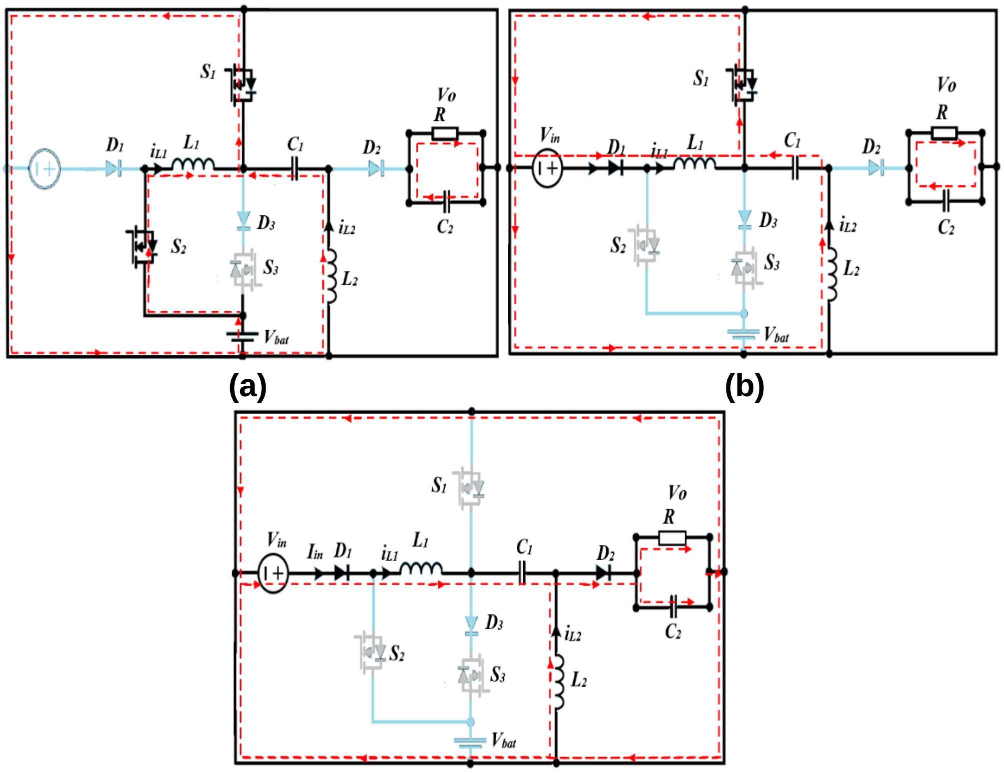

(a) (b)

(c)

Fig 4.5 Different switching states of the DIM:(a) state 1, (b) state 2, (c) state 3.

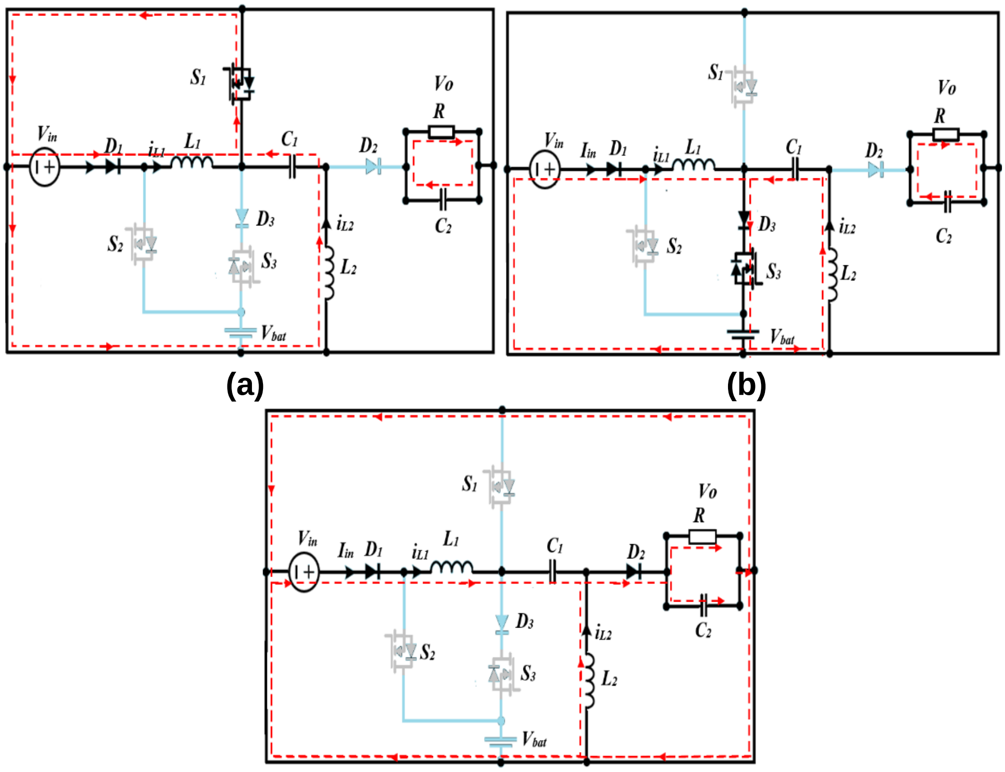

(a) (b)

(c)

Fig 4.6 Different switching states of the DOM:(a) state 1, (b) state 2, (c) state 3.

4.3 Design Considerations

The following parameters will be utilised in this section to discuss the design example:

$$V_O = 48\ \text{V}$$

$$V_{in} = 10\text{~}25\ \text{V}$$

$$V_{bat} = 24\ \text{V}$$

$$f_s = 25\ \text{kHz}$$

4.3.1 Inductor Design

The relationship between voltage and current between the system's ports can be expressed as follows Based on the system's power conservation law.

$$V_{in} I_{in} = I_b V_b + P_O \tag{4.7}$$

$$P_O = \frac{{V_O}^2}{R} \tag{4.8}$$

It can be shown in Table 4.1 that the DC of inductors can be calculated from (4.7,4.8), where I_o output current can be expressed as follows:

$$I_O = \frac{V_o}{R} \tag{4.9}$$

Table 4.1 Dc currents of inductors L1, L2.

$\Delta \boldsymbol{i}_{\boldsymbol{L_1}}$	$\frac{V_{in}\, d_1}{L_{1f_s}}$
$\Delta \boldsymbol{i}_{\boldsymbol{L_2}}$	$\frac{V_o(1-d_1)}{L_{2f_s}}$

Based on the peak-to-peak values for the inductor currents Δi_{L1}, and Δi_{L2} that occur during a switching period, the value of the inductor currents can be calculated using volt second balance, as shown in Table 4.2.

Table 4.2 Currents ripples of inductors L1, L2.

I_{L1}	$\frac{V_o}{V_{in} R_1}$
I_{L2}	$\frac{I_o(1-d_1)}{d_1}$

According to the above results, it is possible to determine the peak value of the inductor current and the average value of the inductor current in all modes. Magnetic saturation can be avoided by designing inductors with moderate losses to avoid excessive losses. As the device parameters vary from mode to mode, all modes should be considered when selecting the inductor specification to ensure that the device is selected according to the maximum values across all modes.

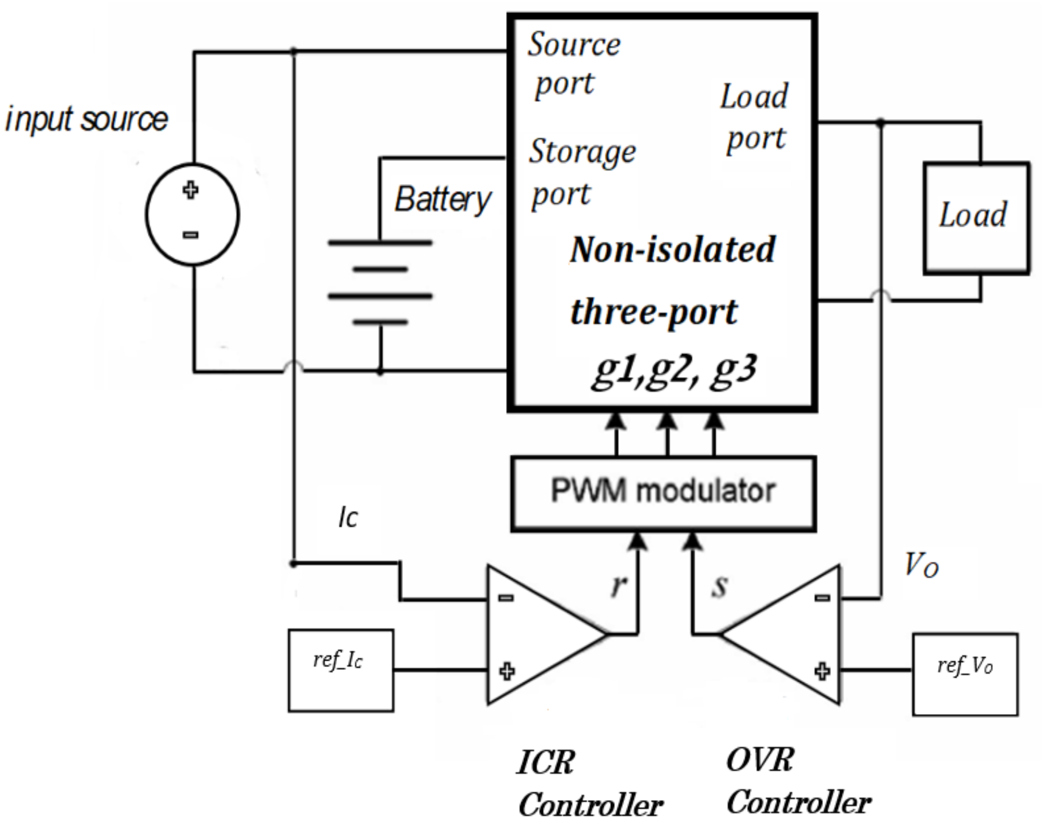

Fig 4.7 Control scheme of the proposed three-port converter [124].

4.3.2 Control Strategy

The drive signals for the switches are produced by a Texas Instrument DSP controller (TMS320F28335) that controls the power flow and produces PWM signals for the switching process. According to the control scheme shown in Fig. 4.7, two feedback controllers are using the two control inputs of the modulator, one controlling the Output Voltage Regulator (OVR) while the other controlling the Input Current Regulator (ICR). As a result of this strategy, it is possible to tighten up the regulation of the load voltage and prevent load transients from affecting the operation of the input source. The ICR loop independently controls the operating current of the input source to match the input source's reference current. A significant role that battery storage plays in this system is balancing the energy by injecting power into the system at heavy loads and absorbing excess power when solar energy is over the demands of the load. A simple PI voltage regulation loop is used to regulate the output voltage by using an OVR.

4.3.3 Power Device Voltage Stress Analysis

Most power electronic device failures occur because of a failure in a semiconductor device. As a result, semiconductor devices must be selected in a manner that enhances their operation quality. Several characteristics must be considered when designing and selecting diodes and switches. During the converter design process, it is essential to consider maximum current flow. As can be seen in Fig. 4.3 and Fig. 4.4, assume the following voltage stresses are calculated as follows:

$$V_{S_1}^{Max} = V_{out} \; ; \; V_{S_2}^{Max} = V_{in} - V_b \; ; V_{S_3}^{Max} = V_{c_1} + V_{out} - V_b \qquad (4.10)$$

$$V_{D_1}^{Max} = V_{in} - V_b \; V_{D_2}^{Max} = V_{out} + V_{in} \; ; \; V_{D_3}^{Max} = V_b - V_{out}; \qquad (4.11)$$

To determine the voltage stresses on all semiconductors, it needs to use the above equations along with (4.10), (4.11) and Tables 4.1,4.2 to protect semiconductors from voltage and current stresses, and they must be selected accordingly.

4.4 Experimental Results

A low-power hardware prototype is implemented to validate the proposed converter's feasibility. The following Table 4.3 lists the parameters used to implement the prototype. The experiments used a constant voltage source instead of a renewable energy source. As seen in this table, the input power source of 10 V and two series batteries of 12 V and 7.4 Ah are considered storage devices. As part of the control system, the microcontroller TMS320F28335 is also implementing the control system. In this experiment, the output voltage is set at 48 V. An experimental setup is provided in Fig. 4.8. Experimental waveforms are illustrated in Figs 4.9-4.15. Specifically, the proposed converter can operate in two different modes.

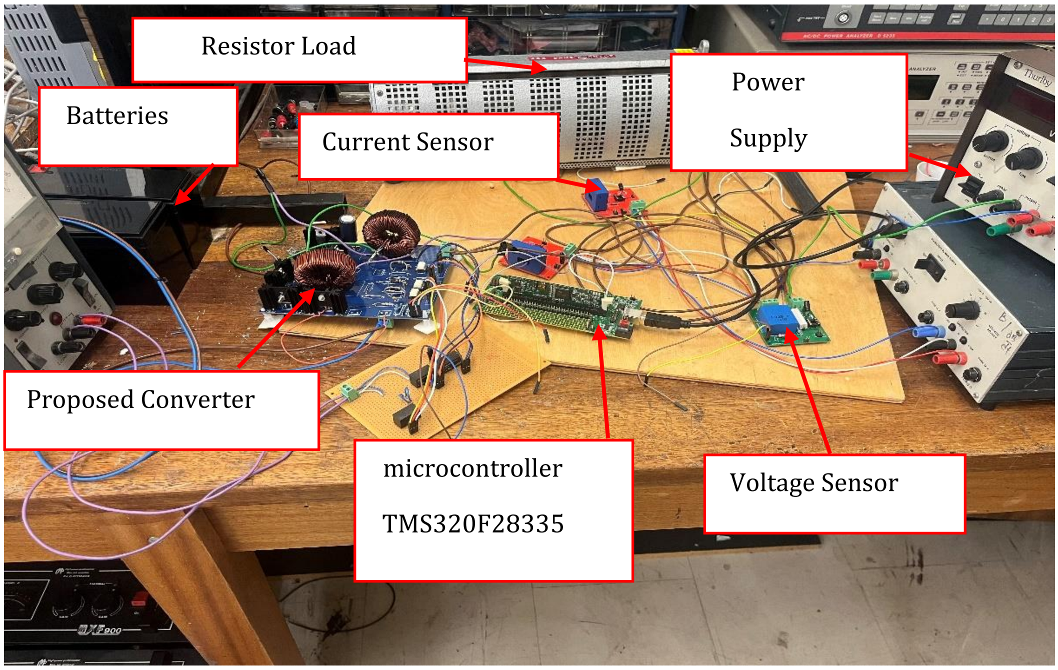

Fig 4.8 Hardware set up.

Dual-input mode is activated when V_{in} cannot fully or partially supply the load. To regulate the output voltage, therefore, the battery must be discharged. By using the power switch S_2, the battery discharging mode can be controlled. As can be seen in Figs. 4.9-4.11, the results of the experiments conducted in this mode of operation are shown. The gate drive of two switches, S_1 and S_2, are shown in Fig. 4.9(a). As illustrated in Fig 4.9(b), the output voltage is 48V. In Fig.4.10 (a), (b), the inductor currents i_{L1} and i_{L2} are shown, respectively. In addition, the battery current is shown in Fig.4.11(a), and the voltage stress on the switches is also shown in Fig.4.11(b)(c). Only the battery voltage is stressing the power switch S_2. This means it can reduce power losses by using a switch with a relatively low $R_{DS\ (on)}$ power. As a result of the experimental results, the presented converter appears to operate properly under various operational conditions.

In Figs. 4.12-4.15, the results of the experiments conducted for dual output mode. The switch S3 and diode D3 will be activated. As shown in Fig. 4.12(a), the gate-driving waveform of switches S_1 and S_3 is also shown. Based on Fig.4.12(b), the output voltage reference is 48 V. Fig.4.13 (a), (b) illustrates the currents flowing through the inductor L_1 and L_2, respectively. A typical waveform of voltage stress is depicted in Fig.4.14 for switches S_1 and S_3. According to Fig. 4.15(a), the voltage stress on the diode D_3 can be seen. The battery charging current is shown to be pulsating in Fig.4.15(b).

The conversion efficiency of the presented converter is shown in Fig.4.16. The figure shows that the converter's efficiency is high throughout the full range of load, and the highest efficiency, 92.5%, is achieved when the load power is 10. Several advantages have been outlined in [125] concerning using pulsating currents for charging batteries. Because of the voltage and the current, all waveforms agree with the previous analysis. Experimental results have shown that the converter can be applied to various applications in various fields in both operation modes.

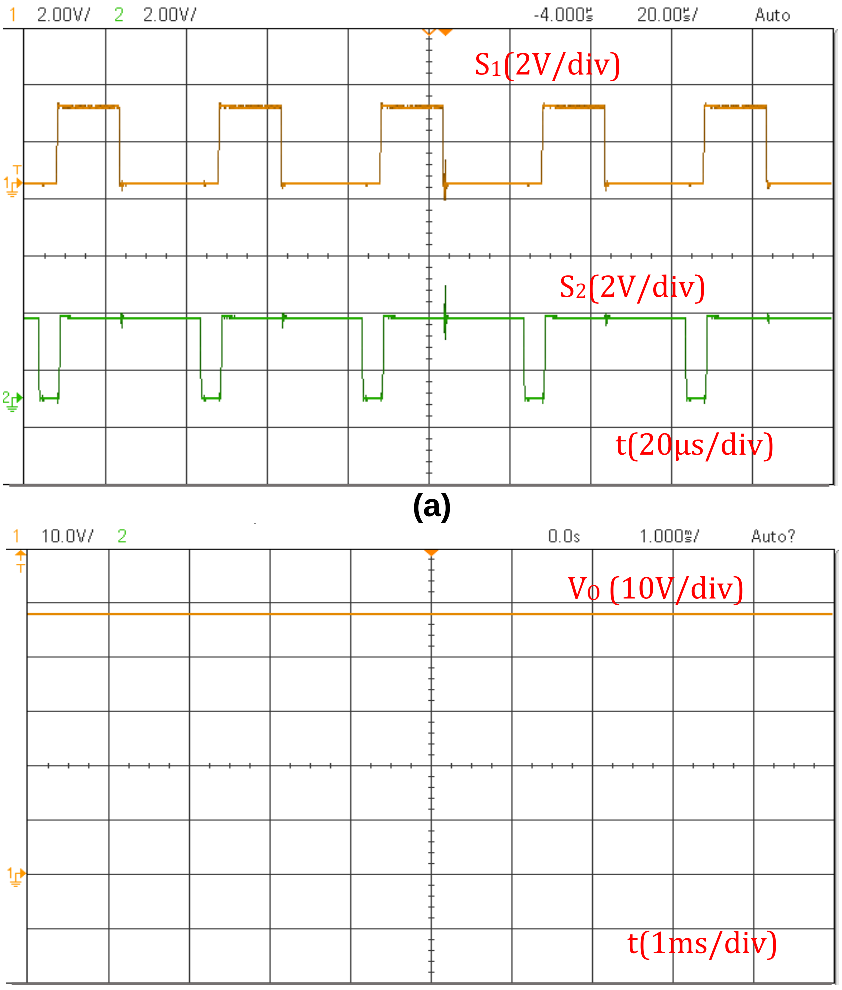

(a)

(b)

Fig 4.9 Results of the experiment in DIM (a) gate driving signals, (b) Output voltage Capacitor.

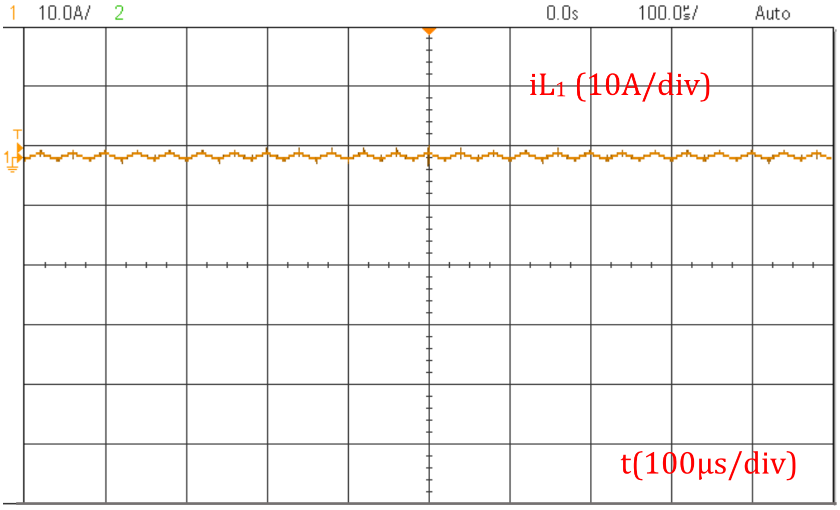

(a)

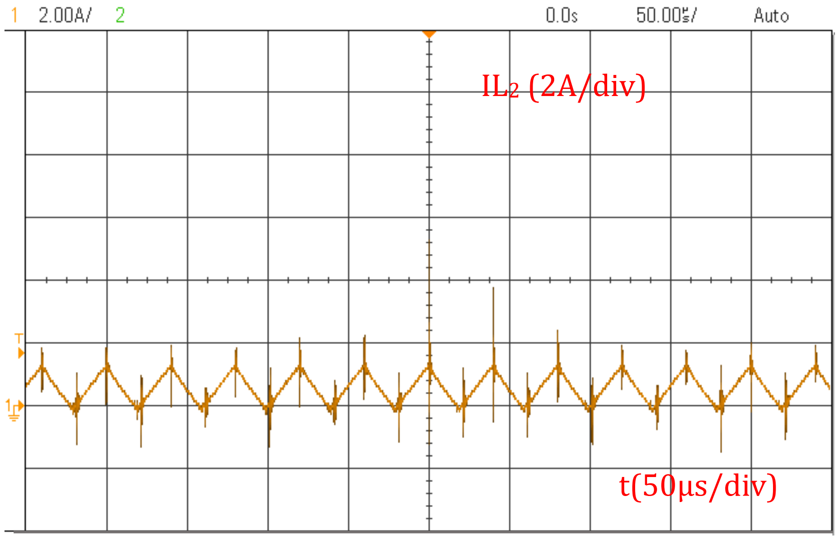

(b)

Fig 4.10 Results of the experiment in DIM (a) inductor current of L1 (b) inductor current of L2.

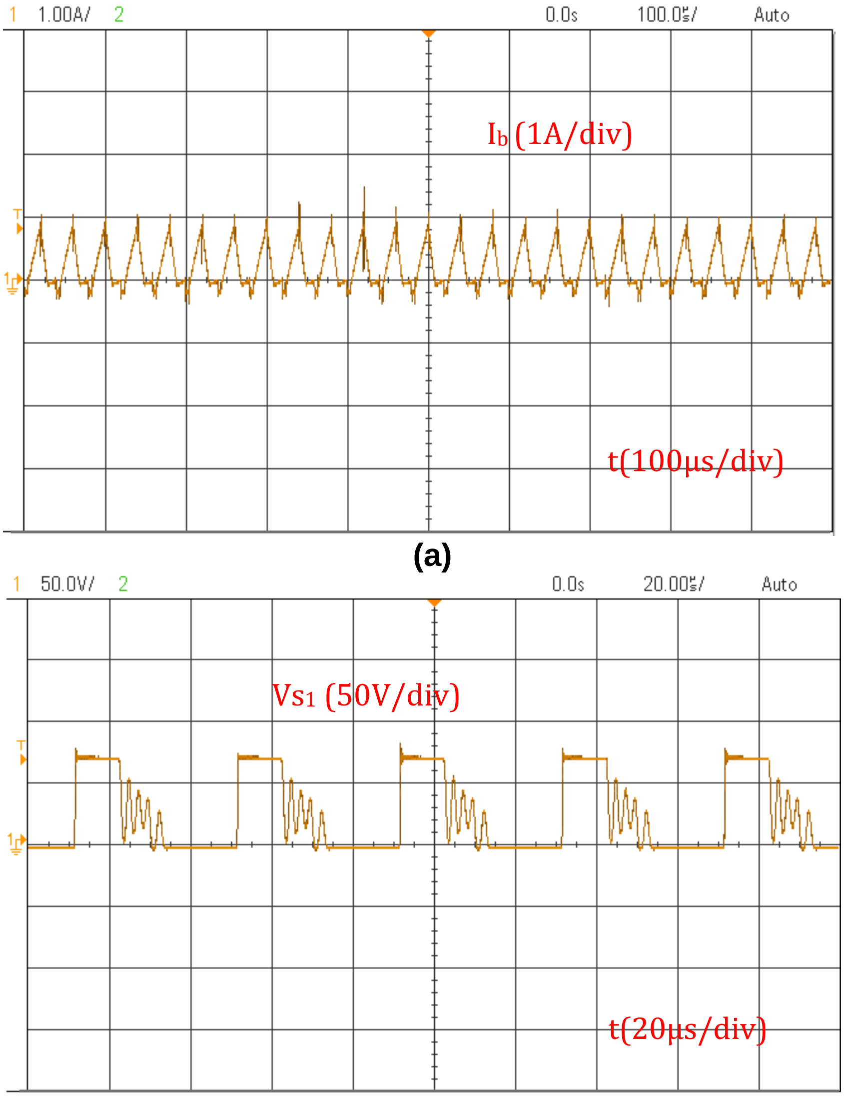

(a)

(b)

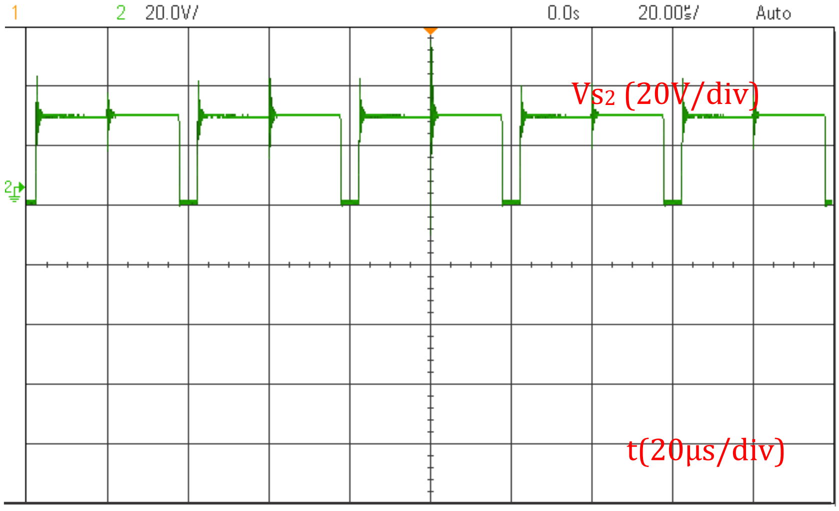

(c)

Fig 4.11 Results of the experiment in DIM (a) battery current, (b) and (c)Power switch voltage stresses.

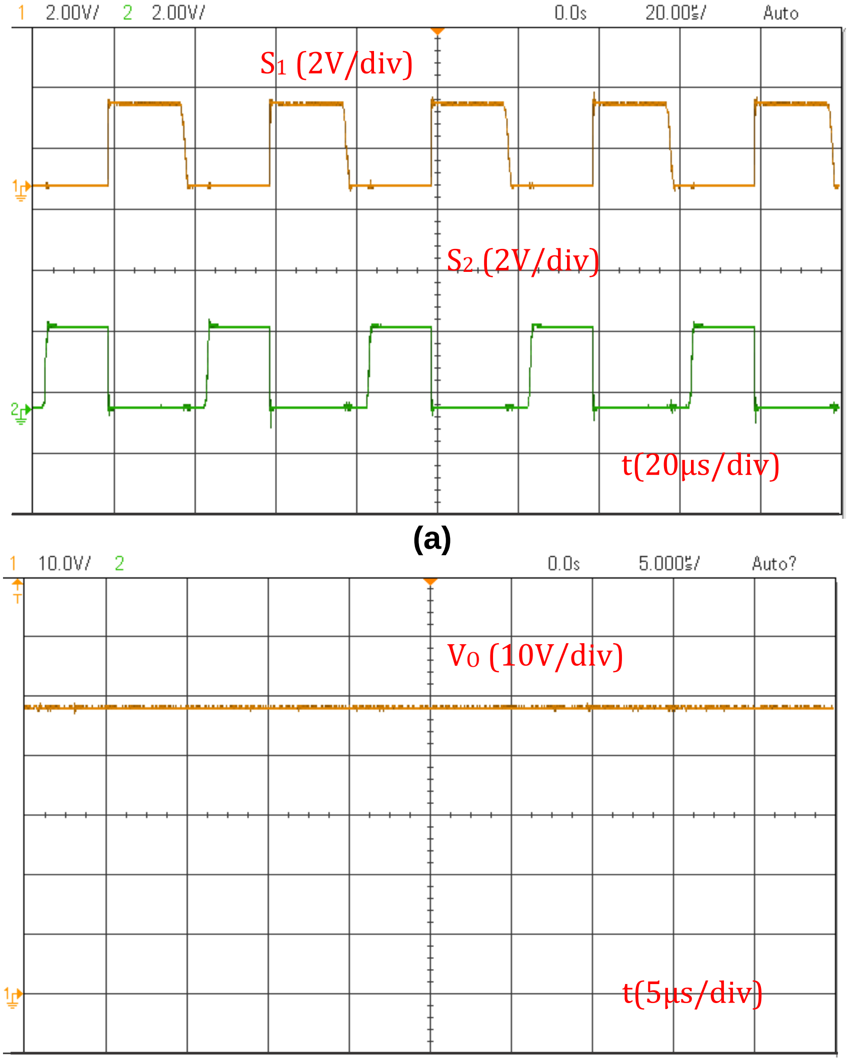

(a)

(b)

Fig 4.12 Experimental results in DOM (a) gate driving signals (b) output voltage.

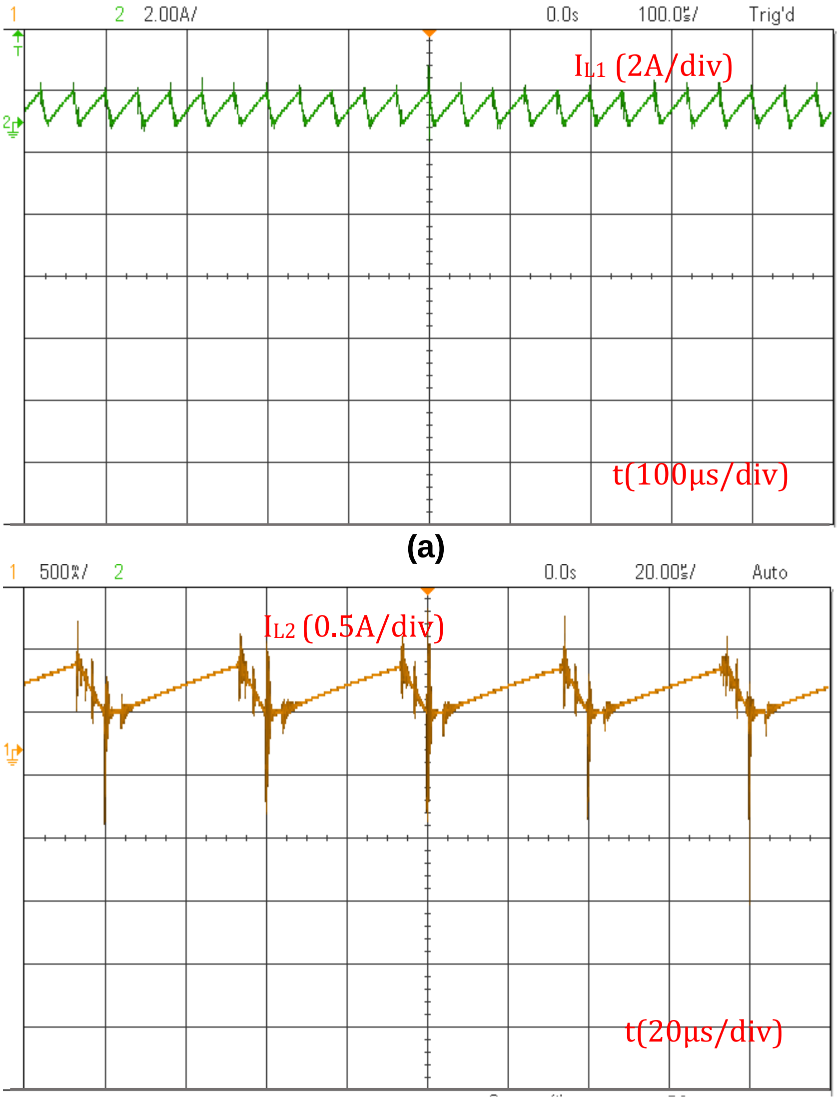

(a)

(b)

Fig 4.13 Experimental results in DOM (a) inductor Current of L1 (b) inductor current of L2.

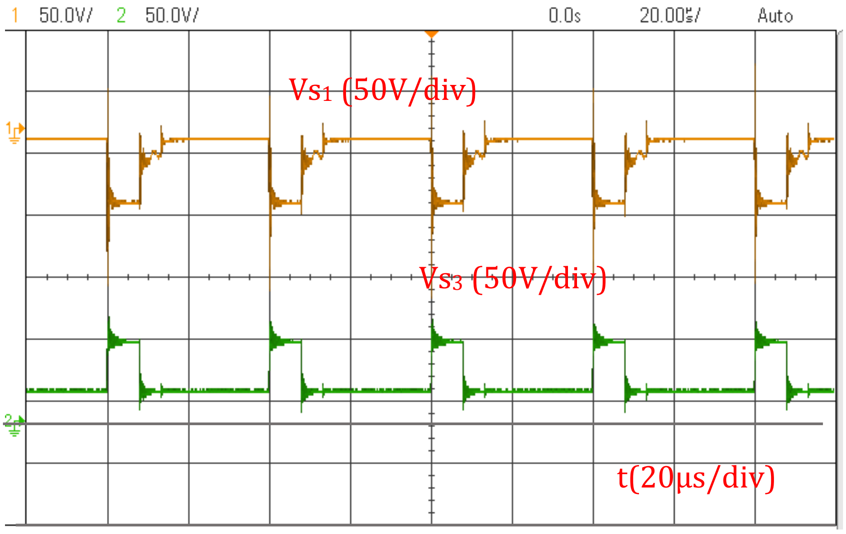

Fig 4.14 Experimental results in DOM Power switch voltage stresses.

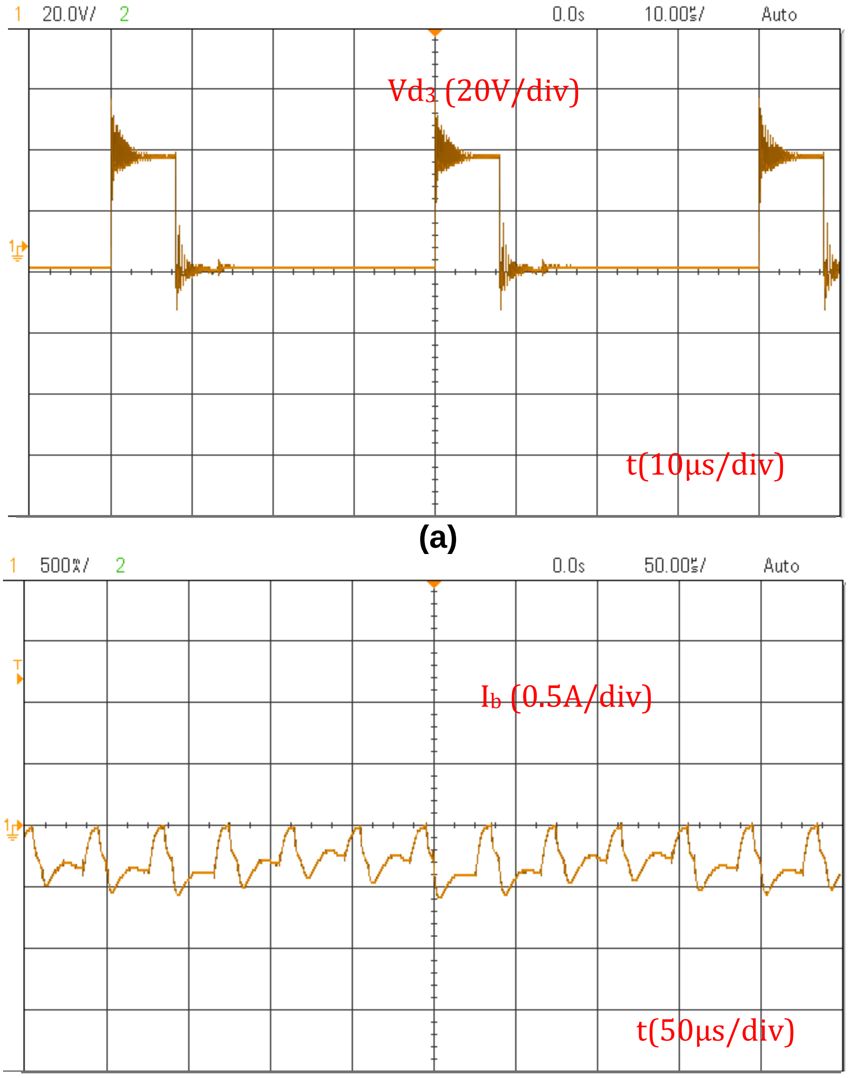

(a)

(b)

Fig 4.15 Experimental results in DOM (a) Diode voltage stresses (b) battery current.

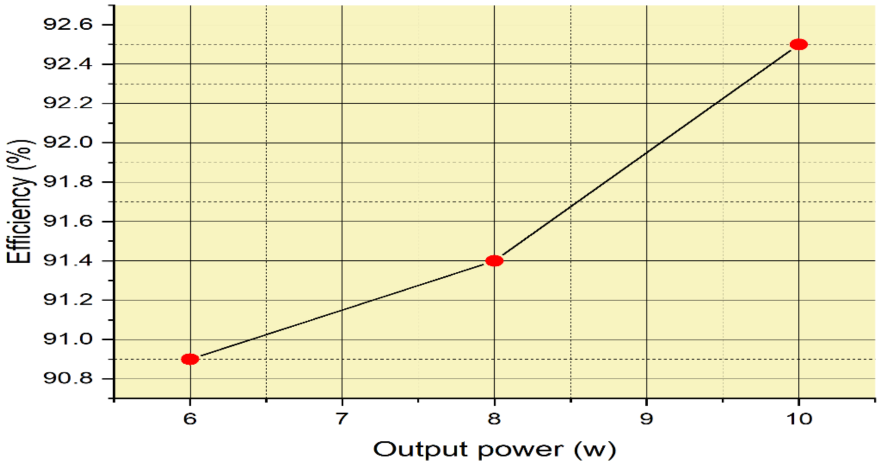

Fig 4.16 The efficiency of the presented converter for various output powers.

4.5 Performance Comparison

Table 4.5 highlights the differences between the proposed DC-DC three-port converter and similar topologies: (1) In addition to decreasing cost, the proposed converter inductor is not required for a battery port filter, which reduces magnetic elements. (2) Another significant advantage of the proposed topology is that the input current used in the proposed topology is continuous, which can increase the efficiency of the renewable energy utilised. (3) Aside from integrating multiple devices in a single converter and being highly efficient, making it a good choice for various power applications in renewable energy.

Table 4.3 Components Details.

Parameter	Value	Parameter	Value
Output Voltage V_O	48V	Capacitor C_2	1000µF/60V
Battery Voltage V_b	10~20V	Inductors L_1 and L_2	300µH/12A
Input voltage V_{in}	12~24V	Switches S_1, S_2, S_3	Fdp2532
Input current I_{in}	0~1.2A	Diodes D_1, D_2, D_3	DSS16-01A
Switching frequency	25kHz	Controller	TMS320F28335
Capacitor C_1	100µF/50V	---	---

Table 4.4 Operation Modes Selections and Switches Operation Lookup Table.

Modes	Power Condition (W)	S1	S2	S3	Active components
Double Input Mode (DIM)	$P_{PV} + P_B = P_0$	PWM1	PWM2	-	S1; S2; C1; C2; L1 and L2
Double Output Mode (DOM)	$P_{PV} = P_0 + P_B$	PWM1	-	PWM3	S1; S3; C1; C2; L1 and L2

Table 4.5 Comparative analysis of TPCs for different applications with a suggested converter.

	Solution	**No. of components *L/C/S/D***	**Control complexity**	**The current state of the battery**	**The current state of the input source**
SEPIC-based three-port converter	Proposed topology on Fig. 4.1(a).	2/1/3/2	simple	discontinuous	continuous
	[125].	2/2/4/1	complex	continuous	discontinuous
	[126].	2/3/4/1	complex	continuous	discontinuous
	[127].	2/2/3/3	complex	discontinuous	continuous
	[128]	2/3/3/4	complex	discontinuous	continuous
Boost-based three-port converter	Proposed topology on Fig. 4.1(b).	2/2/3/3	simple	discontinuous	continuous
	[129].	3/2/3/1	complex	continuous	continuous
		1/1/3/3	complex	discontinuous	continuous
	[130]	2/1/3/0	simple	continuous	continuous
	[131]	2/3/3/5	simple	discontinuous	continuous
	[55]	1/2/5/5	simple	discontinuous	continuous

4.6 Extension into multiple input sources

The proposed converter is capable of hybridising some alternative energy sources, makes it an ideal converter to be considered for use in hybridising alternative energy sources. As a result of this structure, several unidirectional input ports can be made that can be hybridised. Based on Fig.4.17, the converter presented here has a topology in which (m+1) input is connected. Fig.4.17 illustrates a converter with two stages, which deal with the input stage, which connects multiple sources of power to the converter, and the V_{bat} stage, which manages the charge and discharge of the converter's batteries. A total of m + 1 power switches and m + 2 diodes are part of the proposed converter for m-input. Also, two inductors and two capacitors have been used to construct topology.

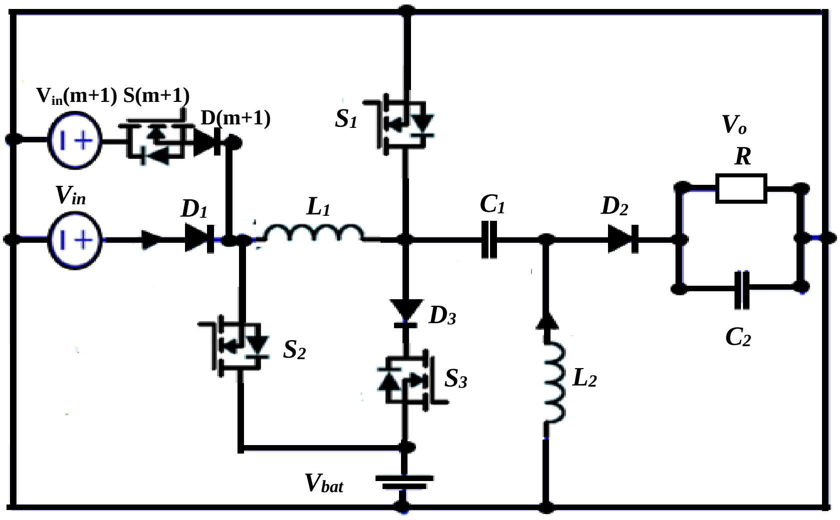

Fig 4.17 Present converter structure of the multiple-input converter proposed.

4.7 Summary

The objective of this chapter is to present a new non-isolated DC-DC converter with two inputs. An in-depth discussion has been given about the operation principle of the converter. Based on the analysis of the presented converter, an optimal port voltage level can be chosen through either buck or boost operating modes. In addition to reducing input current ripples, the SEPIC-based structure provides the TPC with the inherent protection of being able to protect itself against output short circuits due to the series capacitor. The converter presented has a further advantage that it has a simple and cost-effective design because there are no coupled inductors or transformers in the structure. The experimental results verified with the proposed structure demonstrate voltage stresses on switches and diodes. Based on the experimental results, it has been demonstrated that the analysis and converter performance are both viable. Further, the proposed topology can also be applied to the design of multiple input specially designed for different hybrid energy systems as a part of the proposed methodology.

Chapter 5 High gain DC-DC Converter for LED driving and PV applications

5.1 Introduction

In order to meet the ever-increasing energy demand, renewable resources, and energy storage systems have steadily gained acceptance as reliable and low-cost means of generating power [132]. This has led to the integration of non-conventional sources into existing distribution systems. In addition to the growing use of renewable resources, semiconductor devices have advanced, and the energy market has become more competitive, influencing power converter research. In order to increase the power to voltage ratio of many existing low-power renewable resources, a voltage-boosting stage is required [133],[134]. In the literature, several single switch boost converter topologies are proposed, but their major goals are using fewer magnetic elements, smaller sizes, lighter weight, reducing conduction losses, and reducing inductor costs. The voltage stresses on these switches are nearly equal to their output voltage. Rather than modifying an existing converter, it is preferable to integrate the classic DC-DC converter. However, by cascading those classical converters with additional boosting capabilities, the converter circuit's size and cost can be reduced by reducing the power switches and passive elements [135]. This chapter presents a DC-DC converter topology proposed to achieve ten times voltage gain and low voltage stress on semiconductors. To achieve this goal, a new combined Luo-Cuk converter topology on the organic combination of Luo topology and Cuk topology combines the Luo and the Cuk topologies. As well as more than two outputs of different types, the converter can also manage a series output. The operating principles and the design example are described in detail. Experimental results are included to validate the effectiveness of the proposed topology in a high-step-up application.

5.2 Proposed Converter and Operational Principle

5.2.1 Circuit Configuration and Description

By combining their input stages, Fig.5.1 illustrates a new hybrid Luo-Cuk converter. As indicated by the dotted line box 1, this is the Luo converter, and as indicated by the solid line box 2, this is the Cuk converter. Compared to the classical Luo or Cuk converters, this new converter is distinguished using just one switch Q and the extension of the static gain voltage compared to the classical converters.

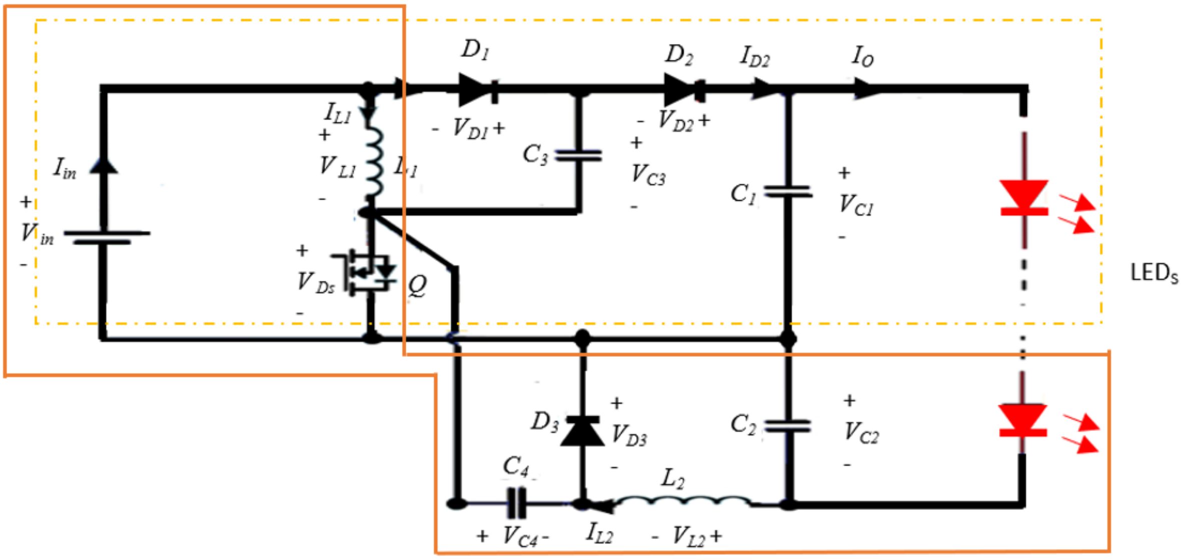

Fig 5.1 Proposed converter.

5.2.2 Converter Principle of Operation

In a combined Luo-Cuk converter, not only can the two types of outputs be produced, but they can also be produced as a series output. Below is an example of an analysis of the series output of the two outputs, which illustrates the concepts of the working principle. Based on the assumption that current is continuous in the inductor and all components are ideal, the combined Luo-Cuk converter has two modes of operation in one switching cycle.

In operating mode [I]: which can be found in Fig.5.2(a), When the switch Q and D_1 are turned ON, the inductors L_1 and L_2 are in the charging mode. Meanwhile, the capacitor C_4 is in the mode of discharging. D_2 and D_3 are respectively blocked by the negative voltages from V_{C1} and V_{C4}, and the voltages across the inductors L_1 and L_2 are:

$$V_{L_1} = L_1 \frac{di_{L1}}{dt} = V_{in} \tag{5.1}$$

$$V_{L_2} = L_2 \frac{di_{L2}}{dt} = V_{C_4} - V_{C_2} \tag{5.2}$$

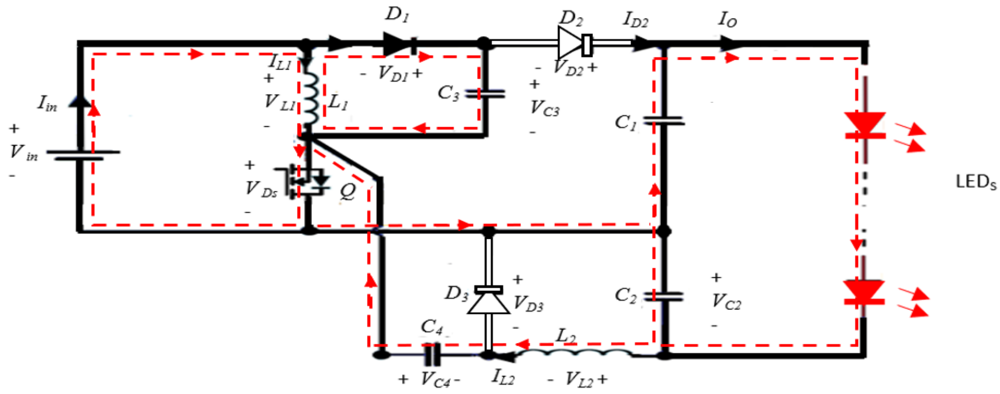

(a) Operation mode I

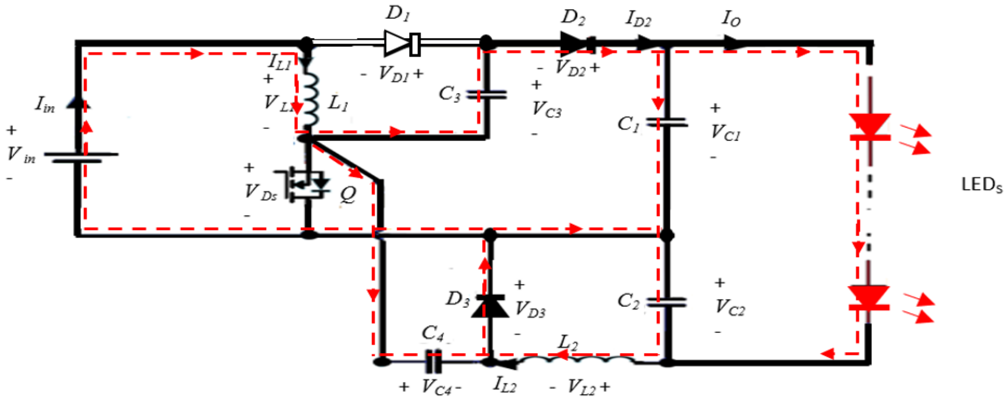

(b) Operation mode II

Fig 5.2 Equivalent circuits of the switching modes (a) Operation mode I, (b) operation mode II.

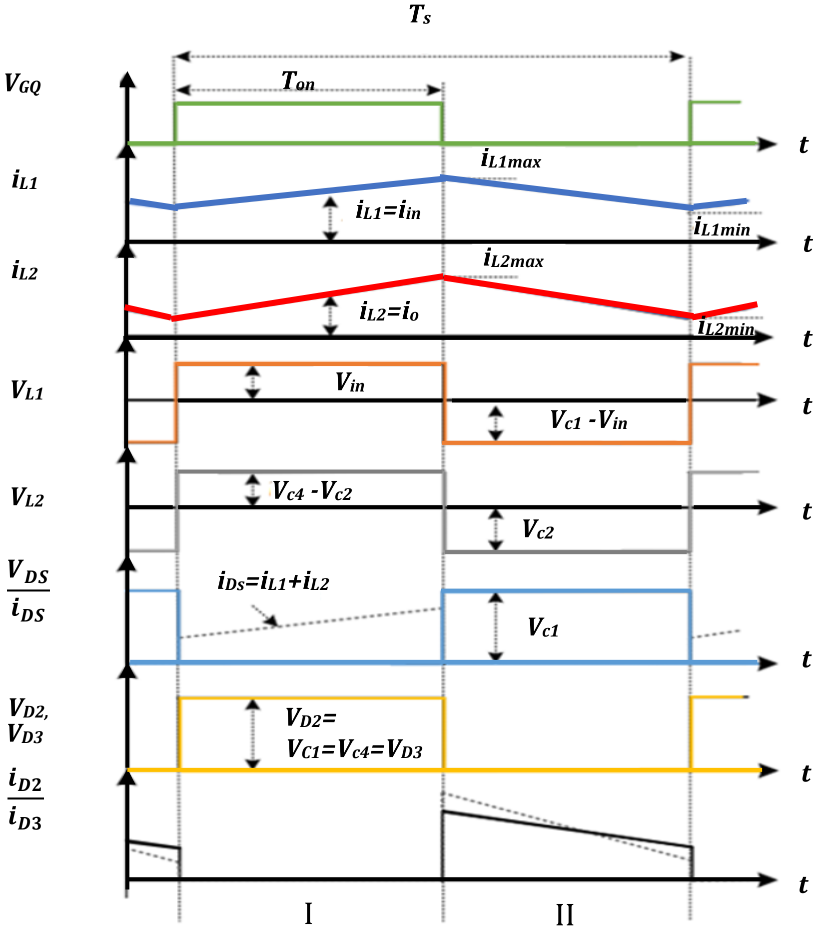

Fig 5.3 Key waveforms based on complementary control.

When $t = T_{on} = DT_S$, i_{L_1} reaches the maximum value $i_{L_{1\max}}$. During the conduction period of the switch Q, the increment i_{L_1} of the current $\Delta i_{L_1} \uparrow$ Is:

$$\Delta i_{L_1} \uparrow = \frac{V_{in}}{L_1} DT_S \tag{5.3}$$

At the same time, i_{L_2} also reaches the maximum value i_{L_2} max, the increment of $\Delta i_{L_2} \uparrow$ Is:

$$\Delta i_{L_2} \uparrow = \frac{V_{C_4} - V_{C_2}}{L_2} DT_S \tag{5.4}$$

At this time, the LEDs are powered by capacitors C_1 and C_2, and the current flowing through the switch Q is:

$$i_{D_S} = i_{L_1} + i_{L_2} \tag{5.5}$$

In operating mode [II] is shown in Fig.5.2(b). When switch Q and D_1 are turned OFF, diodes D_2 and D_3 are turned ON, and the power supply and the inductor L_1 release energy simultaneously. However, diode D_2 supplies power to the capacitor C_1. Meanwhile, the capacitor C_4 charges by L_1 and the capacitor C_2 by the inductor L_2 through the diode D_3. The inductor currents i_{L1} and i_{L2} both decrease linearly, and the voltages across the inductors L_1 and L_2 are:

$$V_{L_1} = L_1 \frac{di_{L1}}{dt} = V_{C_1} - V_{in} = V_{C_4} - V_{in} \tag{5.6}$$

$$V_{L_2} = L_2 \frac{di_{L2}}{dt} = V_{C_2} \tag{5.7}$$

At this point, the current flowing through diode D_3 is:

$$i_{D_3} = i_{c_4} + i_{L_2} \tag{5.8}$$

During the OFF period of the switch Q, the reduction $\Delta\, i_{L_1} \downarrow$ of the current i_{L_1} in the inductor L_1 is:

$$\Delta\, i_{L_1} \downarrow = \frac{V_{c_4} - V_{in}}{L_1}(1 - D)T_s \tag{5.9}$$

Due to the release of energy from the inductor L_2 , the current flowing through L_2 decreases, and its decrease $\Delta\, i_{L_2} \downarrow$ During this period is:

$$\Delta\, i_{L_2} \downarrow = \frac{V_{c_2}}{L_2}(1 - D)T_s \tag{5.10}$$

When D > 0.5, the Luo link and the Cuk link can be boosted simultaneously, and when D < 0.5, it can be to achieve the boost of the Luo link while the Cuk link is stepped down.

5.3 Steady State Performance Analysis

5.3.1 Steady-state voltage gain

According to the volt-second balance principle of the inductor L_1, the following equation is obtained:

$$V_{in}\mathrm{DT}_s = \left(\mathrm{V}_{c_1} - V_{in}\right)(1 - \mathrm{D})\mathrm{T}_s \tag{5.11}$$

$$V_{in}\mathrm{DT}_s = \left(\mathrm{V}_{c_4} - V_{in}\right)(1 - \mathrm{D})\mathrm{T}_s \tag{5.12}$$

From equations (5.11) and (5.12), the voltage across capacitors C_1 and C_4 can be obtained:

$$\mathrm{V}_{c_1} = \mathrm{V}_{c_4} = \frac{V_{in}}{1-D} \tag{5.13}$$

According to the volt-second balance principle of the inductor L_2, the following equation is obtained:

$$\left(\mathrm{V}_{c_4} - \mathrm{V}_{c_2}\right)\mathrm{DT}_s = \mathrm{V}_{c_2}(1 - \mathrm{D})\mathrm{T}_s \tag{5.14}$$

The voltage across the capacitor C_2 can be obtained from equation (5.14) :

$$\mathrm{V}_{c_2} = D\,\mathrm{V}_{c_3}\frac{D}{1-D}V_{in} \tag{5.15}$$

$$\mathrm{V}_o = \mathrm{V}_{c_1} + \mathrm{V}_{c_2} \tag{5.16}$$

(5.16) and (5.13)，(5.15) and (5.16)， The steady-state voltage gain of the converter can be derived:

$$\mathrm{M} = \frac{\mathrm{V}_o}{\mathrm{V}_{in}} = \frac{I_o}{I_{in}} = \frac{1+D}{1-D} \tag{5.17}$$

Fig.5.4 shows the relationship between the voltage gain and the duty cycle of the combined Luo-Cuk, Luo, and Cuk converters. It can be seen from the figure that the voltage gain of the combined Luo-Cuk converter is higher than the voltage of the Luo and Cuk converters. Compared with the gain, it not only realises the high gain of the output voltage but also is suitable for the lighting system (such as the LED photovoltaic lighting system), which combines the low voltage input source and the LED.

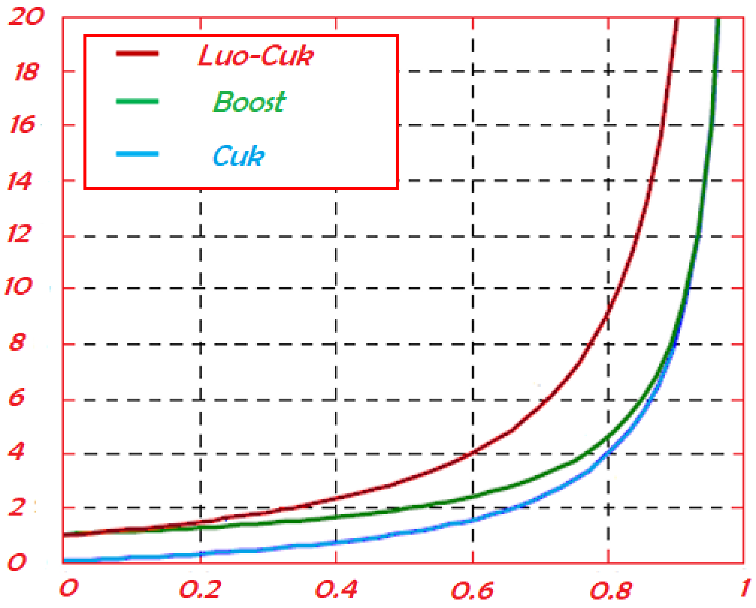

Fig 5.4 Voltage gain versus duty cycle.

5.4 Design Consideration

5.4.1 Inductor design

The calculation of the value of the inductors and the circuit under analysis is carried out to guarantee a certain variation in the average value (Fig.5.3). Generally speaking, the differential equation (5.18) represents the evolution of the current in a coil.

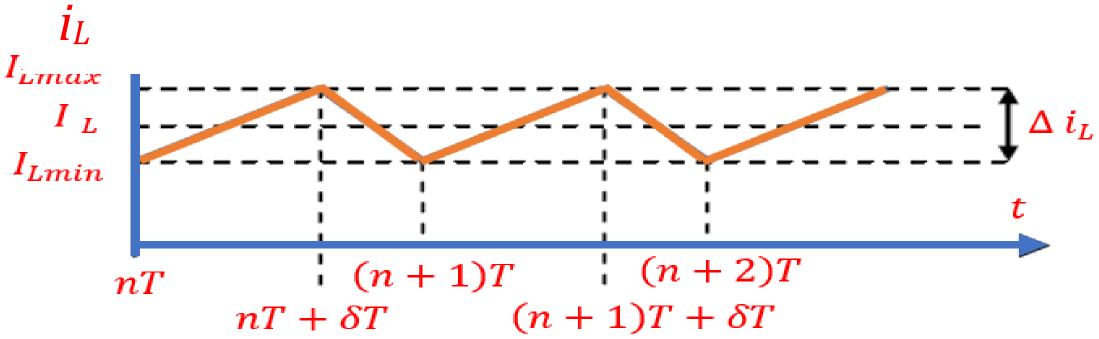

Fig 5.5 Current evolution in the Inductor L1.

$$V_{L_1} = L_1 \frac{di_{L1}}{dt} \tag{5.18}$$

Thus, equation (5.18) now looks like equation (5.19).

$$\frac{\Delta iL}{\Delta t_L} = \frac{V_L}{L} \tag{5.19}$$

Thus, using the instantaneous value of the voltage at the coil terminals, V_L , verified during a certain period Δt_L, it is possible to calculate the value of the coils.

In the case of the coil L_1, V_{L_1}The voltage is given by:

$$V_{L_1} = \begin{cases} V_{in} & nT < t < nT + \delta T \\ U - Vc_1, & nT + \delta T < t < (n+1)T \end{cases} \tag{5.20}$$

Using the first-time interval, we have $\Delta t_L = \delta T$, so:

$$L_1 = \frac{U\delta T}{\Delta i_{L_1}} \tag{5.21}$$

For the coil case L_2, the voltage V_{L_2} Is given by:

$$V_{L_2} = \begin{cases} Vc_1 - Vc_2 & nT < t < nT + \delta T \\ -Vc_2, & nT + \delta T < t < (n+1)T \end{cases} \tag{5.22}$$

Using, in this case, the second time interval, we have $\Delta t_L = (1-\delta)T$, so:

$$L_2 = \frac{Vc_2(1-\delta)T}{\Delta i_{L_2}} \tag{5.23}$$

5.4.2 Sizing of capacitors

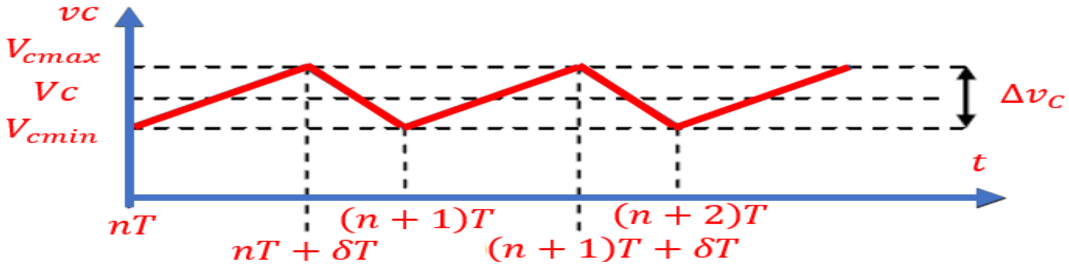

Fig 5.6 Voltage evolution in a capacitor C1.

The calculation of the value of the capacitors C$_1$, C$_2$, and C$_4$ and the circuit under analysis is carried out to guarantee a certain variation Δvc to the average value V$_C$ Fig.5.6. The differential equation (5.24) represents the evolution of the voltage vc(t) in a capacitor.

$$i_c(t) = C\frac{dV_C}{dt} \tag{5.24}$$

Applying the same reasoning in calculating the coils, equation (5.24), after being linearised, presents the aspect of equation (5.25).

$$\frac{\Delta vc}{\Delta t_c} = \frac{i_c}{C} \tag{5.25}$$

Thus, using the instantaneous value of the current in the capacitor, i_c, verified during a certain period Δt_c, it is possible to calculate the value of the capacitors. In the case of capacitor C$_1$, the current i_{c1} is given by:

$$ic_1 = \begin{cases} -I_o, & nT < t < nT + \delta T \\ I_o\frac{\delta}{1-\delta}, & nT + \delta T < t < (n+1)T \end{cases} \tag{5.26}$$

Using the first-time interval, we have $\Delta t_c = \delta T$, so:

$$C_1 = \frac{I_o \delta T}{\Delta v c_1} \tag{5.27}$$

In the case of capacitor C$_3$, the current ic$_3$ is given by:

$$ic_4 = \begin{cases} -I_o, & nT < t < nT + \delta T \\ I_o \frac{\delta}{1-\delta}, & nT + \delta T < t < (n+1)T \end{cases} \tag{5.28}$$

Using the first-time interval, we have $\Delta t_c = \delta T$, so:

$$C_4 = \frac{I_o \delta T}{\Delta v c_3} \tag{5.29}$$

In the case of capacitor C$_2$, its current does not present almost constant instantaneous values during the switching states, contrary to what happens in capacitors C$_1$ and C$_4$, so the above approximation is invalid.

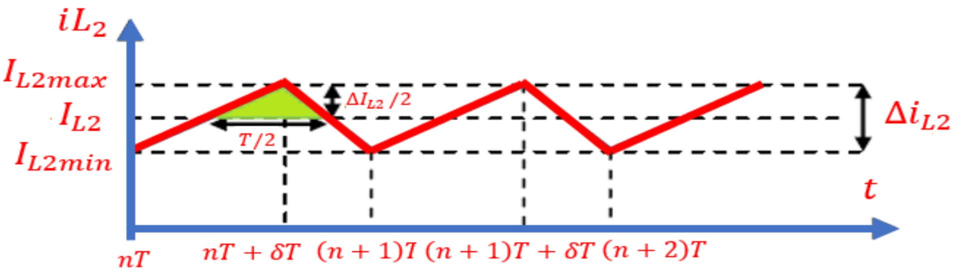

Fig 5.7 Current evolution in the Inductor L2.

From the analysis of Fig.5.7, when the driven semiconductor is conducting, the change in charge ΔQ supplied to the capacitor corresponds to the area of the triangle with height $\Delta i L_2/2$ and base $T/2$ Thus:

$$Q = C\,V_C \rightarrow C = \frac{Q}{V_C} \tag{5.30}$$

With C$_2$ constant:

$$C_2 = \frac{Q}{\Delta V_{C_2}} \tag{5.31}$$

The change in load is then given by:

$$Q = \int i.dt$$

$$\Delta Q = \frac{\frac{T}{2}\frac{\Delta i_{L_2}}{2}}{2} = \frac{T\Delta i_{L_2}}{8} \tag{5.32}$$

Therefore, the value of capacitor C_2 is obtained in this way:

$$C_2 = \frac{T\Delta i_{L_2}}{8\Delta V_{c_2}} \tag{5.33}$$

5.4.3 Choice of Semiconductors

One of the design options that must be taken when sizing converters is the choice of the type of controlled semiconductor to use, depending on the specific application in which it is inserted. Thus, it is common to consider several factors, such as the cost of the device, the voltage and current limit values supported, the complexity of its control circuit, and the frequency at which it will operate, among others. The semiconductor must be selected to withstand the maximum voltages and currents, plus a safety margin of approximately 50%, if possible. Thus, given the study under analysis, I opted for using an n-type reinforcement MOSFET semiconductor. It is a device whose characteristics match the values that will be effectively used in this project. The MOSFET will be oversized, thus ensuring increased safety and reliability. Furthermore, it requires a relatively simple control circuit compared to other devices. As for the remaining semiconductors included in the study, they must be selected considering a safety margin close to that mentioned above.

5.5 Simulation results

Using MATLAB/Simulink and Power System Toolbox, the proposed power converter was tested in steady state. The theoretical analysis is verified by simulating a new combined Luo-Cuk converter according to the parameters presented in Table 5.1 to demonstrate the validity of the theoretical analysis.

Table 5.1 The circuit specifications.

Parameter	Value
V_{in}	7~10 V
V_o	48 V
L_1	300 μH
L_2	300 μH
C_1, C_2, C_3	$C_1 = 470\ \mu$F, $C_2 = 470\ \mu$F, $C_3 = 100\ \mu$F, $C_4 = 100\ \mu$F
f_s	25 kHz

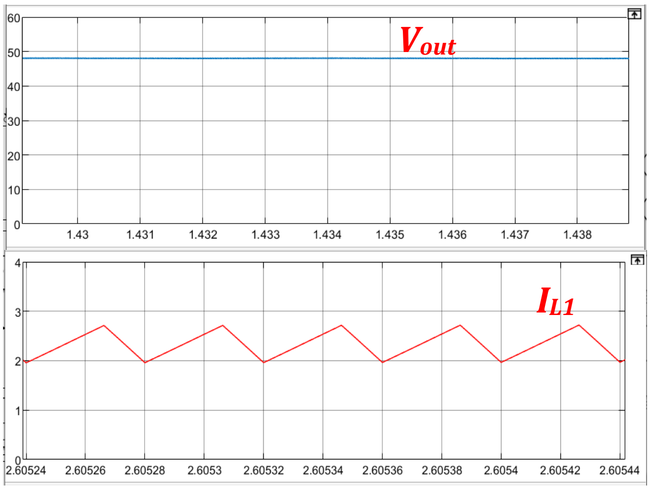

Fig 5.8 Results of simulation of the input current iL1 and output voltage.

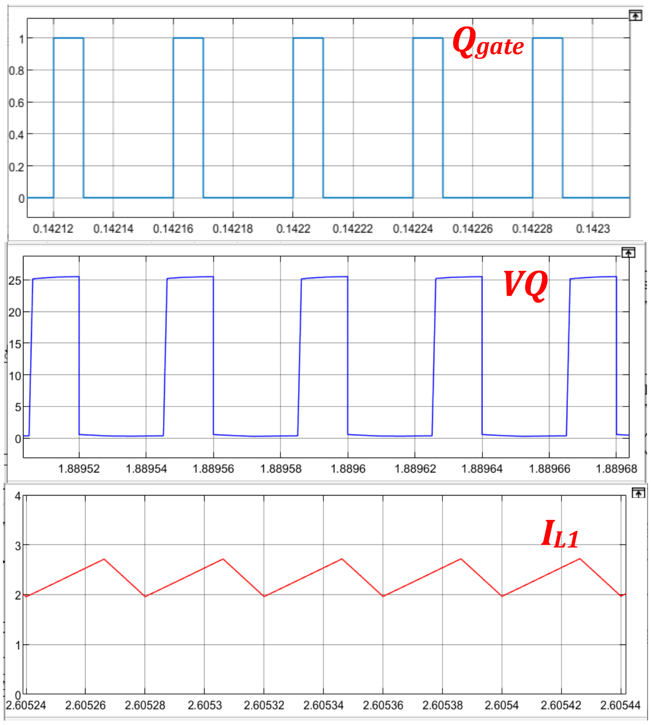

Fig 5.9 The input current of inductor i_{L1} and voltage across the power switch Q.

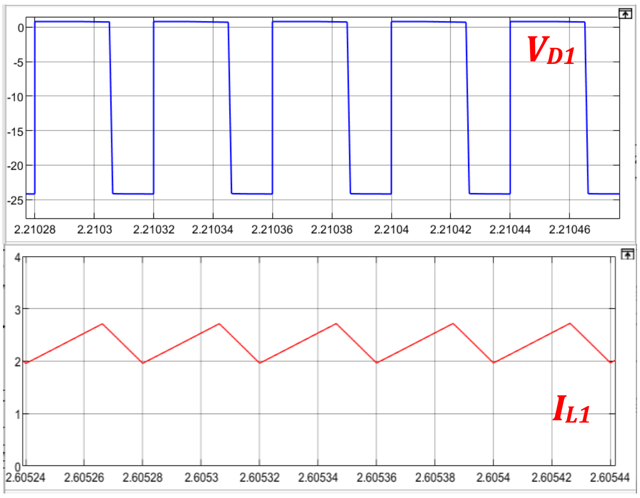

Fig 5.10 Result of simulation of the input current i_{L1} and voltage across diode D1.

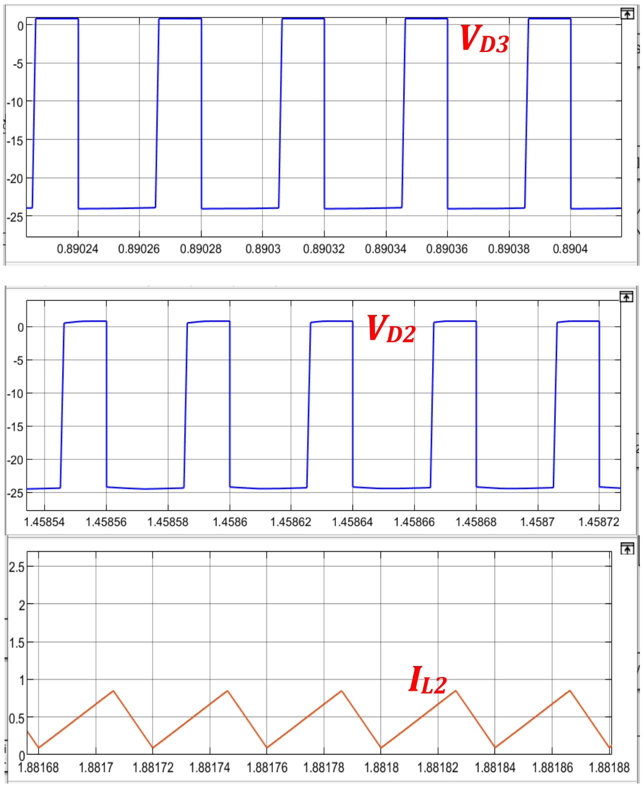

Fig 5.11 Results of the simulation of the output current inductor (iL2) and voltage across two diodes the D2 and D3.

Table 5.2 Analysis of output voltage waveform of the proposed converter.

	Preshoot	**Overshoot**	**Undershoot**	**Rise Time**	**Settling Time**
V_{o1}	30.921%	0.224%	2.081%	41.577ms	72.264 ms
V_{o2}	29.221%	0.322%	2.056%	41.277ms	72.078 ms

According to Fig.5.8, the simulation waveforms of the new combined Luo-Cuk converter show the output voltage at 48V followed by the current of inductor L_1. As is obvious from Fig.5.9, it displays the waveforms of the driving voltage on switch Q and the currents flowing through the inductor L_1. The figure shows a relatively low ripple in the current (the input current ripple) flowing through the inductor L_1. A picture of a switching Mosfet Q and its corresponding voltage stress waveforms. According to Figs 5.10-5.11, The voltage stress waveforms of the diodes D_1, D_2, and D_3 and the current of inductor L_2. The voltage stress on the diodes D_2 and D_3 are consistent with the voltage stress of the switch. It appears that the simulation results agree with the analysis above, which lends credence to the findings of the theoretical analysis. Table 5.2 shows the analysis of output voltage waveform V_o. These results demonstrate the validity of the control performance.

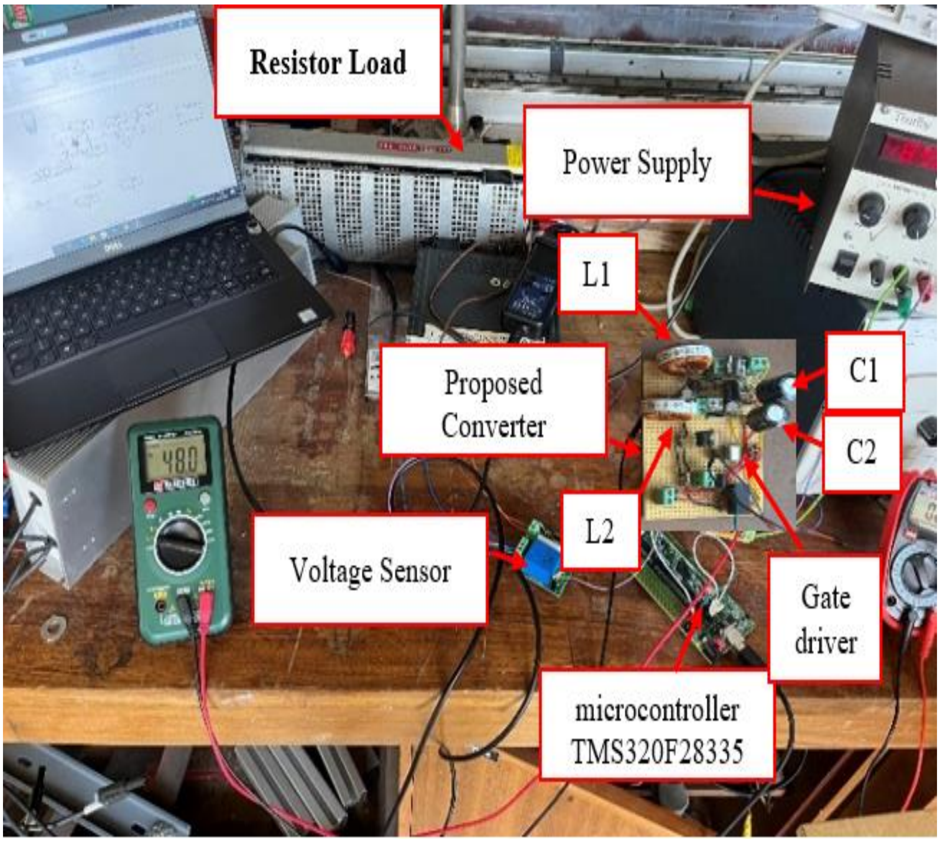

Fig 5.12 View of the experimental prototype of the hybrid DC-DC converter.

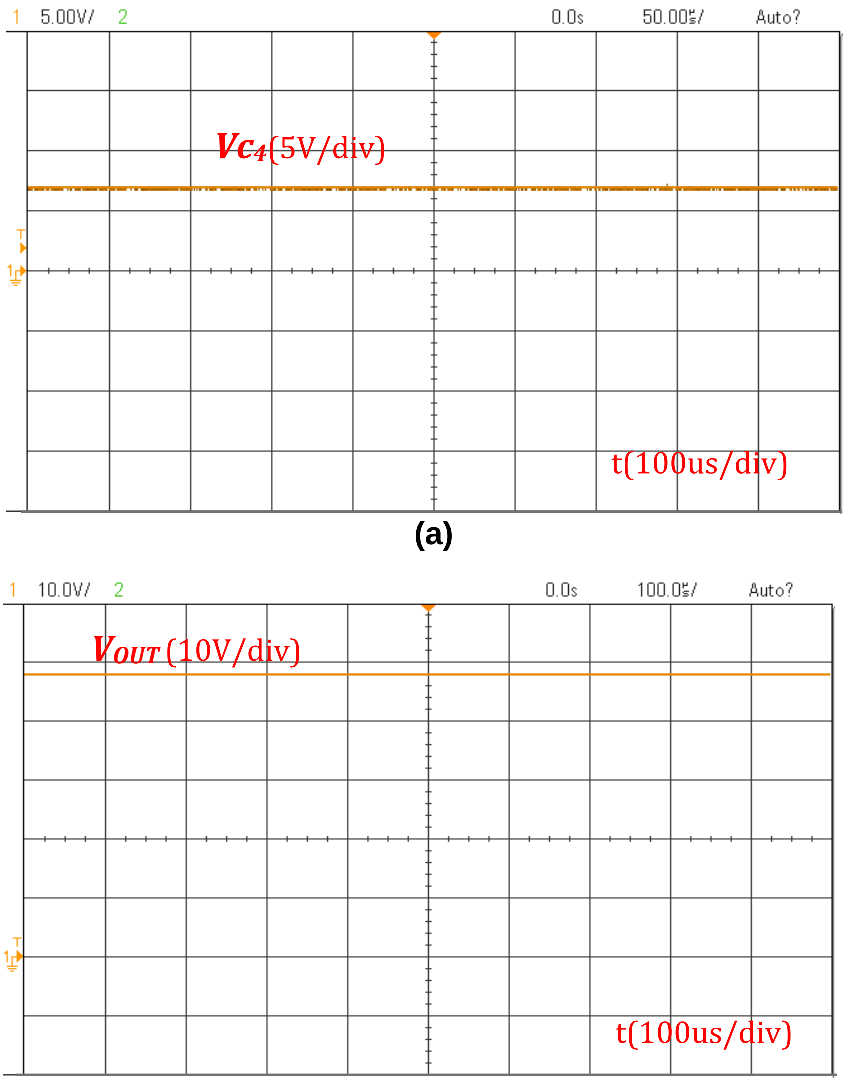

(a)

(b)

Fig 5.13 (a) Capacitor voltage V_{C4} and (b) output voltage.

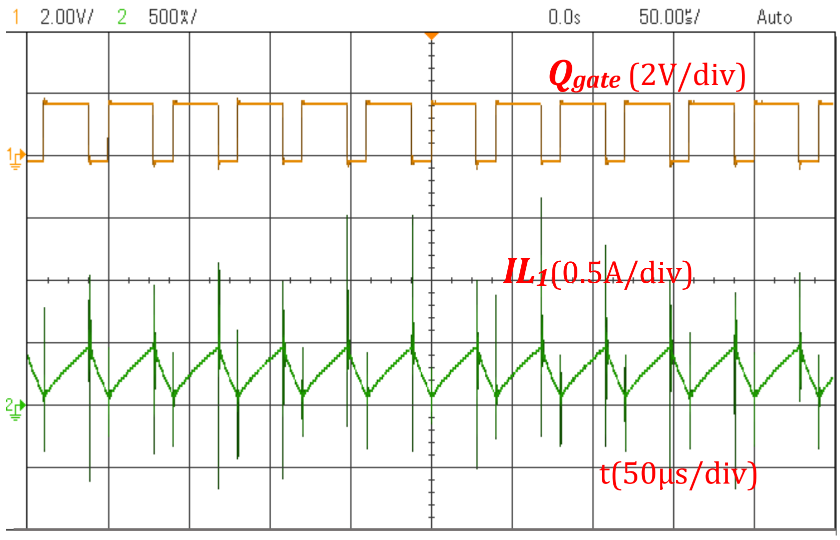

Fig 5.14 Currents were flowing through the inductors I_{L1} and gate drive signal.

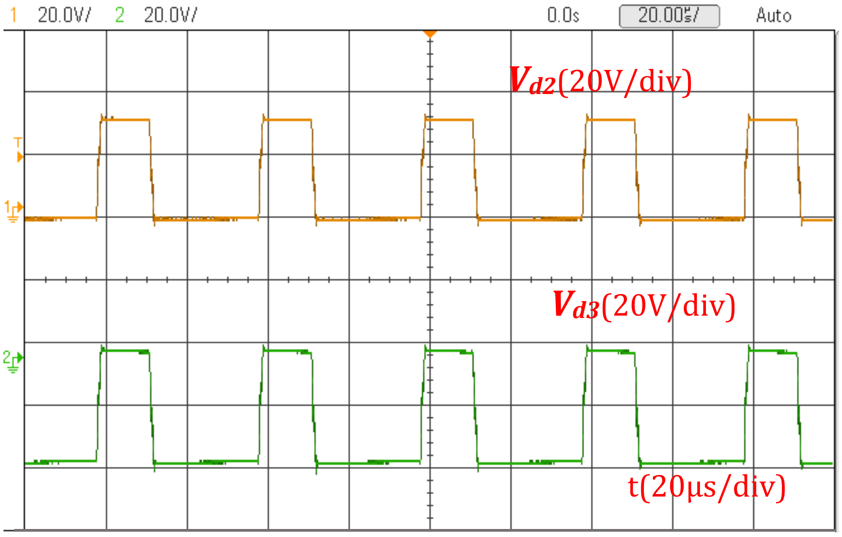

Fig 5.15 Voltage across the diode D2 and D3.

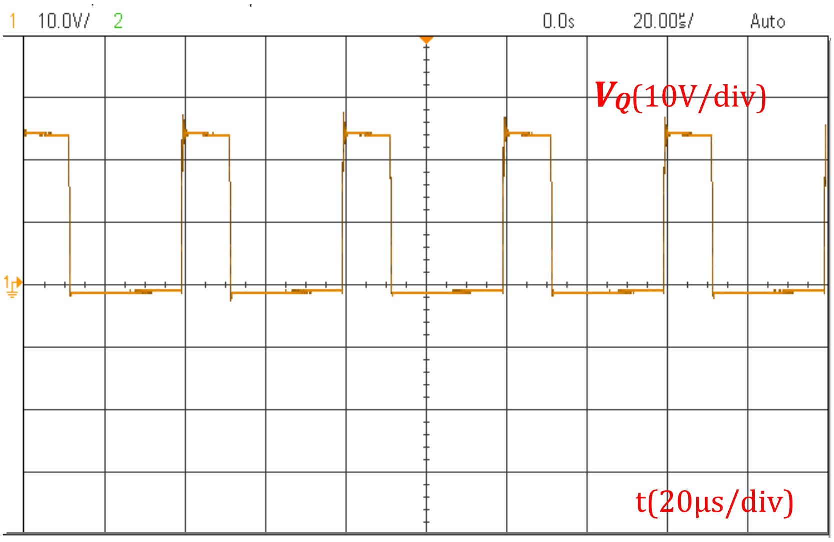

Fig 5.16 Voltage across the switch.

5.6 Experimental results

A low-power hardware prototype is implemented to evaluate the feasibility of the converter proposed. In the laboratory prototype, all the circuit parameters are the same as those used in the simulation, as described in Table 5.1. The experiments were conducted with an electrical source of constant voltage instead of a renewable energy source. Based on the table above, it is intended to have an input power source of 7V. In addition, the microcontroller TMS320F28335 has been included in the design to implement the control system. To demonstrate the test setup, the output voltage is set to 48 V. The experimental prototype is depicted in Fig.5.12. In this chapter, the results were all obtained with a duty cycle of less than 0.7, and the duty cycle was set at 0.7 to limit the semiconductor losses, giving a gain of 6.8, which was in line with the simulation results.

Based on Fig.5.13(a), the waveform shows that the output voltage is 48 V. On Fig.5.13(b) also shows the voltage across the capacitor C_4. Fig.5.14 shows the experimental waveforms of the currents flowing through the inductors i_{L1} and gate drive signal of switch Q. The inductor in this figure operates in the continuous conduction mode. As shown in Fig.5.15 and 5.16, experimental waveforms show the voltage across the switch and the diodes. Here is Fig.5.16, which shows the experimental waveforms of the voltages across the diodes D_2 and D_3. It also shows their complementary states of operation. Considering these last two figures, the voltage stress across the switch and diodes is half the maximum output voltage. The efficiency of the converter that is being presented is illustrated in Fig.5.17. The figure indicates that the converter's efficiency is not less than 93.9% even under the most unfavourable conditions when it is operating at 6 W.

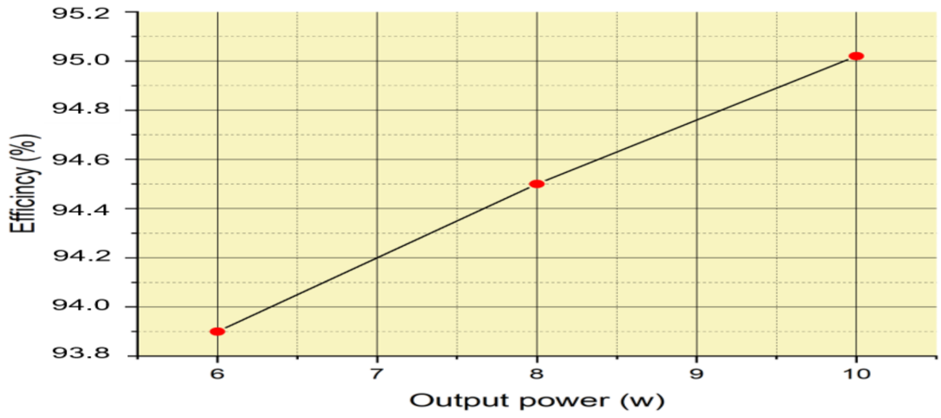

Fig 5.17 The efficiency of the presented converter for various output powers.

5.7 Performance Comparison

A comparison of the proposed converter's performance with other similar converters is presented in Table 5.3. Based on these results, the proposed converter provides a better voltage gain with only one active switch and less normalized voltage stress on the switch. According to the analysis and discussion presented, the proposed converter has the advantage of both functionality and efficiency.

Table 5.3 Performance comparison of similar converter topology

Similar Converter Topology	Converter [136]	Converter [137]	Converter [138]	Converter [139]	Converter [140]	Proposed Converter
Switches used	1	2	1	1	1	1
Diodes used	5	2	2	3	1	2
No. of Inductors used	3	2	2	3	2	2
No. of capacitors used	3	2	3	3	3	3
Continuous input current	Yes	No	Yes	Yes	No	Yes
Voltage gain, V_O	$\frac{(d)^2}{(1-d)^2}V_{in}$	$\frac{2(1+d)}{(1-d)}V_{in}$	$\frac{1}{(1-d)}V_{in}$	$\frac{d}{(1-d)^2}V_{in}$	$\frac{2d}{(1-d)}V_{in}$	$\frac{(1+d)}{(1-d)}V_{in}$
Efficiency	91%	90%	91%	90%	92%	92.2%
The voltage stress on the active switch	Moderate	Less	High	Less	High	Moderate

5.8 Extension into Bipolar Output Four-Port Converter

This section proposes synthesising a new Four-Port bipolar Converter that combines the outputs of a unipolar converter Luo and a unipolar converter Cuk as shown in Fig.5.18. An additional bidirectional power flow port, consisting of switches S_2, S_3, and diode D_3, is added to the previously proposed topology in this chapter to interface with the energy storage unit. The proposed converter integrates solar panels and batteries into the bipolar dc microgrid. The proposed converter consists of only three switches to generate PV power, charge, and discharge batteries, and deliver symmetrical bipolar voltage as the output voltage. In addition, the converter can convert power between sources and loads in a single stage, improving its efficiency. It is possible to guarantee higher reliability by sharing a reference ground between the PV input port, the battery port, the positive output port, and the negative output port. According to the relationships between PV generation power and load power, the Four-Port Converter provides an uninterrupted power supply to the DC load in three modes. The voltages of positive and negative polarities in the converter are symmetrical regardless of the mode in which it operates.

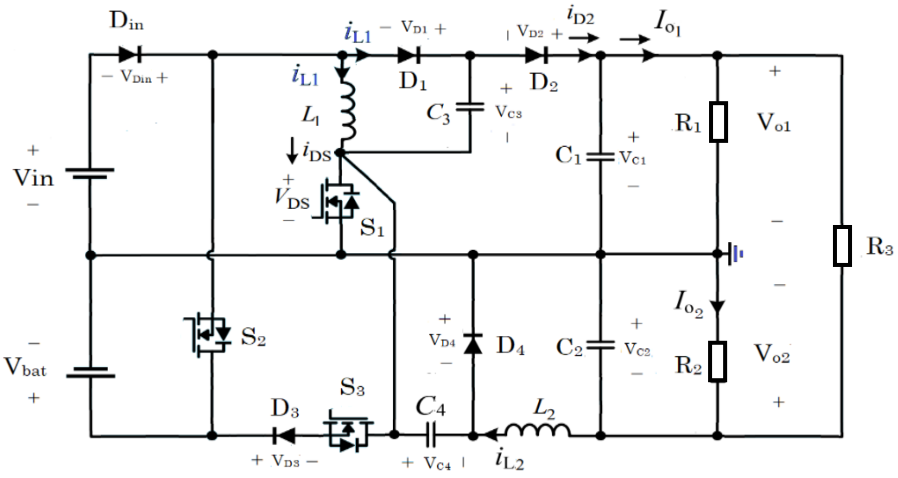

Fig 5.18 Non-isolated Symmetric Bipolar Output Four-Port converter.

5.9 Summary

This chapter proposes a combined Luo-Cuk converter topology appropriate for LED lighting and PV applications. The working principles and steady-state characteristics of the converter were discussed in detail. Two characteristics are present in the converter. One of the key features of the equipment is to allow the high voltage gain to be achieved for the converter through the Luo link and the Cuk link using the same input branch so that you can realise two types of outputs at the same time through a single switch. It should also be noted that aside from the extended voltage static gain, the stress on the diode and switch is also reduced. The laboratory prototype results, and a theoretical and simulation analysis have also been included. Besides integrating the DC-DC converter, the proposed topology synthesis method also applies to the design of a non-isolated symmetric bipolar output Four-Port Converter that interfaces the PV-battery system.

Chapter 6 A New Bidirectional High Step-Up Multi-Input Multi-Output DC-DC Converter for Renewable Energy Applications

6.1 Introduction

Integrating these sources into electric power grids has become significantly more prevalent with the development of renewable energy sources. Nevertheless, these sources often fail to meet the requirements of some applications due to the low output voltage they produce. As a result, an interface voltage converter should be used to increase the device's output voltage and control the output voltage [141]–[144]. Further, renewable energy sources have a wide range of output voltages that vary depending on the environmental conditions. This can be accomplished simply by using N Single Input Single Output Converters for N voltage levels so that these requirements can be met, as pictured in Fig.6.1(a), but the problem with this approach is that it is very expensive and inefficient due to the large number of components it requires [145],[146]. There is an increasing tendency to combine the different types of sources, thereby reducing the component count and the overall cost of the system. This requires Multi-Input (MI) DC-DC converters, which can combine various sources.

Further, it has been suggested that the use of Multi-Output (MO) DC-DC converters can also be used to provide the needed power to loads with different voltage levels [147],[148]. As a result, high step-up DC-DC converters with multiple inputs and outputs are becoming increasingly popular in applications, including hybrid electric vehicles, DC microgrid systems, renewable energy, and personal computers, which require energy flow and voltage regulation. Since it is possible to integrate multiple SISO converters into one unit, the MIMO converter, shown in Fig. 6.1(b), becomes the dominant option since it can reduce the number of components and overall cost due to its ability to combine multiple SISO converters into one unit.

In terms of the Multi-Port Converter MPC structure, it can be divided into two categories: isolating converters and non-isolating converters. In isolation MPCs, voltage levels are flexible, power levels are high, and switch modes are soft [41], [149],[150]. Compared to isolated converters, non-isolated converters, such as buck, boost, buck-boost converters, etc., have the advantage of being compact, more efficient, and with higher power density than isolated converters [151],[152]. The non-isolated converter seems more appropriate for low-voltage DC microgrid applications (particularly those with a 48V DC bus voltage) than the isolated converter.

This chapter presents a new non-isolated Four-Port DC-DC Converter suitable for various applications requiring harvesting renewable energy sources. The converter is characterised by bidirectional power flow, low input current ripple, and a reduced number of components. This new non-isolated Four-Port Converter is designed and derived based on the topology circuit proposed in Chapter 4 of this thesis. A diode D_4 and an active switch S_4 have been added to have one more output power port to the circuit. Voltage lift techniques have been used in the circuit. There is an increasing geometric progression in the output voltage of a converter that leads to high-gain outputs that produce low ripples and high-efficiency outputs. The voltage lift cell has been inserted into the topology of the four ports, which is mentioned in the literature review in section 2.2.3. A four-port topology based on a single voltage lift cell has fewer components and a simpler structure. Among the salient features of the proposed converter are the followings:

1) Four simple switches are used to implement input generation, battery charging and discharging, and two output voltages. As a result of the single-stage power conversion between the source and the load, the converter's efficiency is also greatly improved.

2) As a result of the relationship between input source power and load power, the converter can operate in two modes: Single-Input Three-Output (SITO) and Double-Input Double-Output (DIDO). This allows the converter to always provide an uninterrupted power supply to the load.

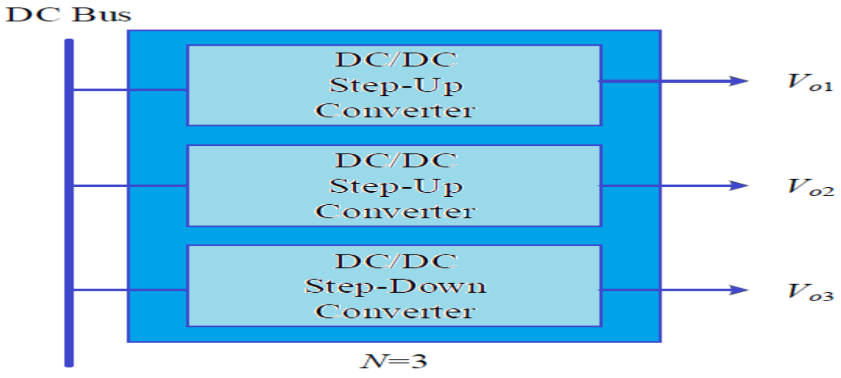

(a)

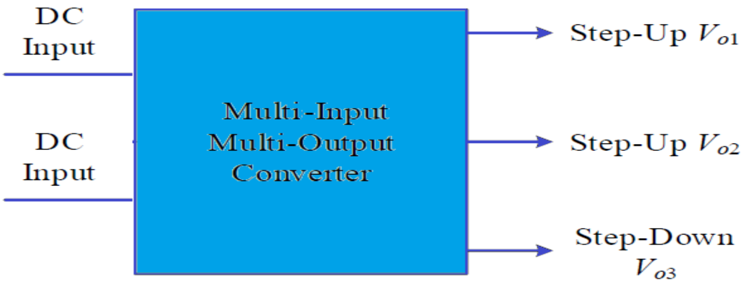

(b)

Fig 6.1 The schematic of converters with multiple outputs: (a) conventional (b) MIMO converter.

6.2 Proposed converter and operation modes.

An illustration of the power circuit of the proposed Four-Port DC-DC Converter is given in Fig.6.2. Following this figure, the source V_{in} is considered to be the energy source, and the source V_{bat} is considered as the energy storage (battery). According to the schematic, the proposed converter is composed of four switches (S_1 - S_4), three diodes (D_1, D_2, D_3, and D_4), two inductors (L_1 - L_2), and four capacitors (C_1, C_2, C_{o1}, and C_{o2}). The resistors R_1 and R_2 in this figure represent the equivalent power that can be fed to a multilevel inverter. As a result of the bidirectional power flow, the battery can be charged and discharged. When the battery is discharged, no gate pulse is given to the switches S_2 during the battery discharge process. It is, therefore, possible to control the discharging current of the battery and the output voltage by controlling switches S_1 and S_2. During charging, switch S_2 receives no gate pulse. The switches S_1, S_2, S_3, and S_4 will be controlled to deliver energy from the input source to the battery. An attempt should be made to minimise the ripple in the current drawn from the input sources. The converter operates in two main modes.

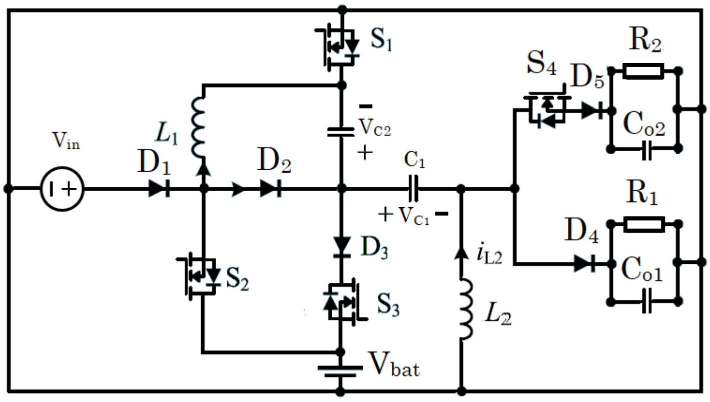

Fig 6.2 Structure of the presented Four-Port converter.

6.2.1 First operation mode (DIDO)

When this operation mode is enabled, two input power sources, V_{in} and V_{bat} (the battery), will supply the power to the loads. S_3 is completely OFF during this mode, and S_1, S_2, and S_4 are activated. Every switch is assigned a particular duty.

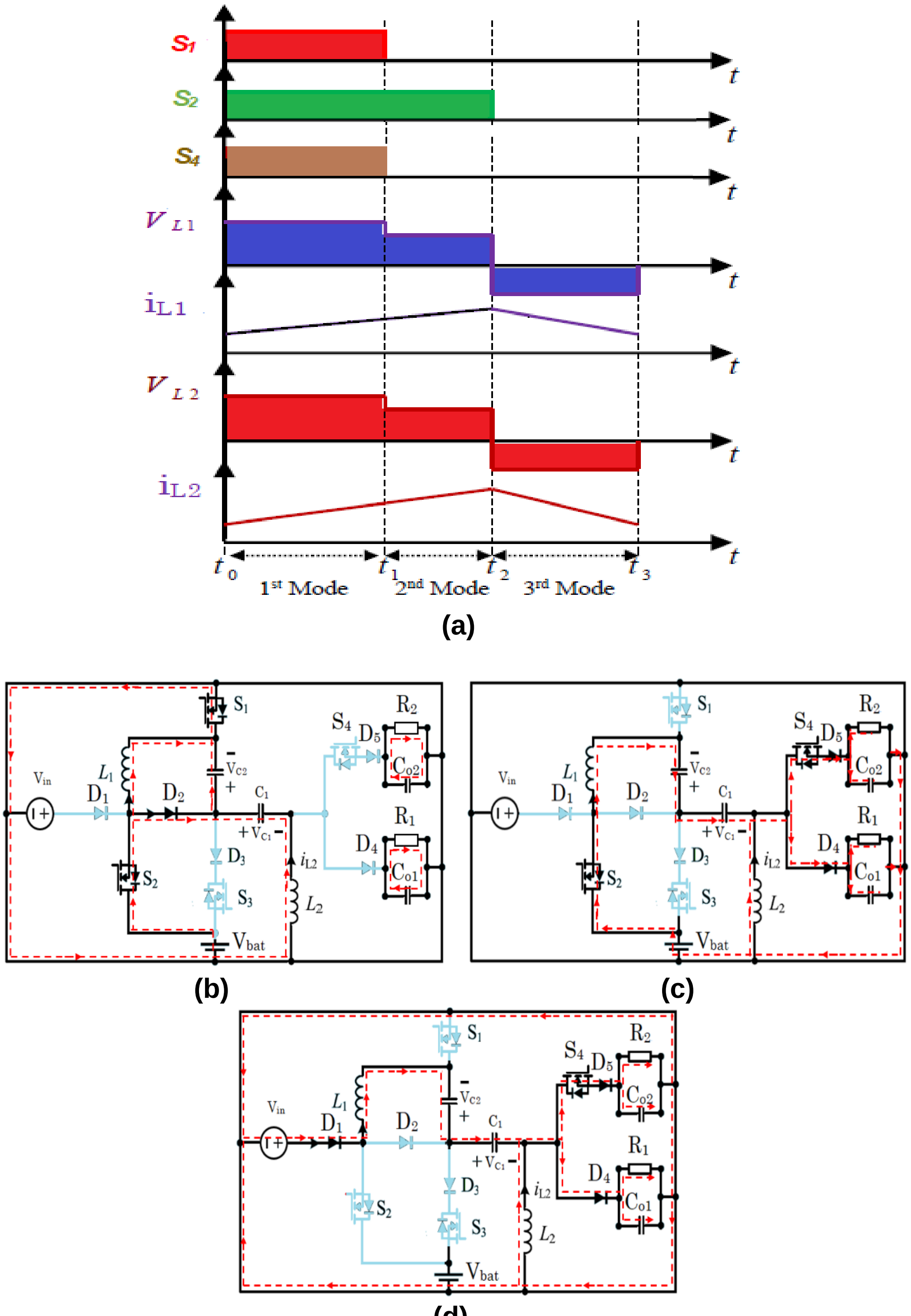

(a)

(b)

(c)

(d)

Fig 6.3 Current flow paths of the converter (a) Steady-state waveforms of the presented converter in the DIDO mode. Current flow paths of the presented converter in the DIDO mode, (b) Switching mode 1, (c) Switching mode 2, (d) Switching.

Controlling the inductor current, S_1 regulates the battery current to the desired value. As shown in Fig.6.3 (a), the gate signals of switches and the inductor's voltage and current waveforms. Depending on the state of the switches, there are three different modes of operation in one switching period as follows:

Switching State 1 ($t_0< t< t_1$): Switches S_1 and S_2 will be turned ON during this state. Since S_1 is turned ON, D_2 is forward-biased, and diodes D_4 and D_5 are reverse-biased. So, Switch S_4 has turned OFF. Because switch S_2 is ON, and $V_{in}<V_{bat}$ Diode D_1 is reverse-biased. As shown in Fig. 6.3(b), the equivalent circuit of the proposed converter at this state. Due to the charge created by V_{bat} on the inductor L_1, the inductor current increases at this state. Additionally, in this mode, the capacitors C_{o1} and C_{o2} are discharged, and the energy they hold is delivered to the load resistances R_1 and R_2, respectively.

Switching State 2 ($t_1< t< t_2$): At this point, switch S_2 is still turned ON, and switch S_1 has turned OFF. Diodes D_1 and D_2 is reverse-biased. In addition, switch S_4 has been turned ON. As shown in Fig.6.3(c), the equivalent circuit for the proposed converter in this state can be seen. At this point, inductor L_1 is discharged, transferring its stored energy to capacitors C_{o1}, C_{o2}, and load resistances R_1 and R_2. This mode also results in the charging of capacitors C_{o1} and C_{o2}.

Switching State 3 ($t_2< t< t_3$): This mode is characterised by the OFF state of all three switches. Therefore, the diodes D_1 and D_4 are forward-biased. The inductor L_1 is discharged at this point, and the stored energy is delivered to the capacitor C_{o1}, C_{o2}, and the load resistances R_1 and R_2. A charge is also applied to capacitors C_1 and C_2 in this mode. A schematic representation of the proposed converter in this state can be found in Fig.6.3(d).

6.2.2 Second operation mode (SITO)

This mode allows V_{in} to power both the V_{bat} battery and the loads.

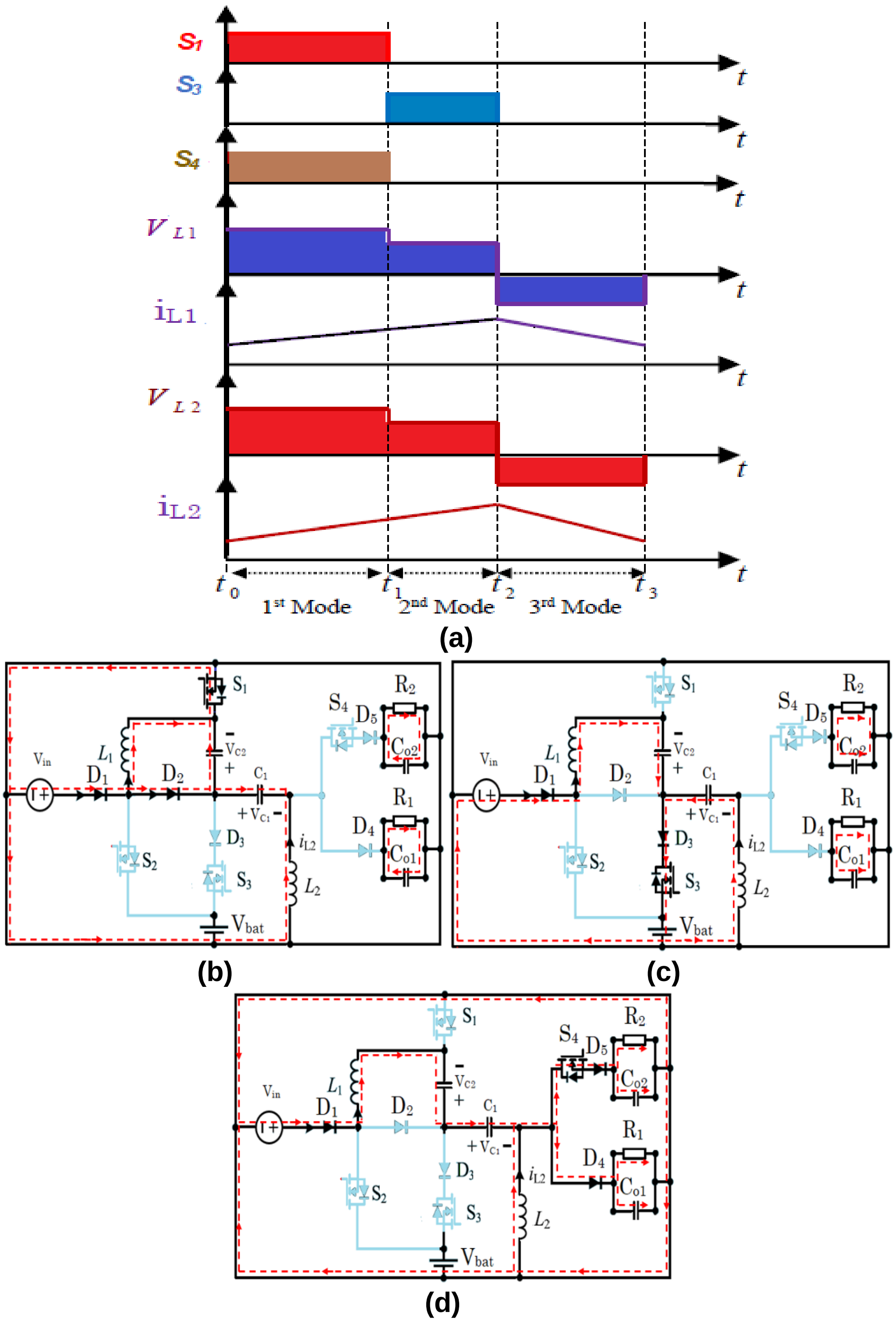

(a)

(b)

(c)

(d)

Fig 6.4 Current flow paths of the converter (a) Steady-state waveforms of the presented converter in the SITO mode. Current flow paths of the presented converter in the SITO mode, (b) Switching mode 1, (c) Switching mode 2, (d) Switching mode 3.

It occurs when the battery is depleted, and the load power is low. During this operation mode, switches S_1, S_3, and S_4 are all active, with switch S_2 completely OFF. Similarly, to the previous mode of operation of the converter in this mode, there is a particular duty that must be considered for each switch.

The total output voltage is regulated by switching S_1 to reach the desired value. A switch S_3 is responsible for regulating the battery charging current I_{bat} to maintain the desired level. A representative example of a gate signal of a switch can be seen in Fig.6.4(a), along with the voltage and current waveforms of an inductor.

Switching State 1* ($t_0 < t < t_1$)*: During this state, switches S_1 and D_2 are turned ON, so switches S_3 and S_4 are turned OFF. In addition, the diode D_4 doesn't conduct due to reverse bias. Here is a schematic representation of the equivalent circuit of the proposed converter shown in this state in Fig.6.4(b). As a result of V_{in} charging inductor L_1, there is an increase in current flowing through the inductor. This mode also involves the discharge of the capacitors C_{o1} and C_{o2} so that their stored energy can be delivered back to load resistances R_1 and R_2, respectively, in this mode.

Switching State 2 ($t_1 < t < t_2$): This mode of operation is accomplished by turning OFF switch S_1 and switch S_3 turned ON. The diode D_2 and D_4 are reversely biased. Therefore, diode S_4 is still completely inactive. A schematic representation of the equivalent circuit of the proposed converter in this state is shown in Fig.6.4(c). As $V_{in} = V_{bat}$, the inductor current decreases during this period, and the inductor releases its stored energy to the battery (V_{bat}). During this mode, the capacitors C_{o1} and C_{o2} will also be discharged to deliver their stored energy to the load resistances R_1 and R_2 simultaneously.

Switching State 3 **(t_2< t< t_3):** This mode maintains an OFF condition for switch S_1, turns OFF switch S_3, and turns ON switch S_4 and diode D_4. As well as this, diode D_2 is still reverse-biased. The equivalent circuit of the proposed converter is shown in Fig.6.4(d). As a result of this action, the inductor L at this point will be discharged, and the energy stored in the inductor will be transferred to the capacitors C_{o1} and C_{o2} and the load resistances R_1 and R_2, respectively. This mode of operation also applies a charge to both capacitors C_1 and C_2.

6.3 Control Structure method of proposed MIMO converter

6.3.1 Pole-placement control method

A converter's control system consists of two control loops, one for controlling the converter's output voltage and one for controlling the converter's input current. Decoupling the SISO transfer functions of the system is required for designing classical control compensators, like PI and PID. In the case of systems with more than three orders, the decoupling method becomes more complex. Therefore, MIMO systems control methods should be used to design converter closed-loop controllers. Among the control methods used in MIMO converters is the integral state feedback-based control method called pole placement, which is useful for designing a control system. Using this method, a closed-loop system can be designed with any pole location as desired, as long as the system is fully state-controlled and able to control its state at all times. An appropriate state feedback gain matrix is used to achieve this. The following is the definition of the controllability matrix:

$$\boldsymbol{\Psi_C} = [\boldsymbol{B} \ \vdots \boldsymbol{AB} \vdots \boldsymbol{A^2B} \vdots \boldsymbol{A^3B}] \tag{6.1}$$

If ΨC is a complete-rank matrix (rank (ΨC) = 4), it is at this point that the system becomes fully state-controlled. As a result, two additional integral states will now be considered:

$$\dot{q}_1(t) = r_1(t) - y_1 = r_1(t) - \tilde{\imath}_{L1}(t) \qquad (6.2)$$

$$\dot{q}_2(t) = r_2(t) - y_2 = r_2(t) - \tilde{v}_{o1}(t) \qquad (6.3)$$

Based on the new integral states, it is necessary to rewrite the state equations and output equations as follows:

$$\begin{bmatrix} \dot{\tilde{x}}(t) \\ \cdots \\ \dot{q}(t) \end{bmatrix} = \begin{bmatrix} A & \vdots & 0 \\ \cdots & \vdots & \cdots \\ -C & \vdots & 0 \end{bmatrix} \begin{bmatrix} \tilde{x}(t) \\ \cdots \\ q(t) \end{bmatrix} + \begin{bmatrix} B \\ \cdots \\ 0 \end{bmatrix} \tilde{u}(t) + \begin{bmatrix} 0 \\ \cdots \\ I \end{bmatrix} r(t) \qquad (6.4)$$

$$y(t) = \begin{bmatrix} C & \vdots & 0 \end{bmatrix} \begin{bmatrix} \tilde{x}(t) \\ \cdots \\ q(t) \end{bmatrix}$$

In (6.4), Defining the input reference vector ***r***(*t*), which can be shown in the following way:

$$r(t) = [I_{L1.ref} \quad V_{o1.ref}]^T \qquad (6.5)$$

Following the definition in (6.4), the new matrixes are the following:

$$\bar{A} = \begin{bmatrix} A & \vdots & 0 \\ \cdots & \vdots & \cdots \\ -C & \vdots & 0 \end{bmatrix}, \bar{B} = \begin{bmatrix} B \\ \cdots \\ 0 \end{bmatrix} \qquad (6.6)$$

It is possible to arrange the controllability matrix for the system in (6.4) ($\bar{\Psi}$C) in the following way:

$$\bar{\boldsymbol{\Psi}}_C = \begin{bmatrix} B & \vdots & A\Psi_C \\ \cdots & \vdots & \cdots \\ 0 & \vdots & -C\Psi_C \end{bmatrix} = \underbrace{\begin{bmatrix} B & \vdots & A \\ \cdots & \vdots & \cdots \\ 0 & \vdots & -C \end{bmatrix}}_{\mathbf{M}} \begin{bmatrix} I & \vdots & 0 \\ \cdots & \vdots & \cdots \\ 0 & \vdots & \Psi_C \end{bmatrix} \qquad (6.7)$$

If ΨC is considered complete-rank, the system defined in (6.4) is completely state-controllable if and only if the rank of the matrix ***M*** is 6. Therefore, there is matrix ***K***, which satisfies the following equation:

It can be stated that if matrix M has rank six, it becomes completely state-controllable if the rank of matrix C is considered a complete rank, which is where the system defined in (6.4) is. Matrix K, then, can be described as follows:

$$\tilde{u}(t) = -K\begin{bmatrix}\tilde{x}(t)\\ \cdots \\ q(t)\end{bmatrix} = -[K_X \;\; \vdots \;\; K_q]\begin{bmatrix}\tilde{x}(t)\\ \cdots \\ q(t)\end{bmatrix} \tag{6.8}$$

The following equation can be written by substituting (6.8 into 6.4):

$$\begin{bmatrix}\dot{\tilde{x}}(t)\\ \cdots \\ \dot{q}(t)\end{bmatrix} = \begin{bmatrix} A - BK_X & \vdots & -BK_q \\ \cdots & \vdots & \cdots \\ -C & \vdots & 0 \end{bmatrix}\begin{bmatrix}\tilde{x}(t)\\ \cdots \\ q(t)\end{bmatrix} + \begin{bmatrix}0\\ \cdots \\ I\end{bmatrix} r(t) \tag{6.9}$$

$$K_X = \begin{bmatrix} K_{11} & K_{12} & K_{13} & K_{14} \\ K_{21} & K_{22} & K_{23} & K_{24} \end{bmatrix} \tag{6.10}$$

$$K_q = \begin{bmatrix} \grave{K}_{11} & \grave{K}_{12} \\ \grave{K}_{21} & \grave{K}_{22} \end{bmatrix}$$

Table 6.1 The circuit specifications.

Parameter	Value	Parameter	Value
Output Voltage V_O	48V	Capacitor C_2	1μF/50V
Battery Voltage V_b	10~20V	Capacitor Co_1, Co_2	1000μF/60V
Input voltage V_{in}	12~24V	Inductors L_1 and L_2	300μH/12A
Input current I_{in}	0~1.2A	Switches S_1, S_2,S_3	Fdp2532
Switching frequency	25kHz	Diodes D_1, D_2, D_3	DSS16-01A
Capacitor C_1	100μF/50V	Controller	TMS320F28335

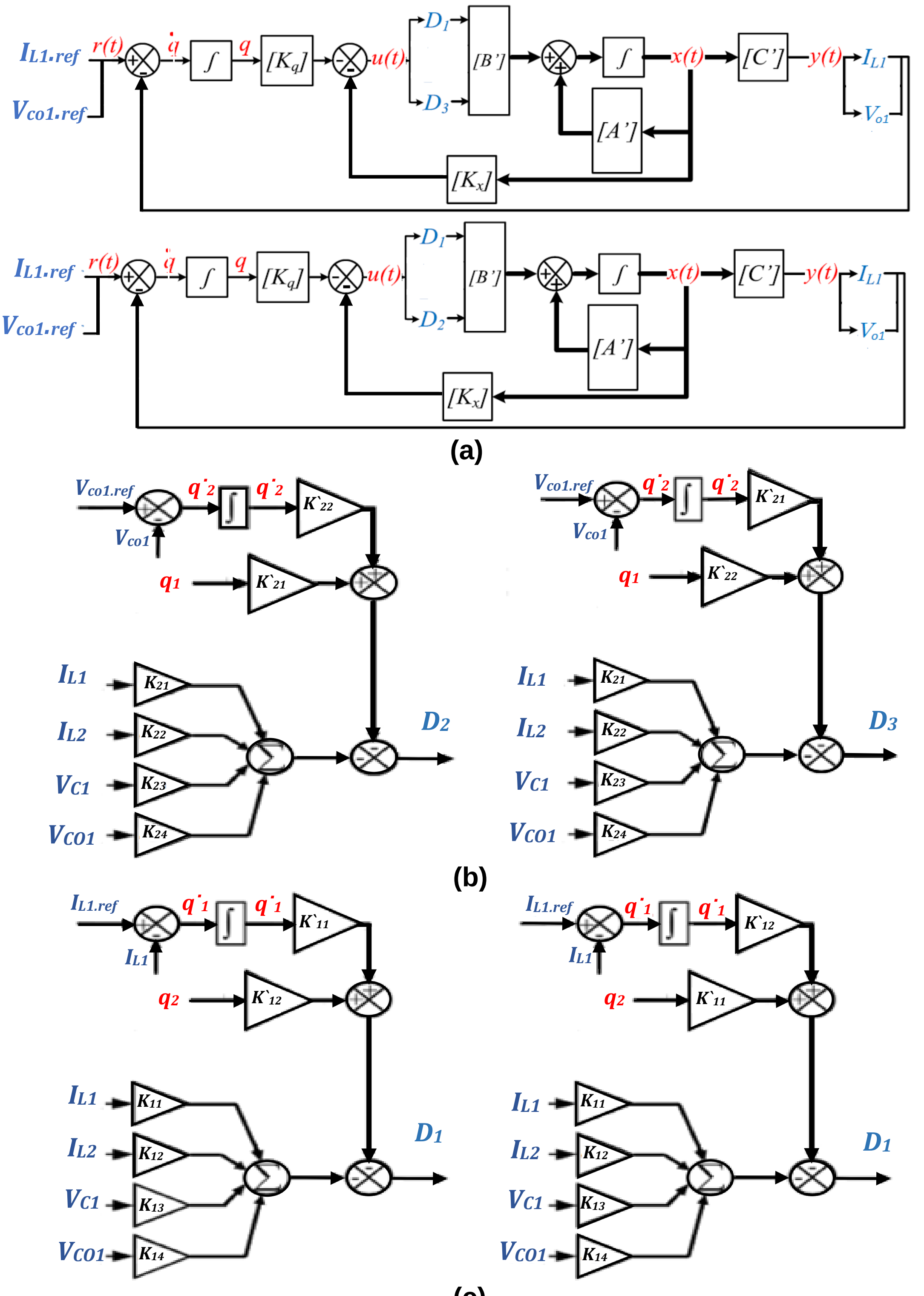

(a)

(b)

(c)

Fig 6.5 (a) Block diagram of the pole-placement control of the proposed converter, (b) voltage regulator loop of output, (c) current regulator loop of the input source.

Using the state feedback gain matrix K, it is necessary now to find the controlling signal (t) for the closed-loop system so that the closed-loop system eigenvalues are situated in the right place. The control systems toolbox provided by the MATLAB software contains a useful function for pole-positioning that takes input from the system (6.4) and the locations of the desired eigenvalues to find the state feedback gain matrices of the system. According to the block diagram of Fig. 6.5(a), the Pole-placement control method is shown in which the input the reference tracks current (i_{L1}) and the output voltage (V_{o1}) values i_{L1}, ref, and V_{o1}, ref, respectively, to balance the signals. A representation of two integral state feedback loops is shown in Fig.6.5 (b), (c) for the converter proposed.

6.4 Simulation Results

The converter can either have a Dual-Input-Dual-Output (DIDO) or Single-Input-Triple-Output Mode (SITO), which allows it to deliver uninterrupted power to a DC load in both modes. MATLAB / Simulink is used to simulate the process to carry out the steady state and transient analysis. Thus, controllers maintain a constant and regulated output voltage by adjusting the duty cycles of switches as the input voltage varies. As default DIDO mode has initiated, the state of charge is changed to decrease, as presented in Fig.6.6(a). In SITO mode, where a higher voltage input is applied to the converter, a transition occurs between two modes of operation. During this instance, the mode switching occurred because the input source increased to about 20V, as shown in Fig.6.6(b), leading to redundant power being used to charge the battery. It can be seen from Fig.6.6(c) that V_{o1} and V_{o2} are regulated.

On the other hand, as it can be seen from Fig.6.6(d), the state of charge of the battery increases when the switch from DIDO mode to SITO mode is initiated. As the load resistance changes, as illustrated in Fig.6.7(a), the controllers are also designed to regulate the output voltage based on these changes. The output voltage across both output ports does not subject to any significant changes with any change in load demands, and it remains around 48 V for both output ports with a negligible variation when the load changes, as it’s seen in Fig.6.7(b). Table 6.2 shows the analysis of output voltage waveforms V_{o1} and V_{o2}. These results demonstrate the validity of the control scheme in both varying input voltage and changing load demand situations.

Simulation results indicate that the proposed dynamic energy management method can maintain a constant bus voltage despite varying inputs or outputs and enable flexibility in switching between two modes.

Table 6.2 Analysis of output voltage waveforms of the proposed converter.

	Preshoot	**Overshoot**	**Undershoot**	**Rise Time**	**Settling Time**
V_{o1}	30.921%	0.224%	2.081%	41.577ms	72.264 ms
V_{o2}	29.221%	0.322%	2.056%	41.277ms	72.078 ms

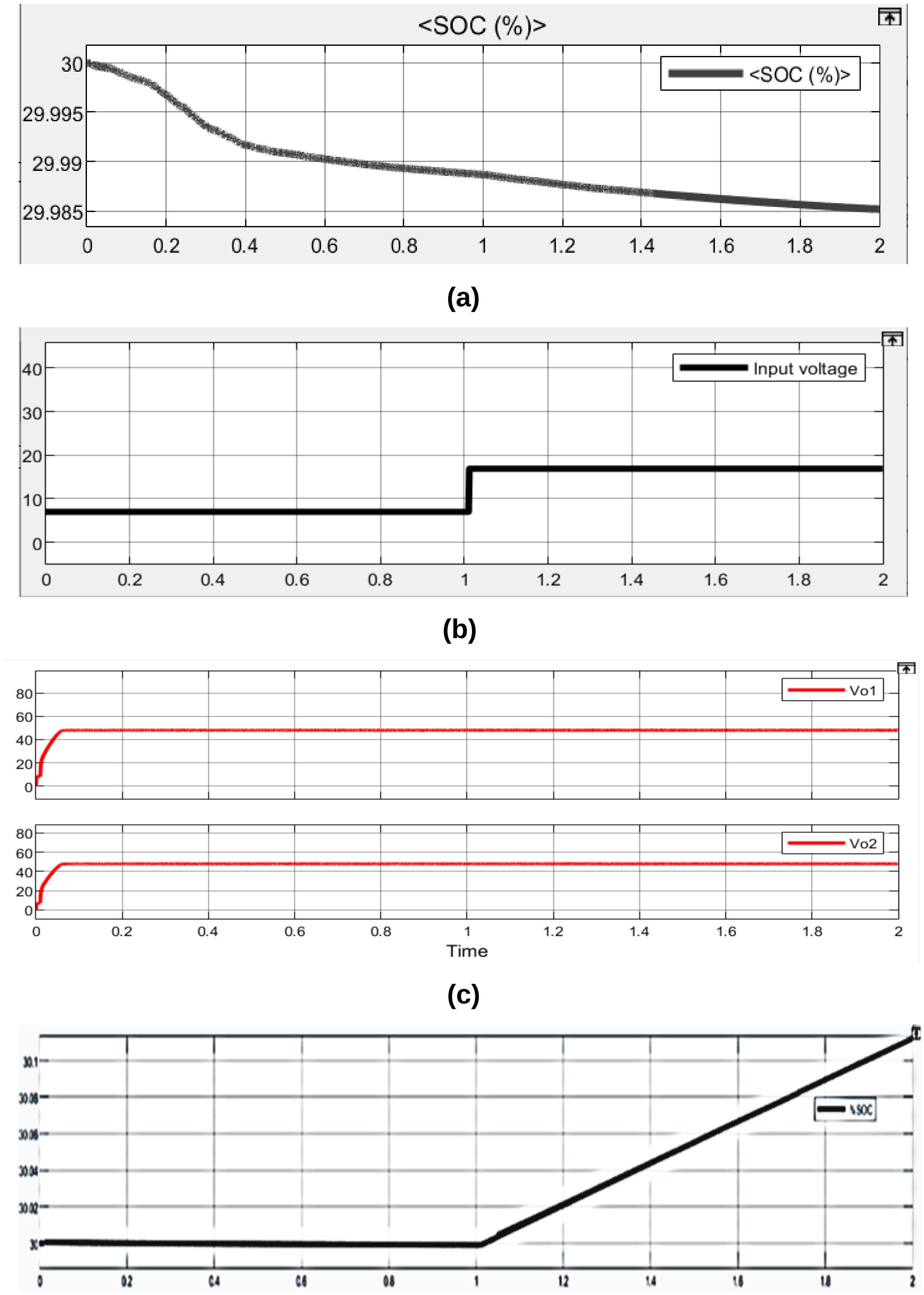

(a)

(b)

(c)

(d)

Fig 6.6 Close loop simulation results (a) state of charge in DIM, (b) input variation, (c) output voltage, (d) state of charge in TOM.

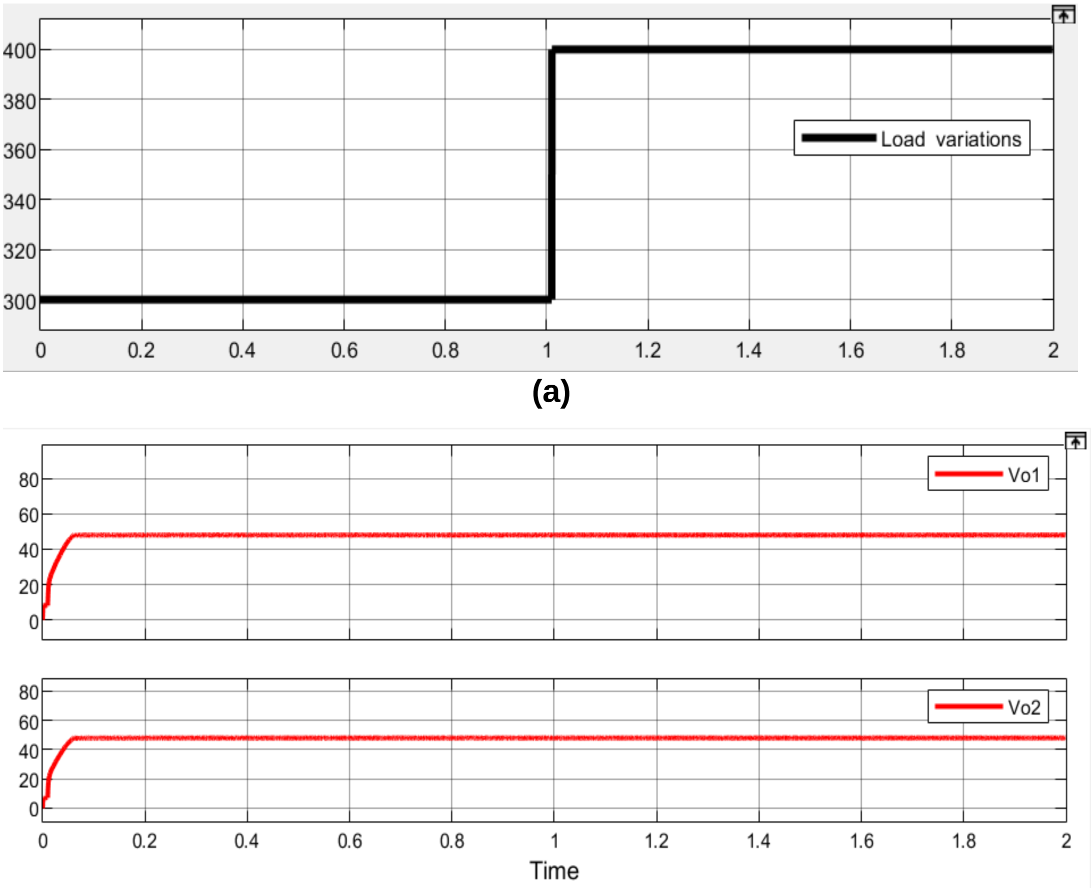

(a)

(b)

Fig 6.7 Close loop simulation results (a)load variation and (b) output voltage.

6.5 Extension into Multiple-Input Multiple-Output Converter

The proposed converter's structure is illustrated in Fig.6.8. According to the figure, the converter can be interfaced with another source of input power, V_{in1}. The converter proposed has only two inductors, (n+1) capacitors and (n+1) switches and diodes. The resistance R_1 and R_2 in the circuit represent the equivalent power feeding a multilevel inverter. Power flow can be controlled, and input voltage can be boosted by properly switching switches. This converter can be used to hybridised FC, batteries, and SC.

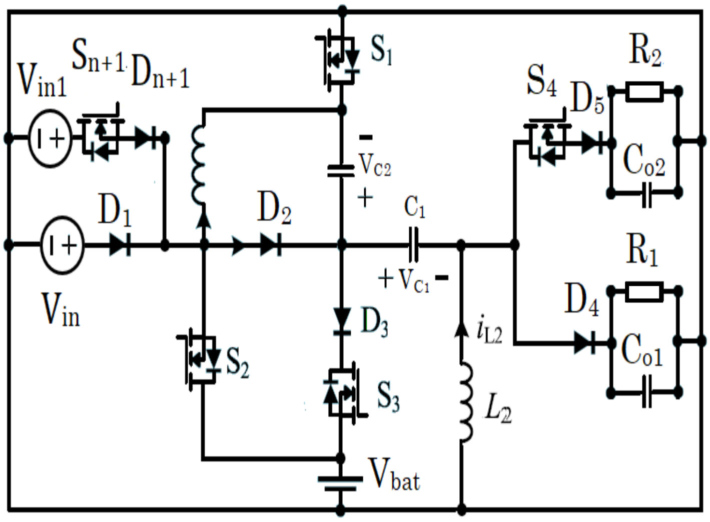

Fig 6.8 Extension of the proposed multi-port DC-DC converter.

6.6 Summary

A new DC-DC step-up converter with dual inputs and dual outputs was presented in this chapter. An electric vehicle or microgrid can be hybridised with multiple power sources employing this proposed converter topology with a unified structure. Additionally, the converter can be utilised as a converter with a single input and multiple outputs. It works in two main modes: battery discharging and charging. In different conditions for electric vehicles or microgrids, the converter can operate in different modes, such as buck and boost. A method of controlling the system, known as the pole-placement method, was developed. Additionally, the MATLAB simulation program is used to verify the various operating. Several input sources and multiple outputs can be added to the proposed topology that can be applied to various applications.

Chapter 7 Conclusions and Future Works

7.1 Conclusion

The techniques of increasing the voltage step-up conversion ratio have been studied, analysed, and applied in two converters, a high-step-up converter, and a Four-Port Converter, used to increase the voltage step-up conversion ratio. In addition, the newly developed two Three-Port Converters. The designed converters also achieve other advantages, such as a simple and cost-effective design, the ability to step up or down in voltage level, continuous input current, and energy being converted in one stage by flowing power bidirectionally between the two ports. For the converter design to improve its performance, three characteristics are highlighted as the most important ones:

- Step-up conversion ratios of high voltage are achieved without extremely high duty cycles of switches.
- The volume is relatively small.
- The component count is low.

Based on the findings of the study, the following conclusions can be drawn:

Chapter 3 introduces the Two-Input DC-DC Converter can be considered one of the best candidates for input source integration to maximise the use of renewable energy sources since it allows many of its components to be shared. The design has some features, including continuous input current, energy being converted in one stage by flowing power bidirectionally between the two ports, and the ability to step up or down in voltage level. In addition, it is possible to apply the converter to various applications, such as DMPPT PV applications, DC motor drive systems, and LED drivers. Experimental work has been conducted to verify topology. In the proposed converter, there are two switches and two diodes, which reduce switching losses, and have an overall component count of (8), making the design compact with a low volume. The maximum average efficiency achieved is 92.5%, whereas the minimum is 89.6%.

To optimise renewable energy sources, the ESS becomes an essential element, as it can resolve the intermittency issue and help manage the unpredictable changes in demand. One of the best possible candidates for an input source integration is a Three-Port Converter, as introduced in chapter 4. Since it allows some components to be shared, the proposed converter applies to many applications, such as satellite applications, DC motors, and LED drivers. A detailed discussion has been provided regarding the operation of the converter. By using either buck or boost modes, the optimal port voltage level can be selected based on the analysis of the converter presented. Furthermore, the SEPIC-based structure provides the TPC with the inherent protection of protecting itself against output short circuits due to the series capacitor, as well as reducing input current ripples. It is also advantageous that the converter has a simple and cost-effective design. There are three switches and two diodes in the proposed converter, thereby minimizing switching losses. Ten components are in total, making the converter compact and low volume. Experimental results have validated the proposed structure. The highest average efficiency is 92.5%, and the lowest is 90.9%. Besides integrating the DC-DC converter, the proposed topology synthesis method also applies to the design of non-isolated three-port converters that interfaces with the PV-battery system.

Chapter 5 introduces a non-isolated high step-up converter with only one switch. It is designed by integrating the Luo and Cuk topologies. This topology is intended for light-emitting diode lighting and PV applications. Compared to the current popular DC-DC converters, the proposed model has a high voltage step-up conversion ratio. Experimental work has been conducted to verify the design of the proposed non-isolated Luo-Cuk converter. All obtained results have a duty cycle of less than 0.7 and a gain of 6.8 times higher than classical converters, which was in line with the simulation results. In addition, stress across the switch and diodes is smaller than the output voltage, approximately 50% of the obtained output voltage. With a low-duty cycle, the semiconductor losses were limited. As a result, the highest average efficiency reaches 95%, and the lowest at 93.9%. In addition to integrating the DC-DC converter, the proposed topology synthesis method is also applicable to designing a non-isolated symmetric bipolar output four-port converter to interface with the PV-battery system.

Designed and simulated results for a Four-Port Converter are presented in chapter 6. This topology is proposed for microgrids and electric vehicles with battery backups. Low component counts are characteristic of the topology. Based on the analysis of the converter presented, the optimal port voltage level can be determined by using either buck or boost modes. It is also advantageous that the converter has a cost-effective design and continuous current at the input. Through simulation, the operation of the circuit and the control system of this converter has been verified. The proposed control structure achieves a regulated output voltage. However, the Four-Port Converter can be extended to include an additional input and output port.

7.2 Future Work

- Even though the proposed three-port converter can be extended to include n input and n output ports in addition to the bidirectional battery port as mentioned in chapters 3 and 4. A proper inverter can be incorporated into the proposed Three-Port-Converter TPC and the proposed Luo-Cuk converter to enable plug-and-play PV applications.
- Simulated results are used to verify the operating characteristics of Four-Port Converter since the experiment conditions are limited. Their experiments can therefore be conducted in the future.
- Current state-of-the-art topologies employ capacitor charge transference or magnetic elements for high step-up applications. Another popular method is integrating capacitive and magnetic means. New topologies with improved efficiency may result from further research on gain extension cells.
- Deriving topologies that can be applied to various applications can be studied further. Two classic topologies can be combined using the topology synthesis method by sharing inputs such as Boost, Buck, Zeta, and Sepic.
- The coupled inductor can be added to the Luo-Cuk topology to make the system more suitable for relatively high-power applications. As a possible extension, the proposed converter includes an additional battery bidirectional port, and symmetric two-bipolar output ports, as mentioned in chapter 5.

Appendix A

Simulink Model of the Proposed Converters

A.1 Introduction

This section presents the closed-loop MATLAB/Simulink model used in simulating the behaviour of the proposed converters (Two Input Converter, Three-Port Converter, high step-up DC-DC Converter, and Four-Port Converter).

A.2 Two-Input Converter Simulink Model

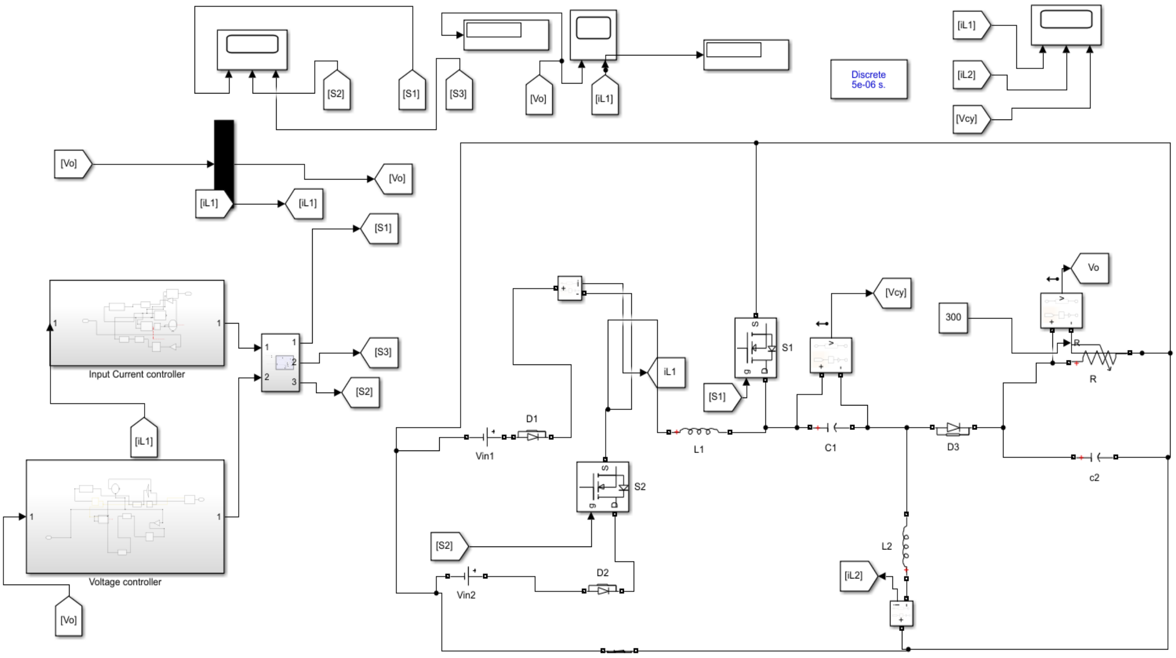

Fig A.1 Simulink model of the Two-Input Converter.

Fig.A.1 shows the MATLAB\Simulink model of the proposed Two-Input converter. It comprises two dc sources, V_{in1} and V_{in2}, and two primary switches, S₁, S₂, and C₁ coupling capacitors, C₂ is the filter capacitor, and *R* is the resistive load. In this circuit, the two inductors.

A.3 Three-Port Converter Simulink Model

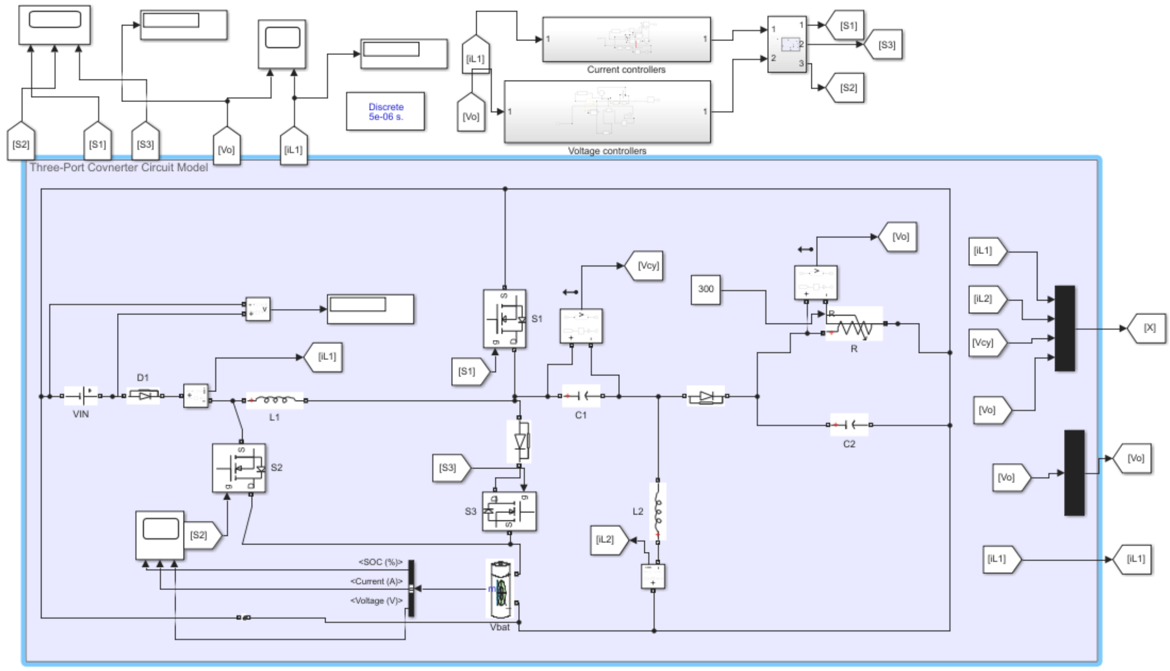

Fig A.2 Simulink model of the Three-Port Converter.

Fig.A.2 illustrates the MATLAB\Simulink model of the proposed Three-Port Converter. The only difference in the circuits is the substitution of switch S_2 with a bidirectional cell to integrate the battery.

A.4 High Set-Up Converter Simulink Model

Fig.A.3 shows the MATLAB/Simulink structure of the proposed combined high step-up converter. The converter employs two inductors (L_1 and L_2). It comprises C_1, C_2, the filter capacitors C_3 and C_4 coupling capacitors, and three diodes, D_1, D_2, D_3, and *R* is the resistive load.

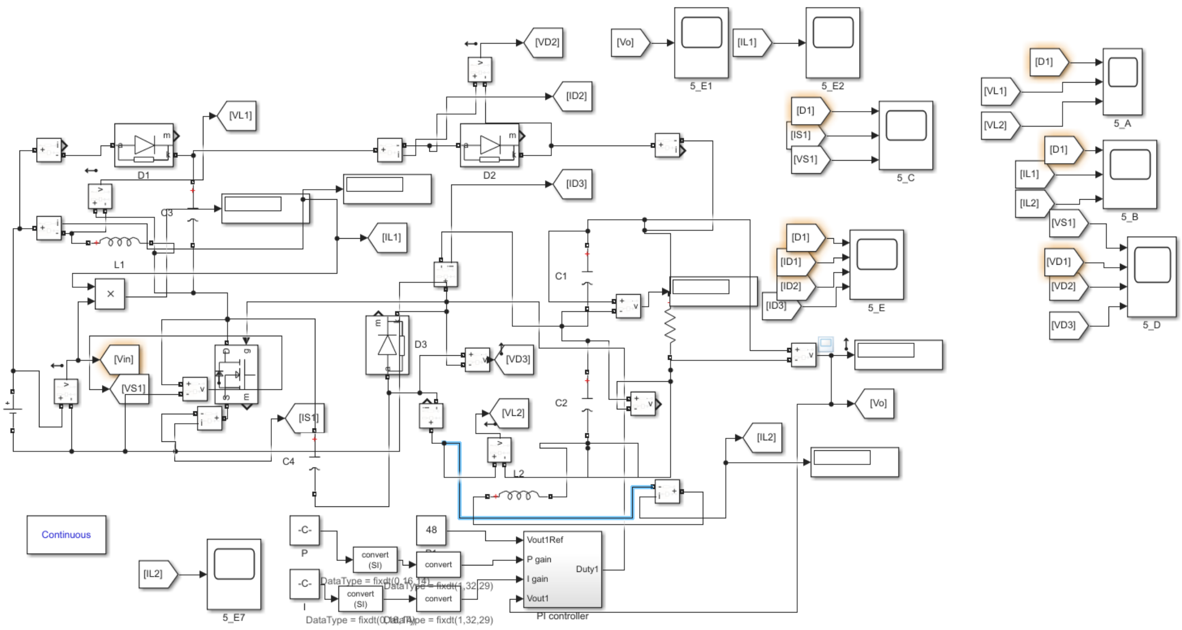

Fig A.3 High Set-Up Converter Simulink Model.

A.5 Four-Port Converter Simulink Model

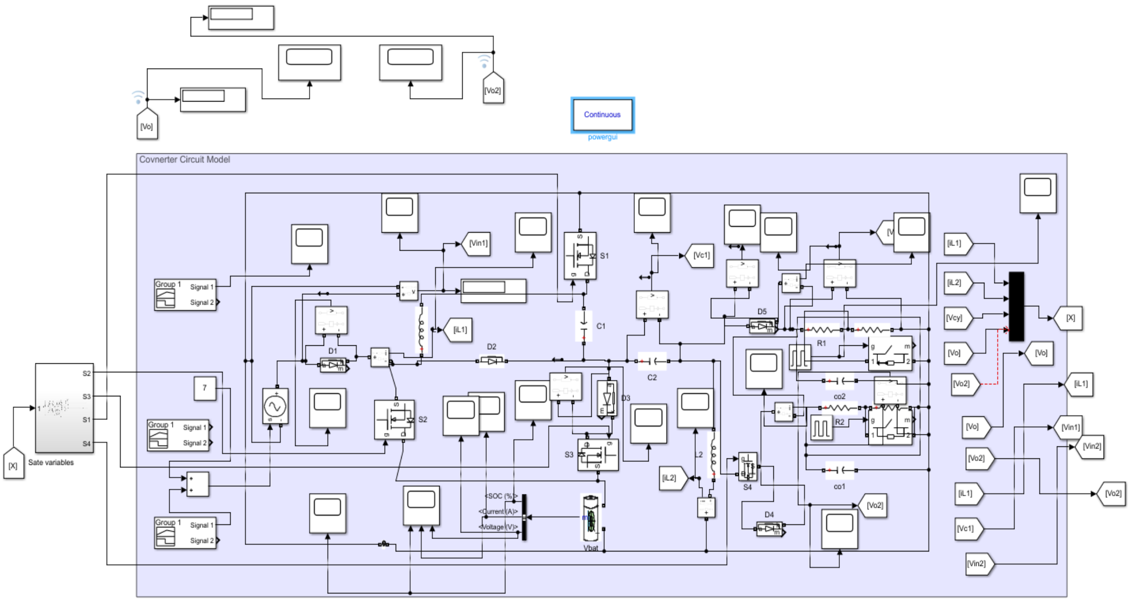

Fig A.4 Four-Port Converter Simulink Model.

Fig.A.4 illustrates the MATLAB\Simulink model of the proposed Four-Port Converter. The only difference in the circuits is adding extra switches S_4 and D_4 to integrate the second output port.

A.6 Pole Placement Control MATLAB code

```
clear
clc
%  close all
D1=0.51;
D3=0.74;
L1=300e-6;
L2=300e-6;
Cy=100e-6;
Co=1000e-6;
R=300;
Vbat=36;
Vcy=20;
Vco=48;
iL1=1.3;
iL2=-0.9;

% I=(Vco/R*1-D1-D3)/(D1+D3)

% Steady state model of mode SIDO

A=[0 0 (D3+D1-1)/L1 (D3+D1-1)/L1;0 0 (D3+D1)/L2 (D3+D1-1)/L2;(1-D1-D3)/Cy –(D1-D3)/Cy 0 0;(1-D1-D3)/Co (1-D1-D3)/Co 0 -1/R/Co];
B=[(Vcy+Vco)/L1 (Vcy+Vco-Vbat)/L1;(Vcy+Vco)/L2 (Vcy+Vco-Vbat)/L2;-(iL1-iL2)/Cy –(iL1-iL2)/Cy;-(iL1-iL2)/Co –(iL1-iL2)/Co];
C=[1 0 0 0;0 0 0 0];
D = [0 0; 0 0];

%% The system has two modes (SIDO & DISO) both have two input, two output
% % % % % % % % % % % % % % % % % % % % % % % % % % % % % % % % % % % % % % %
% %  define state matrix
% state-space model of the first mode(SIDO)

% A=[0 0 -178 178;0 0 550 -500;-128 128 0 0; 0 -1 0 0.0000666];
%
% B=[8 0;48 -96;-0.014 2.56; 0 0];
%
% C=[1 0 0 0;0 0 0 1];
%
% D = [0 0; 0 0];
% % create a state-space object of SIDO
% %
% [num1 den1] = ss2tf(A,B,C,D,1)  % iu = 1
% [num2 den2] = ss2tf(A,B,C,D,2)  % iu = 2
%
%
%  sys = ss(A,B,C,D);

%   tf(sys)
% bode(sys)
% % % % % % % % % % % % % % % % % % % % % % % % % % % % % % % % % % % % % % %
% state-space model of second mode(DISO)
%  A1=[0 0 -178 178;0 0 550 450;1 -1 0 0; 0 -1 0 0.0001];
%
% B1=[8 8;48 0;-0.014 2.5; 0 0];
%
% C1=[1 0 0 0;0 0 0 1];
%
% D1 = [0 0; 0 0];

 D11=0.6;
  D21=0.33;
 L11=300e-6;
 L21=300e-6;
 Cy=100e-6;
 Co=1000e-6;
 R1=200;
 Vbat=36;
Vcy1=10;
Vco1=48;
```

```
iL11=1.2;
iL21=-0.9;
% % Steady state model of model DISO
A1=[0  0  (D11-1)/L11  (D11-1)/L11;0  0  D11/L21  (D11-1)/L21;(1-D11)/Cy  -D11/Cy  0  0;(1-D11)/Co  (1-D11)/Co  0  -
1/R1/Co];
B1=[(Vcy1+Vco1)/L1 Vbat/L1;(Vcy1+Vco1)/L2 0;-(iL11-iL21)/Cy 0;-(iL11-iL21)/Cy 0];
C1=[1 0 0 0;0 0 0 1];
D1a = [0 0; 0 0];
% %

% % create the state-space object of DISO
% [num11 den11] = ss2tf(A1,B1,C1,D1,1)  % iu = 1
% [num22 den22] = ss2tf(A1,B1,C1,D1,2)  % iu = 2
% sys1 = ss(A1,B1,C1,D1);



%% TF


% %  tf(sys1)
% % % % % % % % % % % % % % % % % % % % % % % % % % % % % % % % % % % % % % % % % % % % % %
% % %
% Check open loop eigenvalues for both modes
% % % % % % % % % % % % % % % % % % % % % % % % % % % % % % % % % % % % % % % % % % % % %
%  poles = eig(A)
%   poles = eig(A1)
% % % % % % % % % % % % % % % % % % % % % % % % % % % % % % % % % % % % % % % % % % % % % %
% % %
% Check the rank of both modes
% % % % % % % % % % % % % % % % % % % % % % % % % % % % % % % % % % % % % % % % % % % % %
% rank(ctrb(A,B))
%  rank(ctrb(A1,B1))

% % % % % % % % % % % % % % % % % % % % % % % % % % % % % % % % % % % % % % % % % % % % % %
% % %
% % Full state feedback control without integral action
% % % % % % % % % % % % % % % % % % % % % % % % % % % % % % % % % % % % % % % % % % % % %
%  pL =[-7000+15500i;-7000-15500i;-200+15000i;-200-15000i];
%  pL =[-200+5500i;-200-5500i;-7500+1000i;-7500-1000i];
% desired close loop 132eigenvalues of SIDO mode

% pL =[-50+150i;-50-150i;-100+200i;-100-200i];
%  pL =[-50+1400i;-50-1400i;-200+4800i;-200-4800i];il only
% pL =[-5500+10i;-5500-10i;-9000;-10200]
%  pL =[-50+400i;-50-400i;-100+1300i;-100-1300i];il only
%  pL =[-5000+100i;-5000-100i;-9000;-10200];VO only
% pL =[-4099;-10000;-49990;-50000];
% pL =[-300+287i;-300-287i;-35000+22487i;-35000-22487i];
%  pL =[-5000;-18907;-27888;-29400];
% pL =[-1473+100*1i -1473-100*1i -14999+9010*1i -14999-9010*1i];
% pL =[-880+i*600;-880-i*600;-2500+i*6000;-2500-i*6000];
% pL =[-10500+7487i;-10500-7487i;-7699;-7700];0000
% pL =[-12000;-20000;-7977;-7989];
% pL =[-26000;-35000;-49977;-49089];
% pL =[-410+i*1580;-410-i*1580;-2000+i*1710;-2000-i*1710];
% pL =[-310+i*1580;-310-i*1580;-2000+i*1710;-2000-i*1710];
% pL =[-210+i*1180;-210-i*1180;-2000+i*1710;-2000-i*1710];
%  pL =[-210+i*480;-210-i*480;-2000+i*1710;-2000-i*1710];
%   pL =[-250+i*170;-250-i*170;-2700+i*1700; -2700-i*1700];
%   pL =[-12+i*40;-12-i*40;-200+i*20;-200-i*20];
%   pL =[-300+1000i*1;-300-1000i*1;-70+5000i*1;-70-5000i*1];
%  pL =[-100+500i*1;-100-500i*1;-500+5000i*1;-500-5000i*1];
%   pL =[-4+0.25i*2; -4-0.25i*2;-30; -150];
  % desired close loop 132 eigenvalues of DISO mode
%   pL1 =[-2; -50;-90; -120];
%  pL1 =[-6000+1000i;-6000-1000i;-25000+1250i;-25000-1250i];%IL/D2
%  pL1 =[-6000+400i;-6000-400i;-25000+1250i;-25000-1250i];
%  pL1 =[-6000+100i;-6000-100i;-10000+500i;-10000-500i];
%  pL1 =[-1700+1000i;-1700-1000i;-20000+5000i;-20000-5000i];
%  pL1 =[-1700+1000i;-1700-1000i;-20000+5000i;-20000-5000i];          %il/d1
% %  pL1 =[-6000+100i;-6000-100i;-7000+500i;-7000-500i];
% % pL1 =[-5000+100i;-5000-100i;-6000+500i;-6000-500i];
% % pL1 =[-3000+100i;-3000-100i;-4000+100i;-4000-100i];
 pL1 =[-3000+100i;-3000-100i;-3700+50i;-3700-50i];
```

```
% %  pL1 =[-1700+1000i;-1700-1000i;-20000+15000i;-20000-15000i];
% %  pL1 =[-1700+1000i;-1700-1000i;-21500+14999i;-21500-14999i];
% %   pL1 =[-29+10i;-29-10i;-1033;-5000];
% %    pL1 =[-10+2.25i*1; -10-2.25i*1;-5; -10];
% %    pL1 =[-1+1.25i*1; -1-1.25i*1;-2; -3];
% %   To find the state feedback gain K using pole placement of SIDO mode
% %  K= place(A,B,pL);
% % %   To find the state feedback gain  K1 using pole placement of DISO mode
% %
 K1= place(A1,B1,pL1);
% % % create a closed loop for SIDO
% %   sys_SIDO = ss(A-B*K,B,C,0);
% %
% %    tf(sys_SIDO);
%
   sys_DISO = ss(A1-B1*K1,B1,C1,0);

  tf(sys_DISO)

%
% % create a closed loop for DISO
% %  sys_cl1 = ss(A1-B1*K1,B1,C1,0);
% %
%  poles = eig(sys_DISO)
% %  bode(sys_cl(1,2)),grid on
% % bode(sys_cl(2,1)),grid on
%
%
% %
%
% % display plots of SIDO MODE
%
% % % ///////////////////////////////////////////////
% %   [Gm,Pm] = margin(sys_cl(1,1))
% %   [Gm,Pm] = margin(sys_cl(1,2))
% % % [Gm,Pm] = margin(sys_cl(2,2))
% h1 = subplot(211);
% margin(sys_DISO(2,1));
% hold on;
% h2 = subplot(212);
% margin(sys_DISO(2,2));
% hold on;


% h2 = subplot(212);
% margin(sys_cl(2,2));
%  hold on;
% % %
%  allmargin(sys_cl(1,1))
%  allmargin(sys_cl(1,2))
%   allmargin(sys_cl(2,2))

% 133igenva(sys_cl(1,1))
%
% bode(sys_cl(1,1),sys_cl(2,2));
%  legend('iL1','Vo');
%
% step(sys_cl)
% *///////////////////////////////////////



% display plots of DISO MODE

% ///////////////////////////////////////////////
% [Gm,Pm] = margin(sys_cl1(1,2))
% [Gm,Pm] = margin(sys_cl1(2,1))
%  h1 = subplot(211);
%  margin(sys_cl1(1,1));
%  hold on;
% %
%  h2 = subplot(212);
% margin(sys_cl1(2,2));
%  hold on;
%
```

```
%  allmargin(sys_cl1(1,1))
%   allmargin(sys_cl1(2,2))

% bode(sys_cl(1,1),sys_cl(2,2));
%  legend('iL1','Vo');
%
% step(sys_cl1)
% *//////////////////////////////////////
% bode(sys_cl),grid


% h1 = subplot(211);
% bode(sys_cl(1,1));
% hold on;
% h2 = subplot(1,2);
% bode(sys_cl(2,2,1,1));
% hold on;
%
% %
% % h1 = subplot(211);
% % bode(sys_cl(1,1));
% % hold on;
% % % h2 = subplot(212);
% % bode(sys_cl(2,2));
% % hold on;
% % set(gcf,'currentaxes',h1);
% legend('iL1','Vo');


% check for closed loop 134 eigenvalues of SIDO mode

% poles = eig(sys_cl)

% check for closed loop 134 eigenvalues of DISO mode


% poles = eig(sys_cl1);


% check step response for SIDO
% step(sys_cl)

% check step response for DISO
% step(sys_cl1)


% % % % % % % % % % % % % % % % % % % % % % % % % % % % % % % % % % % % % % % % % % % % % %
% % %
% % Full state feedback control with integral action
% % % % % % % % % % % % % % % % % % % % % % % % % % % % % % % % % % % % % % % % % % % % %

% % Add integrals of iL1 & Vo to the model for steady-state control and generate augmented plant of SIDO mode.
%
% Aa1=[A zeros(4,1);-C zeros(1,4))]
% Ba1=[B;zeros(1)];
%  Ca= [C zeros(1)] ;
%   Da=0;
% %
% Aa1 = [[A,[0 0 0 0]];[-C, 0]];
% Ba1 = [B;[0 0]];
% Ca1 = [C,0];
% Da1 = 0;
 %%%%%%%%%%%%%%%%%%%%%%%%%%%%%%%%%%%%%%%%%%%%%
% Add poles for SIDO MODE
% % % % % % % % % % % % % % % % % % % % % % % % % % % % % % % % % % % % % %
% Here we have six poles
%  p1=-50+150i;
%  p2=-50-150i;
%  p3=-100+200i;
%   p4=-100-200i;
%   p5 =-50;
%  p6 =-25;
%   Ki= place(Aa1,Ba1,[p1,p2,p3,p4,p5])

%   M=Ki(1:2,1:4)
```

```
%    M1=Ki(1:1)
%    M2=Ki(3:3)
%   M3=Ki(5:5)
%    M4=Ki(7:7)
% %    Z=Ki(1:2,5:5)
%   M5=Ki(2:2)
%    M6=Ki(4:4)
%    M7=Ki(6:6)
%   M8=Ki(8:8)
%     Z1=Ki(9)
%     Z2=Ki(10)
% %    Z3=Ki(10)
% %    Z4=Ki(12)


%  sys_c= ss(Aa1-Ba1*Ki,Ca1,Da1)
%    sys_1=(Aa1-Ba1*Ki);
% % %
%  sys_c=ss(sys_1,Ba1,Ca1,Da1)
%
%    tf(sys_c)

%   [Gm,Pm] = margin(sys_c(1,1))
% [Gm,Pm] = margin(sys_c(2,2))
% h1 = subplot(211);
% margin(sys_c(1,1));
% hold on;
%
% h2 = subplot(212);
% margin(sys_c(2,2));

% %  Add integrals of iL1 & Vo to the model for steady-state control and generate augmented plant of DISO mode.

Aa11=[A1 zeros(4,2);-C1 zeros(2)];
Ba11=[B1;zeros(2)];
 Ca1= [C1 zeros(2)] ;
  Da1 =0;


 %%%%%%%%%%%%%%%%%%%%%%%%%%%%%%%%%%%%%%%%%%%%%%%%
% Add poles for DISO MODE
% % % % % % % % % % % % % % % % % % % % % % % % % % % % % % % % % % % % % %
% Here we have six poles
% Aa11=[A1 zeros(4,2);-C1 zeros(2)];
% Ba11=[B1;zeros(2)];
%  Ca1= [C1 zeros(2)] ;
%   Da1 =0;
%
%
  p11=-3000+100i;
  p21=-3000-100i;
 p31=-4000+100i;
 p41=-4000-100i;
%  p51 =-98;
%  P61=-101;
p51 =-4508;
 P61=-5251;
% %
% %
% %
% %
  Ki1 = place(Aa11,Ba11,[p11,p21,p31,p41,p51,P61]);
%
% % % % %
%    F1=Ki1(1:2,1:4)
% % % % %
%   H1=Ki1(1:2,5:6)
% %
% Nbar=-inv(C1*inv(A1-B1*K1)*B1)
%  sys_1_1=(Aa11-Ba11*Ki1);
% %
% sys_c1_1=ss(sys_1_1,Ba11,Ca1,Da1)
% % % %
%  step(sys_c1_1)
% %   F=Ki(1:2,1:4);
```

```
% %   g1=Ki1(1:1);
% %    g2=Ki1(2:2);
% %    g3=Ki1(3:3);
% %    g4=Ki1(4:4);
   H=Ki1(1:2,5:6)
%
g1=Ki1(1:1);
 g2=Ki1(3:3);
  g3=Ki1(5:5);
   g4=Ki1(7:7);
  g5=Ki1(2:2);
   g6=Ki1(4:4);
   g7=Ki1(6:6);
  g8=Ki1(8:8);
    H1=Ki1(9);
    H2=Ki1(11);
   H4=Ki1(12);
% %     H1=Ki1(1:1,5:6)
%     H2=Ki1(2:2,5:6)

% %
%  sim(‘MY_DC_20.slx’)
%  sim(‘MY_DC21.slx’)
% %  open_system(‘DISO_20.slx’)
% %  sim(‘DISO_20.slx’)
%  open_system(‘SIDO.slx’)
%   sim(‘SIDO.slx’)
% % % % % % % % % % % % % % % % % % % % % % % % % % % % %
% % Check bode plot of both modes

%  bode(sys_cl),grid
%    bode(sys_cl1),grid
%         step(sys_cl1)
%  bode(sys_c)
% step(sys_c)
% % % % % % % % % % % % % % % % % % % % % % % % % % % % % % % % % % % % % % %
%
%  A11=[-3.847 2.98 -512.9 201;-2.28 -30.78 67.53 4.008;-0.08267 -0.3195 -79.38 30.54; 0 -1 0 0.0001];


%
% B11=[8 8;48 0;-0.014 2.5; 0 0];
%
% C11=[1 0 0 0;0 0 0 1];
%
% D11 = [0 0; 0 0];
%
%  [num111 den111] = ss2tf(A11,B11,C11,D11,1) ; % iu = 1
 %[num222 den222] = ss2tf(A11,B11,C11,D11,2);  % iu = 2
% %
% %
% %
%  sys = ss(A,B,C,D);
%   tf(sys_c)
```

Appendix B
Proposed Converters Hardware

B.1 Introduction

This appendix details the power electronics hardware used in testing Three Proposed converters (Two-input, Three-Port, and High set-up converter) in this thesis.

B.2 Two-Input Converter Circuit

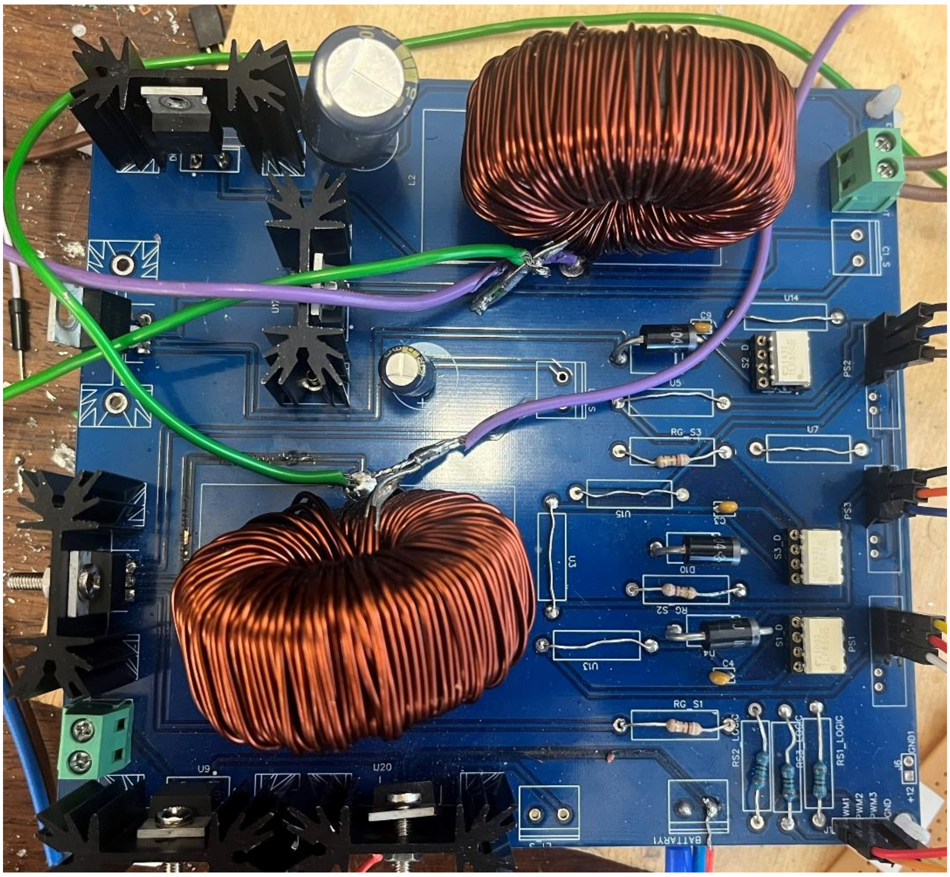

Fig B.1 Complete Two-Input Converter prototype.

Fig.B.1 shows the photograph of the Two-Input converter. The converter has been designed and built to test the performance. The converter consists of two inductors, two switches, a coupling capacitor, and an output capacitor.

B.3 Three-Port Converter Circuit

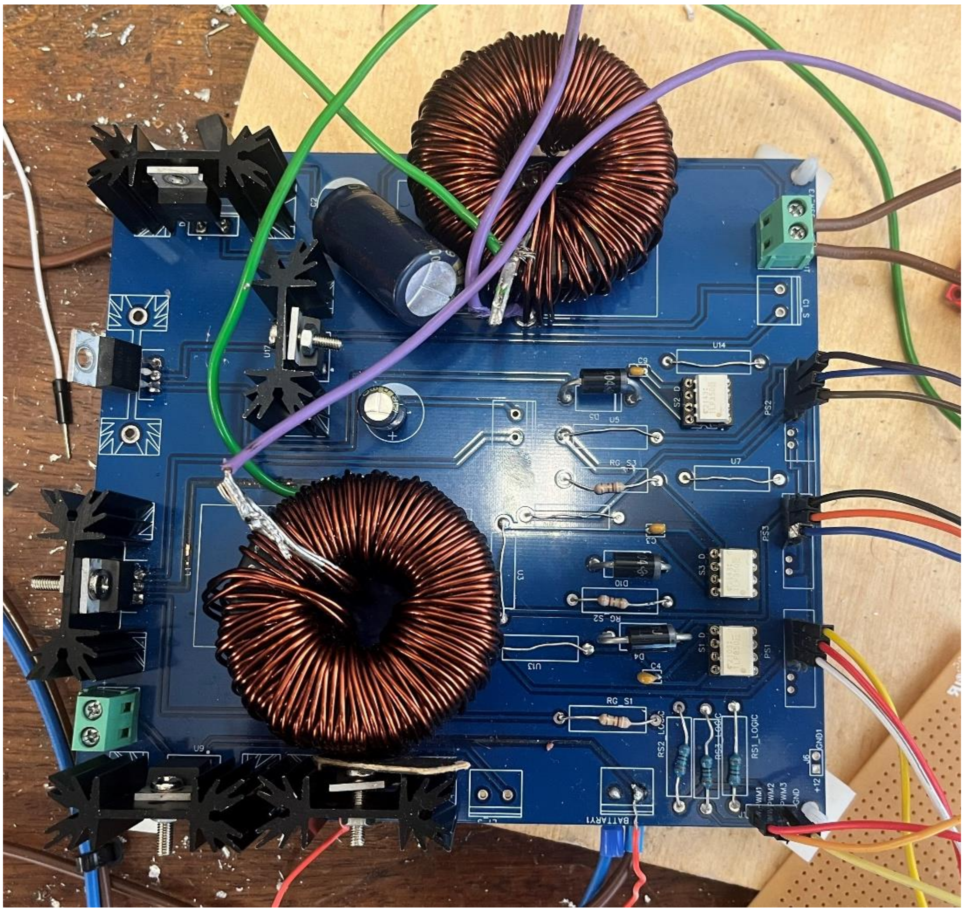

Fig B.2 Complete Three-Port Converter prototype.

Fig.B.2 shows the photograph of the Three-Port converter. The converter has been designed and built to test the performance. The converter consists of two inductors, three switches, a coupling capacitor, and an output capacitor. As can be seen from Fig.B.1 and Fig.B.2, both prototypes are the same. The only difference is the third switch is added with a diode to integrate the battery for bidirectional flow.

B.4 High Set-Up Converter Circuit

An interleaved converter has been constructed in order to test the concept. The converter is populated on the stripboard Fig.B.3. The converter consists of two inductors, one switch, two coupling capacitors, three diodes, and two output capacitors.

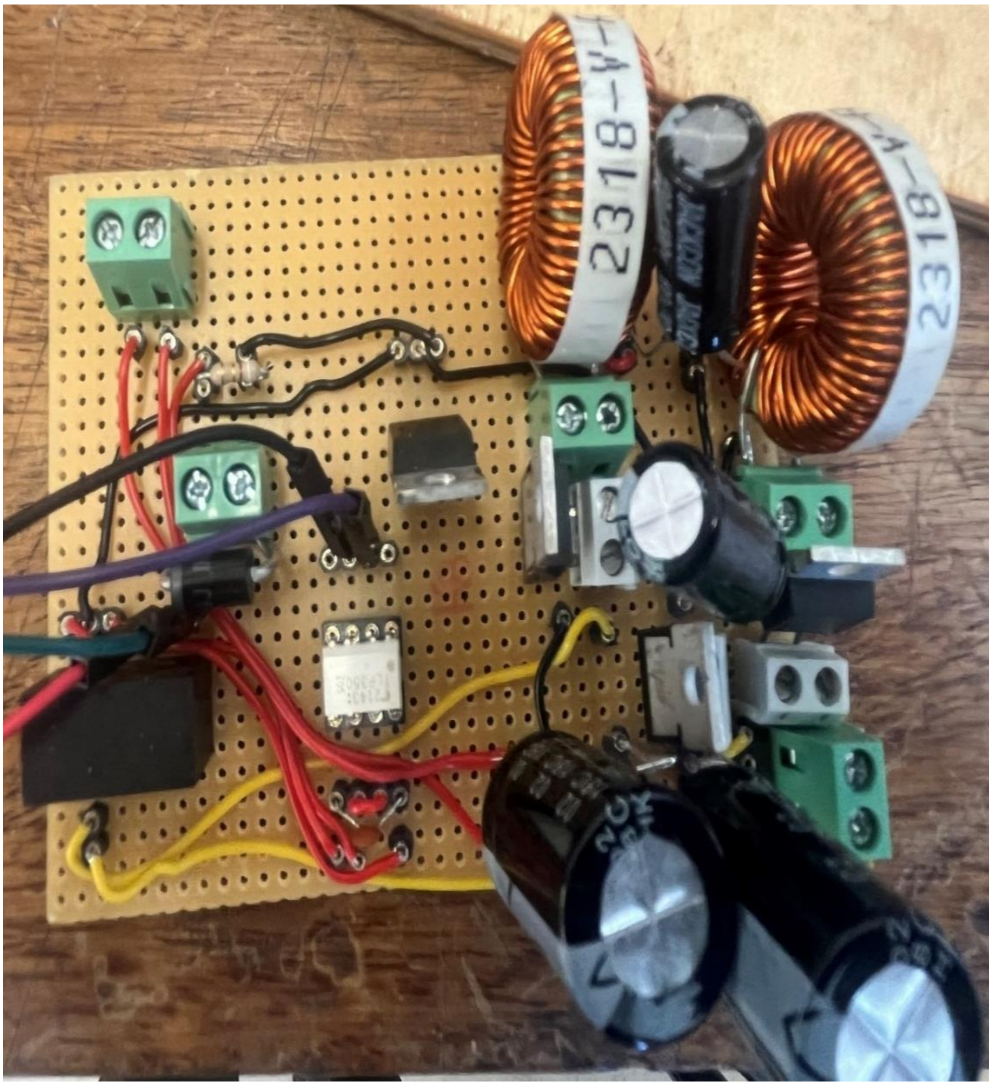

Fig B.3 Complete high-set-up converter prototype.

Appendix C
Controller Overview

C.1 Introduction

This appendix provides a comprehensive description of the control hardware popularly known as the Digital Signal Processor (DSP) board. The board is used in all the research work carried out in this thesis.

C.2 Digital Signal Processor (DSP) Board

A power electronics converter traditionally requires PWM signals to operate. The converters are typically controlled by DSP based on electronics/semiconductor chips. This controller is Texas Instrument ® TMS320F28335 (DSC) [133]. The DSP board consists of many parts, such as an analogue to digital converter (ADC) module with 16 input channels PWM peripheral comprising six pairs of (ePWM) modules [134]. The card has four communication ports that can be configured to allow data transfer between the code composer studio (CCS) environment from the host computer to the target via the JTAG interface [135]. Detail information and specifications of the TMS320F28335 DSP board can be found in [136]. Fig.C.1 shows the TMS320F28335 DSP card, and a block diagram of the converter control architecture is shown in Fig.C.2.

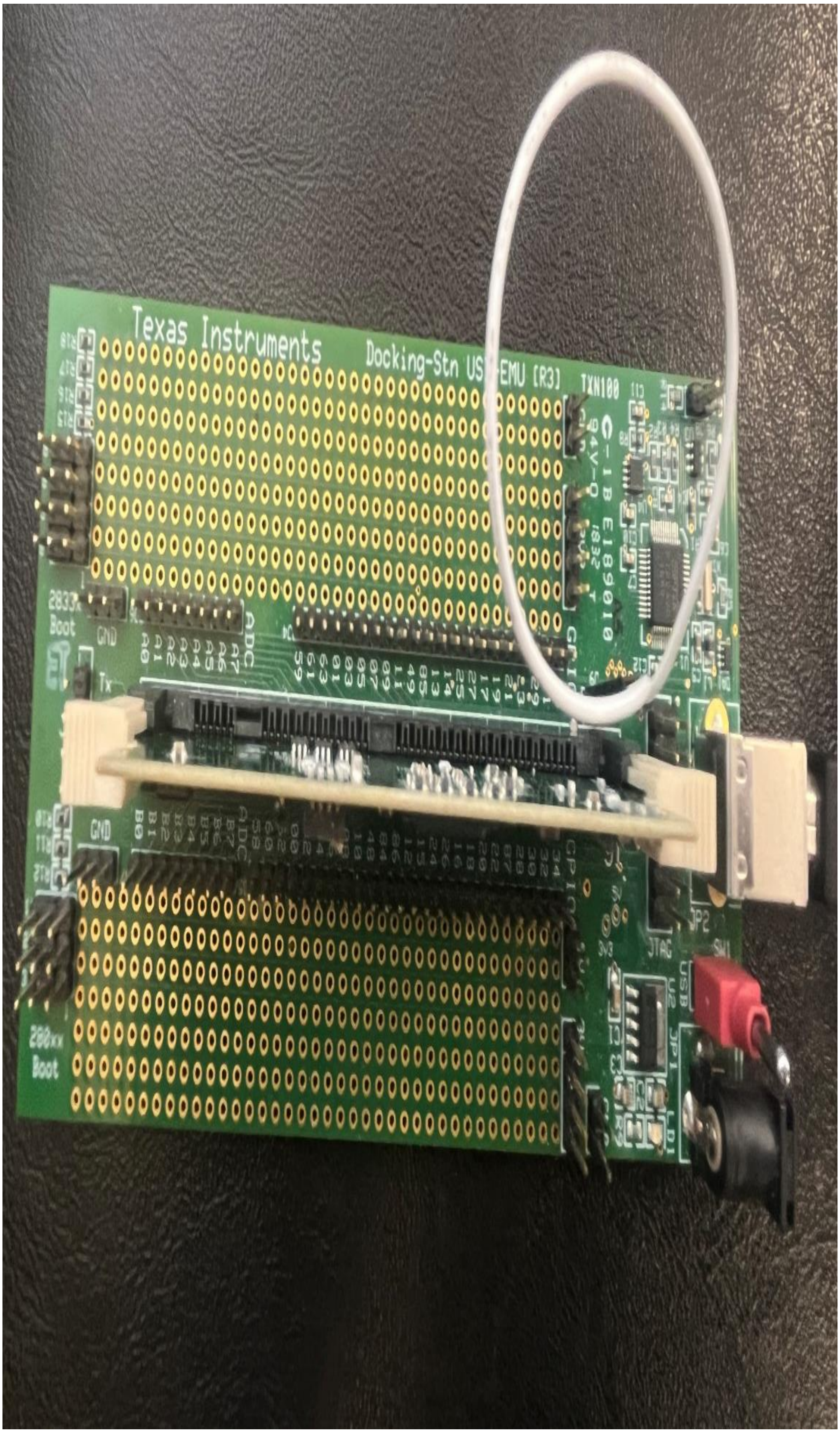

Fig C.1 Texas instrument TMS320F28335 DSP Board.

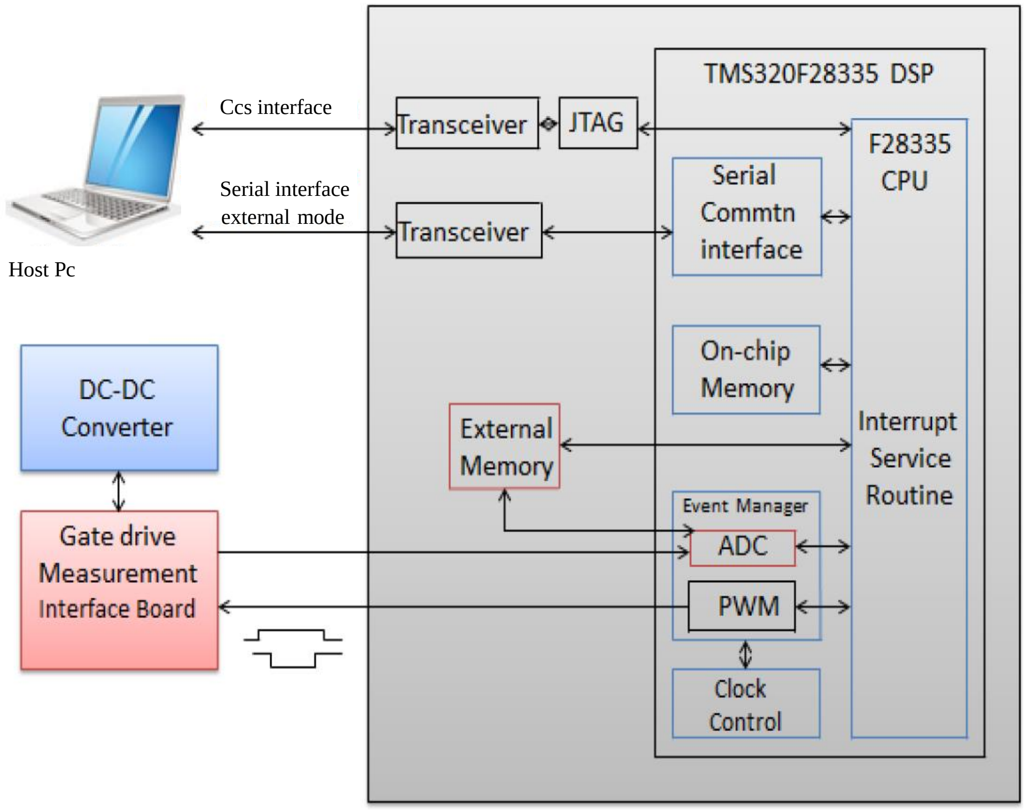

Fig C.2 Control Overview.

C.3 Software Implementation

The main codes (background loop) consist of TMS320F28335 peripheral initialisation such as PLL, PWM module, ADC module, Watchdog, and Event Manager. The entire application software is driven by a primary interrupt service routine (ISR), which contains all the control codes and is triggered from the PWM module of the DSP. The major feature of this implementation is the DSP integration to obtain the reference voltage, configuring the voltage and current loop PI controllers with anti-windup capabilities. The ISR is invoked every 20 µS (50 KHz) by the period event flag of the Event manager submodule. Timers 1 is used as the time base for the ePWM output generations with compare A and compare B sub-modules. The ADC timing is based on ADCCLK (25MHz) derived from SYSCLKOUT, and the ADCCLK is used to time the sampling period. To ensure that the samples are acquired before the commencement of the control code execution, the ADC sequencer start of conversion (SOC) is triggered on the apex of the PWM carrier. When the ADC sampling process is complete, an interrupt contains all the control codes. The flow chart of this software implementation is shown in Fig.C.3.

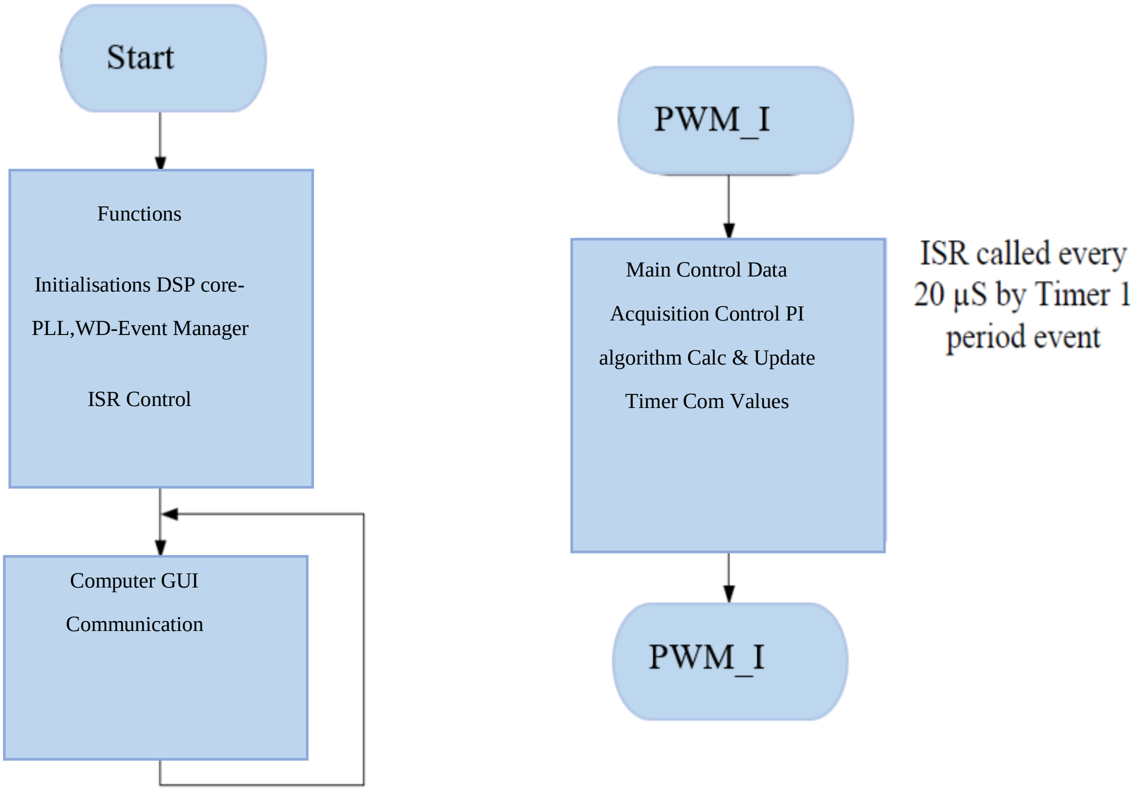

Fig C.3 Program flow chart.

Appendix D

Gate Drives and Sensors Interface Board

D.1 Introduction

The gate drive/sensors measurement board is a dedicated isolation and conditioning board, which has been specifically designed to generate appropriate gate signals required by the converter switches and also for measuring converter input current and output voltage. Furthermore, the board interfaces the spectrum digital F28335 board and hardware (power converter). A comprehensive description of this board is described in this appendix.

D.2 Gate Drive Interface

The ePWM module of F28335 (Fig.C.1) represents one complete PWM channel, each channel composed of a pair of PWM signals ePWM1A and ePWM1B, respectively. The PWM peripheral can derive up to 12 IGBTs/MOSFETs. The gate drive interface permits the DSP PWM outputs to derive the power converter switches. Two ePWM module outputs of the F28335 microcontroller are chosen; therefore, three interface circuits are provided. Each interface is for only one PWM signal. The interface caters to a single switch with a 15V power requirement. This is possible with 5-15 V DC-DC converters. Transmitting PWM signals at 15V is desirable to improve noise immunity. Fig.D.1 shows the interface boards, consisting of the gate drivers.

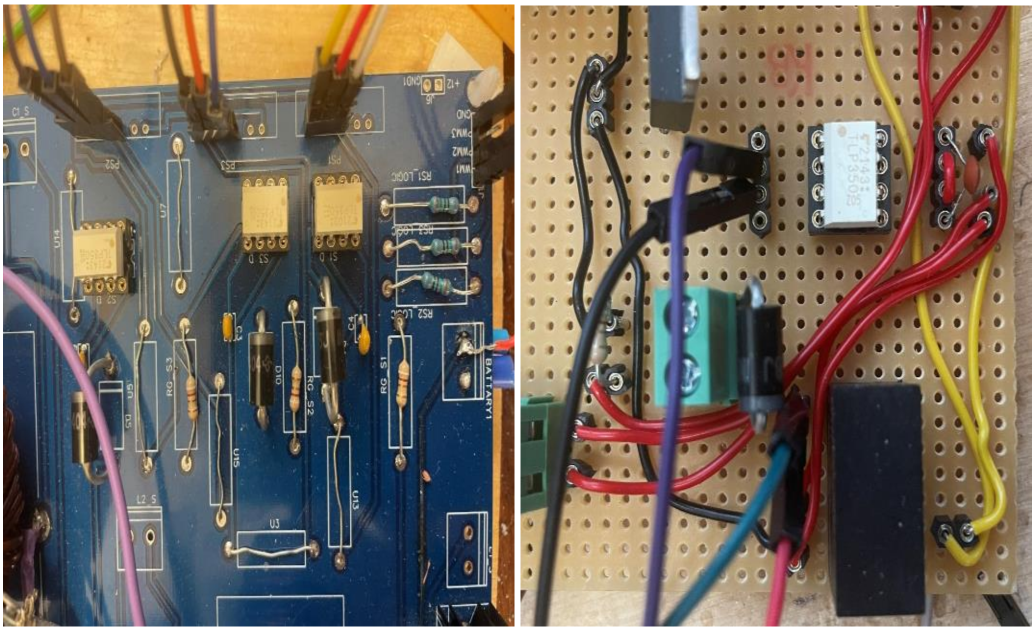

Fig D.1 Gate Drivers.

D.3 Sensor Interface

The LEM® current transducer (LA 55-P) and voltage transducer (LV-25p) are placed on board (Fig.D.2) to allow connection to the microprocessor ADC input. The current transducer is for measuring the input current flowing through the converter. The output current is an analogue voltage within the range of 0-3V with a 2.5V nominal output voltage. The transducer measures the DC input current with galvanic isolation between the power converter and the ADC circuit (primary and secondary circuit). On the other hand, the voltage transducer measures the converter's output voltage by using a load resistor to convert a current to a voltage. The voltage transducer also has galvanic isolation between the analogue and digital circuits. The sensors are positioned very close to the ADC input of the DSP board such that the track length from the sensor output to the ADC input is very short to reduce the level of noise or interference that might creep into the analogue signal.

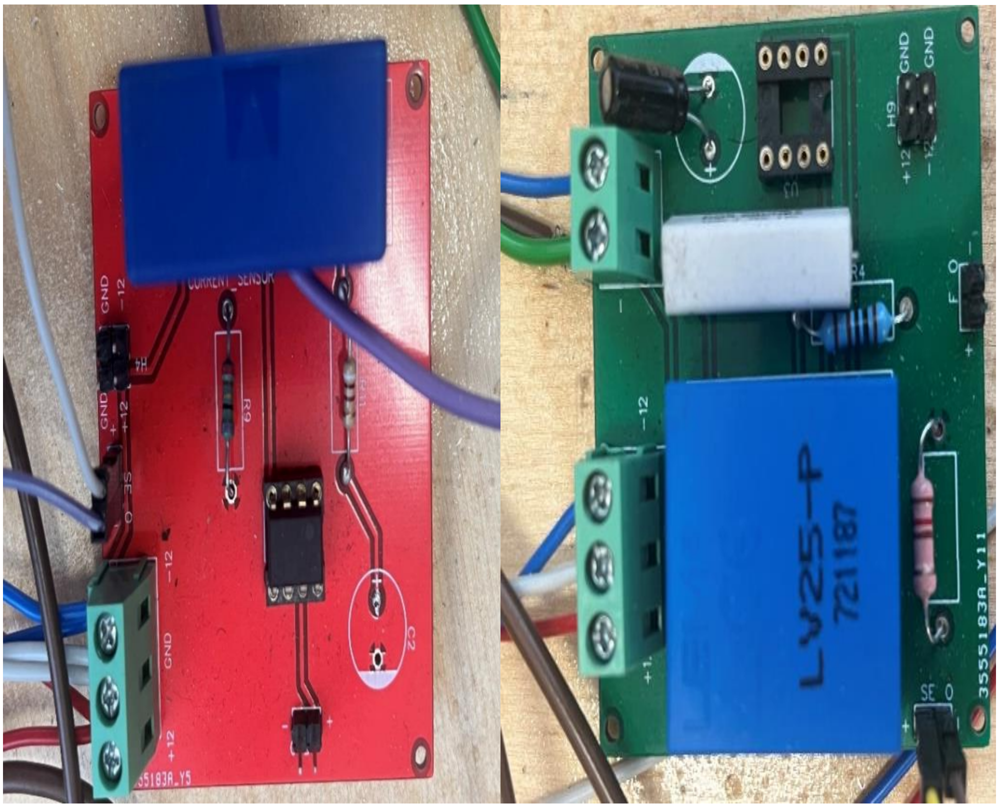

Fig D.2 Current & Voltage sensors.

Appendix E

Power Loss Analysis and Efficiency

E.1 Introduction

The losses in DC-DC converters are due to the parasitic elements inherent in the components, for example, MOSFET on-state resistance, inductor winding resistance, core loss, capacitor ESR and forward diode resistance. Unlike the ideal characteristics, in practice, these parasitic elements limit the voltage gain that a converter can produce. This behaviour is typical in boost converters. This section further illustrates the formulae used to estimate the losses regarding the components used to implement the prototypes.

E.2 Inductor Loss

To determine the converter's efficiency, it is important to calculate the power losses. To calculate the power loss, the following calculation is carried out according to [153].

Initially, Root-Mean-Square (RMS) values for inductor currents must be determined. By disregarding the ripples across the inductor currents, the RMS values are equal to their average values. According to the following formula, the inductor conduction losses can be calculated:

$$P_{\mathrm{L}}^{\mathrm{Loss}} = r_L IL^2 \qquad (E.1)$$

The inductor L and its equivalent resistance is r_L. Following this, it is necessary to determine the conduction losses of the capacitor. In order to calculate conduction losses, the following equations can be used:

$$P_{\mathrm{C}}^{\mathrm{Loss}} = r_c I c^2 \tag{E.3}$$

The equivalent resistance of the capacitor C is r_C.

E.3 Diode Conduction and Switching Losses

In addition, diode power loss should be considered. To calculate the power loss across diode, it is necessary to determine each diode's forward resistance and forward voltage. To express the power loss across the diode, the following formula can be used:

$$P_{\mathrm{D}}^{\mathrm{Loss}} = r_D \, {I_{DC}}^2 + V_{F1} \, I_{Dc} \tag{E.4}$$

It should be noted that r_{D1} is the diode equivalent resistance D_1. Moreover, V_F is the forward voltage for diode D_1 I_{DC} and represents the average diode current.

E.4 Switch Losses and Switch Conduction Losses

As explained previously, the conduction losses in MOSFET occur when the device fully conducts, and current passing through the on-state resistor RDS_on generates a power loss. The main switch conduction loss is calculated using the switch-on state resistance from the data sheet and the switch RMS current given by:

$$P_{\mathrm{S}}^{\mathrm{Loss}} = r_s I_s + \frac{1}{2} \, f_s C_s {V_Q}^2 \tag{E.5}$$

The equivalent resistance of the switch S is represented by r_S. The C_s represents the output capacitor of a metal oxide semiconductor field effect transistor.

E.5 Theoretical Efficiency

The following formula can be used to calculate the efficiency of the converter presented:

$$P_{\text{Loss}}^{\text{total}} = P_{\text{L}}^{\text{Loss}} + P_{\text{C}}^{\text{Loss}} +$$

$$+P_{\text{D}}^{\text{Loss}} + P_{\text{s}}^{\text{Loss}} \qquad (E.6)$$

$$\eta = \frac{P_{out}}{P_{out}+P_{\text{Loss}}^{\text{total}}} \qquad (E.7)$$

The efficiency of the presented converter can be calculated by substituting the equations mentioned above and simplifying them.

References

[1] S. S. Jang and J. Choi, “Energy balance analysis of small satellite in low earth orbit (LEO),” *PECon 2008 - 2008 IEEE 2nd International Power and Energy Conference*, no. PECon 08, pp. 967–971, 2008, doi: 10.1109/PECON.2008.4762613.

[2] A. Capel, “Power system of the multimedia constellation satellite for the Skybridge Missions,” *PESC Record - IEEE Annual Power Electronics Specialists Conference*, vol. 2, pp. 1913–1930, 1998, doi: 10.1109/pesc.1998.703443.

[3] A. Poghosyan and A. Golkar, “CubeSat evolution: Analyzing CubeSat capabilities for conducting science missions,” *Progress in Aerospace Sciences*, vol. 88. Elsevier Ltd, pp. 59–83, Jan. 01, 2017. doi: 10.1016/j.paerosci.2016.11.002.

[4] A. Pukniel, V. Coverstone, R. Burton, and D. Carroll, “The dynamics and control of the CubeSail mission: A solar sailing demonstration,” *Advances in Space Research*, vol. 48, no. 11, pp. 1902–1910, Dec. 2011, doi: 10.1016/j.asr.2011.07.014.

[5] J. Praks, A. Kestila, T. Tikka, H. Leppinen, O. Khurshid, and M. Hallikainen, “AALTO-1 earth observation cubesat mission - Educational outcomes,” in *International Geoscience and Remote Sensing Symposium (IGARSS)*, Institute of Electrical and Electronics Engineers Inc., Nov. 2015, pp. 1340–1343. doi: 10.1109/IGARSS.2015.7326023.

[6] R. Hevner, W. Holemans, J. Puig-Suari, and R. Twiggs, “SSC11-II-3 An Advanced Standard for CubeSats.”

[7] M. Armstrong, D. J. Atkinson, C. M. Johnson, and T. D. Abeyasekera, “Low order harmonic cancellation in a grid connected multiple inverter system via current control parameter randomization,” *IEEE Trans Power Electron*, vol. 20, no. 4, pp. 885–892, 2005, doi: 10.1109/TPEL.2005.850949.

[8] M. Armstrong, D. J. Atkinson, C. M. Johnson, and T. D. Abeyasekera, “Auto-calibrating dc link current sensing technique for transformerless, grid connected, H-bridge inverter systems,” *IEEE Trans Power Electron*, vol. 21, no. 5, pp. 1385–1393, 2006, doi: 10.1109/TPEL.2006.880267.

[9] J. T. Bialasiewicz, “Renewable energy systems with photovoltaic power generators: Operation and modeling,” *IEEE Transactions on Industrial Electronics*, vol. 55, no. 7, pp. 2752–2758, 2008, doi: 10.1109/TIE.2008.920583.

[10] K. C. Tseng, C. C. Huang, and W. Y. Shih, “A high step-up converter with a voltage multiplier module for a photovoltaic system,” *IEEE Trans Power Electron*, vol. 28, no. 6, pp. 3047–3057, 2013, doi: 10.1109/TPEL.2012.2217157.

[11] S. Green ; D.J. Atkinson ; B.C. Mecrow ; A.G. Jack ; B. Green, “Fault tolerant, variable frequency, unity power factor converters for safety critical PM drives,” *Electric Power Applications, IEE Proceedings*, pp. 663 – 672, doi: 10.1049/ip-epa:20030911.

[12] T. Dragicevic, X. Lu, J. C. Vasquez, and J. M. Guerrero, “DC Microgrids - Part I: A Review of Control Strategies and Stabilization Techniques,” *IEEE Trans Power Electron*, vol. 31, no. 7, pp. 4876–4891, 2016, doi: 10.1109/TPEL.2015.2478859.

[13] Q. Zhao and F. C. Lee, "High-efficiency, high step-up dc-dc converters," *IEEE Trans Power Electron*, vol. 18, no. 1 I, pp. 65–73, Jan. 2003, doi: 10.1109/TPEL.2002.807188.

[14] F. Crescimbini, A. Lidozzi, G. Lo Calzo, and L. Solero, "High-speed electric drive for exhaust gas energy recovery applications," *IEEE Transactions on Industrial Electronics*, vol. 61, no. 6, pp. 2998–3011, 2014, doi: 10.1109/TIE.2013.2271602.

[15] C. G. C. Branco, C. M. T. Cruz, R. P. Torrico-Bascopé, and F. L. M. Antunes, "A nonisolated single-phase UPS topology with 110-V/220-V input-output voltage ratings," *IEEE Transactions on Industrial Electronics*, vol. 55, no. 8, pp. 2974–2983, 2008, doi: 10.1109/TIE.2008.918478.

[16] R. P. Torrico-Bascopé, D. S. Oliveira, C. G. C. Branco, and F. L. M. Antunes, "A UPS with 110-V/220-V input voltage and high-frequency transformer isolation," *IEEE Transactions on Industrial Electronics*, vol. 55, no. 8, pp. 2984–2996, 2008, doi: 10.1109/TIE.2008.918480.

[17] R. Harris and R. Browning, "Renewables 2015 Global Status Report. REN21 Renewables Energy Policy Network For the 21st Century, 2015.," 2020. doi: 10.4324/9781843147824-45.

[18] W. Li and X. He, "Review of nonisolated high-step-up DC/DC converters in photovoltaic grid-connected applications," *IEEE Transactions on Industrial Electronics*, vol. 58, no. 4, pp. 1239–1250, 2011, doi: 10.1109/TIE.2010.2049715.

[19] H. S. H. Chung, N. M. Ho, W. Yan, P. W. Tam, and S. Y. Hui, "Comparison of dimmable electromagnetic and electronic ballast systems - An assessment on energy efficiency and lifetime," *IEEE Transactions on*

Industrial Electronics, vol. 54, no. 6, pp. 3145–3154, 2007, doi: 10.1109/TIE.2007.907037.

[20] M. K. Richard and P. K. Sen, “Compact fluorescent lamps and their effect on power quality and application guidelines,” *Conference Record - IAS Annual Meeting (IEEE Industry Applications Society)*, 2010, doi: 10.1109/IAS.2010.5615449.

[21] S. W. Lee and H. L. Do, “Single-stage single-switch AC-DC LED driver with high power factor,” *International Review of Electrical Engineering*, vol. 12, no. 1, pp. 4566–4576, 2017, doi: 10.15866/iree.v12i1.11098.

[22] M. A. Khan, A. Ahmed, I. Husain, Y. Sozer, and M. Badawy, “Performance Analysis of Bidirectional DC-DC Converters for Electric Vehicles,” *IEEE Trans Ind Appl*, vol. 51, no. 4, pp. 3442–3452, 2015, doi: 10.1109/TIA.2015.2388862.

[23] A. Khaligh and Z. Li, “Battery, ultracapacitor, fuel cell, and hybrid energy storage systems for electric, hybrid electric, fuel cell, and plug-in hybrid electric vehicles: State of the art,” *IEEE Trans Veh Technol*, vol. 59, no. 6, pp. 2806–2814, 2010, doi: 10.1109/TVT.2010.2047877.

[24] H. Bizhani, R. Noroozian, S. M. Muyeen, K. Techato, and F. Blaabjerg, “A Grid-Connected Smart Extendable Structure for Hybrid Integration of Distributed Generations,” *IEEE Access*, vol. 7, no. July, pp. 105235–105246, 2019, doi: 10.1109/ACCESS.2019.2931994.

[25] C. Yin, H. Li, Y. Li, W. Su, and T. Q. Zheng, “A New Family of Non-Isolated Single-Inductor Three-Port Converter Based on A Storage Port Switch-Commutated Unit,” in *2022 International Power Electronics Conference, IPEC-Himeji 2022-ECCE Asia*, Institute of Electrical and Electronics

Engineers Inc., 2022, pp. 2307–2311. doi: 10.23919/IPEC-Himeji2022-ECCE53331.2022.9807174.

[26] J. L. D. and M. A. M. H. H. Tao, A. Kotsopoulos, “Family of multiport bidirectional DC-DC converters,” *IEE Proceedings-Electric Power Applications*, vol. 150, no. 2, pp. 139–145, 2003, doi: 10.1049/ip-epa.

[27] B. G. Dobbs and P. L. Chapman, “A multiple-input DC-DC converter topology,” *IEEE Power Electronics Letters*, vol. 1, no. 1, pp. 6–9, Mar. 2003, doi: 10.1109/LPEL.2003.813481.

[28] H. Wu, Y. Xing, Y. Xia, and K. Sun, “A family of non-isolated three-port converters for stand-alone renewable power system,” *IECON Proceedings (Industrial Electronics Conference)*, vol. 3, pp. 1030–1035, 2011, doi: 10.1109/IECON.2011.6119337.

[29] M. Dhananjaya *et al.*, “Design of multi-input single output DC–DC converter with preserved output voltage under source-fault,” *IET Power Electronics*, 2023, doi: 10.1049/pel2.12488.

[30] A. K. Bhattacharjee, N. Kutkut, and I. Batarseh, “Review of Multiport Converters for Solar and Energy Storage Integration,” *IEEE Trans Power Electron*, vol. 34, no. 2, pp. 1431–1445, 2019, doi: 10.1109/TPEL.2018.2830788.

[31] H. Mahmood, D. Michaelson, and J. Jiang, “A power management strategy for PV/battery hybrid systems in Islanded microgrids,” *IEEE J Emerg Sel Top Power Electron*, vol. 2, no. 4, pp. 870–882, 2014, doi: 10.1109/JESTPE.2014.2334051.

[32] S. K. Mishra, K. K. Nayak, M. S. Rana, and V. Dharmarajan, "Switched-boost action based multiport converter," *IEEE Trans Ind Appl*, vol. 55, no. 1, pp. 964–975, 2019, doi: 10.1109/TIA.2018.2869098.

[33] N. Surulivel, D. Debnath, and C. Chakraborty, "A Novel Single Coupled-Inductor Boost TPC with Two Inductively Interfaced Ports suitable for Renewable Energy Integration," *IEEE Transactions on Industrial Electronics*, 2022, doi: 10.1109/TIE.2022.3187576.

[34] N. Zhang, D. Sutanto, and K. M. Muttaqi, "A review of topologies of three-port DC-DC converters for the integration of renewable energy and energy storage system," *Renewable and Sustainable Energy Reviews*, vol. 56, pp. 388–401, 2016, doi: 10.1016/j.rser.2015.11.079.

[35] F. Kardan, R. Alizadeh, and M. R. Banaei, "A New Three Input DC/DC Converter for Hybrid PV/FC/Battery Applications," *IEEE J Emerg Sel Top Power Electron*, vol. 5, no. 4, pp. 1771–1778, 2017, doi: 10.1109/JESTPE.2017.2731816.

[36] X. Sun, Y. Shen, W. Li, and H. Wu, "A PWM and PFM Hybrid Modulated Three-Port Converter for a Standalone PV/Battery Power System," *IEEE J Emerg Sel Top Power Electron*, vol. 3, no. 4, pp. 984–1000, 2015, doi: 10.1109/JESTPE.2015.2424718.

[37] L. An and D. D. C. Lu, "Design of a single-switch DC/DC converter for a PV-battery-powered pump system with PFM+PWM control," *IEEE Transactions on Industrial Electronics*, vol. 62, no. 2, pp. 910–921, 2015, doi: 10.1109/TIE.2014.2359414.

[38] J. Zeng, W. Qiao, and L. Qu, "An Isolated Three-Port Bidirectional DC-DC Converter for Photovoltaic Systems With Energy Storage," *IEEE Trans*

Ind Appl, vol. 51, no. 4, pp. 3493–3503, 2015, doi: 10.1109/TIA.2015.2399613.

[39] H. Wu, K. Sun, R. Chen, H. Hu, and Y. Xing, “Full-bridge three-port converters with wide input voltage range for renewable power systems,” *IEEE Trans Power Electron*, vol. 27, no. 9, pp. 3965–3974, 2012, doi: 10.1109/TPEL.2012.2188105.

[40] T. Cheng, D. D. C. Lu, and L. Qin, “Non-Isolated Single-Inductor DC/DC Converter with Fully Reconfigurable Structure for Renewable Energy Applications,” *IEEE Transactions on Circuits and Systems II: Express Briefs*, vol. 65, no. 3, pp. 351–355, 2018, doi: 10.1109/TCSII.2017.2712286.

[41] H. Zhu, D. Zhang, H. S. Athab, B. Wu, and Y. Gu, “PV isolated three-port converter and energy-balancing control method for PV-battery power supply applications,” *IEEE Transactions on Industrial Electronics*, vol. 62, no. 6, pp. 3595–3606, 2015, doi: 10.1109/TIE.2014.2378752.

[42] R. Faraji, “Soft-Switched Nonisolated High Step-Up Three-Port DC–DC Converter for Hybrid Energy Systems,” *IEEE Trans. on Power Electron.*, vol. 33, no. 12, pp. 10101–10111, 2018.

[43] M. Michon, J. L. Duarte, M. Hendrix, and M. G. Simões, “A three-port bi-directional converter for hybrid fuel cell systems,” *PESC Record - IEEE Annual Power Electronics Specialists Conference*, vol. 6, no. 2, pp. 4736–4742, 2004, doi: 10.1109/PESC.2004.1354836.

[44] X. Sun, Y. Shen, and W. Li, “A novel LLC integrated three-port DC-DC converter for stand-alone PV/battery system,” *IEEE Transportation*

Electrification Conference and Expo, ITEC Asia-Pacific 2014 - Conference Proceedings, pp. 1–6, 2014, doi: 10.1109/ITEC-AP.2014.6941090.

[45] Z. Ouyang and M. A. E. Andersen, “Integrated three-port DC-DC converter for photovoltaic (PV) battery stand-alone systems,” *PCIM Asia 2016 - International Exhibition and Conference for Power Electronics, Intelligent Motion, Renewable Energy and Energy Management*, no. June, pp. 28–30, 2016.

[46] Y. Hu, W. Xiao, W. Cao, B. Ji, and D. J. Morrow, “Three-port DC-DC converter for stand-alone photovoltaic systems,” *IEEE Trans Power Electron*, vol. 30, no. 6, pp. 3068–3076, 2015, doi: 10.1109/TPEL.2014.2331343.

[47] Y. M. Chen, A. Q. Huang, and X. Yu, “A high step-up three-port DC-DC converter for stand-alone PV/battery power systems,” *IEEE Trans Power Electron*, vol. 28, no. 11, pp. 5049–5062, 2013, doi: 10.1109/TPEL.2013.2242491.

[48] L. J. Chien, C. C. Chen, J. F. Chen, and Y. P. Hsieh, “Novel three-port converter with high-voltage gain,” *IEEE Trans Power Electron*, vol. 29, no. 9, pp. 4693–4703, 2014, doi: 10.1109/TPEL.2013.2285477.

[49] S. M. Dwari and L. Parsa, “A novel high efficiency high power interleaved coupled-inductor boost DC-DC converter for hybrid and fuel cell electric vehicle,” *VPPC 2007 - Proceedings of the 2007 IEEE Vehicle Power and Propulsion Conference*, pp. 399–404, 2007, doi: 10.1109/VPPC.2007.4544159.

[50] T. J. K. C. T. Liang;, “Analysis of integrated boost-flyback step-up converter,” *IEE Proceedings - Electric Power Applications*, vol. 152, no. 2, pp. 217 – 225, 2005, doi: 10.1049/ip-epa:20045003.

[51] A. Khaligh, J. Cao, and Y. J. Lee, “A multiple-input DC-DC converter topology,” *IEEE Trans Power Electron*, vol. 24, no. 3, pp. 862–868, 2009, doi: 10.1109/TPEL.2008.2009308.

[52] H. Wu, K. Sun, S. Ding, and Y. Xing, “Topology derivation of nonisolated three-port DC-DC converters from DIC and DOC,” *IEEE Trans Power Electron*, vol. 28, no. 7, pp. 3297–3307, 2013, doi: 10.1109/TPEL.2012.2221746.

[53] L. An and D. D. C. Lu, “Design of a single-switch DC/DC converter for a PV-battery-powered pump system with PFM+PWM control,” *IEEE Transactions on Industrial Electronics*, vol. 62, no. 2, pp. 910–921, Feb. 2015, doi: 10.1109/TIE.2014.2359414.

[54] Y. Du and D. D. C. Lu, “Battery-integrated boost converter utilizing distributed MPPT configuration for photovoltaic systems,” *Solar Energy*, vol. 85, no. 9, pp. 1992–2002, 2011, doi: 10.1016/j.solener.2011.05.008.

[55] Q. Tian, G. Zhou, M. Leng, G. Xu, X. Fan, and T. Yan, “Analysis, control, and modeling of the three-port converter without port voltage constraint for photovoltaic/battery system application,” *International Journal of Circuit Theory and Applications*, vol. 49, no. 9, pp. 2791–2811, 2021, doi: 10.1002/cta.3043.

[56] S. S. Dobakhshari, S. H. Fathi, and J. Milimonfared, “A New Soft-Switched Three-Port DC/DC Converter with High Voltage Gain and Reduced Number of Semiconductors for Hybrid Energy Applications,” *IEEE Trans*

Power Electron, vol. 35, no. 4, pp. 3590–3600, 2020, doi: 10.1109/TPEL.2019.2933182.

[57] Z. Qian, O. Abdel-Rahman, H. Al-Atrash, and I. Batarseh, “Modeling and control of three-port DC/DC converter interface for satellite applications,” *IEEE Trans Power Electron*, vol. 25, no. 3, pp. 637–649, 2010, doi: 10.1109/TPEL.2009.2033926.

[58] H. Al-Atrash, J. Reese, and I. Batarseh, “Tri-modal half-bridge converter for three-port interface,” *PESC Record - IEEE Annual Power Electronics Specialists Conference*, vol. 22, no. 1, pp. 1702–1708, 2007, doi: 10.1109/PESC.2007.4342255.

[59] Z. Qian, O. Abdel-Rahman, H. Al-Atrash, and I. Batarseh, “Modeling and control of three-port DC/DC converter interface for satellite applications,” *IEEE Trans Power Electron*, vol. 25, no. 3, pp. 637–649, 2010, doi: 10.1109/TPEL.2009.2033926.

[60] H. Wu, R. Chen, J. Zhang, Y. Xing, H. Hu, and H. Ge, “A family of three-port half-bridge converters for a stand-alone renewable power system,” *IEEE Trans Power Electron*, vol. 26, no. 9, pp. 2697–2706, 2011, doi: 10.1109/TPEL.2011.2125991.

[61] J. Zhang, H. Wu, X. Qin, and Y. Xing, “PWM Plus Secondary-Side Phase-Shift Controlled Soft-Switching Full-Bridge Three-Port Converter for Renewable Power Systems,” *IEEE Transactions on Industrial Electronics*, vol. 62, no. 11, pp. 7061–7072, 2015, doi: 10.1109/TIE.2015.2448696.

[62] Y. Lu, K. Sun, H. Wu, X. Dong, and Y. Xing, “A Three-Port Converter Based Distributed DC Grid Connected PV System with Autonomous Output

Voltage Sharing Control," *IEEE Trans Power Electron*, vol. 34, no. 1, pp. 325–339, 2018, doi: 10.1109/TPEL.2018.2822726.

[63] T. Chaudhury and D. Kastha, "A High Gain Multiport DC-DC Converter for Integrating Energy Storage Devices to DC Microgrid," *IEEE Trans Power Electron*, vol. 35, no. 10, pp. 10501–10514, 2020, doi: 10.1109/TPEL.2020.2977909.

[64] Y. Liang, "Parallel Coordination Control of Multi-Port DC-DC Converter for Stand-Alone Photovoltaic-Energy Storage Systems," *CPSS Transactions on Power Electronics and Applications*, vol. 5, no. 3, pp. 235–241, 2020, doi: 10.24295/cpsstpea.2020.00020.

[65] A. Vettuparambil, K. Chatterjee, and B. G. Fernandes, "Dual-Active-Bridge-Based Multiport Converter with Split DC Links," *IEEE Transactions on Industrial Electronics*, vol. 69, no. 1, pp. 485–494, 2022, doi: 10.1109/TIE.2021.3051576.

[66] L. Wang, Z. Wang, and H. Li, "Asymmetrical duty cycle control and decoupled power flow design of a three-port bidirectional DC-DC converter for fuel cell vehicle application," *IEEE Trans Power Electron*, vol. 27, no. 2, pp. 891–904, 2012, doi: 10.1109/TPEL.2011.2160405.

[67] D. Liu and H. Li, "A ZVS bi-directional DC-DC converter for multiple energy storage elements," *IEEE Trans Power Electron*, vol. 21, no. 5, pp. 1513–1517, 2006, doi: 10.1109/TPEL.2006.882450.

[68] C. Zhao, S. D. Round, and J. W. Kolar, "An isolated three-port bidirectional dc-dc converter with decoupled power flow management," *IEEE Trans Power Electron*, vol. 23, no. 5, pp. 2443–2453, 2008, doi: 10.1109/TPEL.2008.2002056.

[69] H. Tao, A. Kotsopoulos, J. L. Duarte, and M. A. M. Hendrix, “Transformer-coupled multiport ZVS bidirectional DC-DC converter with wide input range,” *IEEE Trans Power Electron*, vol. 23, no. 2, pp. 771–781, Mar. 2008, doi: 10.1109/TPEL.2007.915129.

[70] H. Krishnaswami and N. Mohan, “Three-port series-resonant DC-DC converter to interface renewable energy sources with bidirectional load and energy storage ports,” *IEEE Trans Power Electron*, vol. 24, no. 10, pp. 2289–2297, 2009, doi: 10.1109/TPEL.2009.2022756.

[71] H. Tao, J. L. Duarte, and M. A. M. Hendrix, “Three-port triple-half-bridge bidirectional converter with zero-voltage switching,” *IEEE Trans Power Electron*, vol. 23, no. 2, pp. 782–792, 2008, doi: 10.1109/TPEL.2007.915023.

[72] D. Liu and H. Li, “A ZVS bi-directional DC-DC converter for multiple energy storage elements,” *IEEE Trans Power Electron*, vol. 21, no. 5, pp. 1513–1517, 2006, doi: 10.1109/TPEL.2006.882450.

[73] N. D. Dao, D. C. Lee, and Q. D. Phan, “High-Efficiency SiC-Based Isolated Three-Port DC/DC Converters for Hybrid Charging Stations,” *IEEE Trans Power Electron*, vol. 35, no. 10, pp. 10455–10465, 2020, doi: 10.1109/TPEL.2020.2975124.

[74] X. Tang, H. Wu, W. Hua, Z. Yu, and Y. Xing, “Three-Port Bidirectional Series-Resonant Converter with First-Harmonic-Synchronized PWM,” *IEEE J Emerg Sel Top Power Electron*, vol. 9, no. 2, pp. 1410–1419, Apr. 2021, doi: 10.1109/JESTPE.2020.2975164.

[75] J. Asakura and H. Akagi, “State-of-Charge (SOC)-Balancing Control of a Battery Energy Storage System Based on a Cascade PWM Converter,”

IEEE Trans Power Electron, vol. 24, no. 6, pp. 1628–1636, 2009, doi: 10.1109/TPEL.2009.2014868.

[76] R. Y. Kim and J. S. Lai, “Aggregated modeling and control of a boost-buck cascade converter for maximum power point tracking of a thermoelectric generator,” *Conference Proceedings - IEEE Applied Power Electronics Conference and Exposition - APEC*, pp. 1754–1760, 2008, doi: 10.1109/APEC.2008.4522964.

[77] B.-R. J.-J. C. Lin;, “Analysis and implementation of a soft switching converter with high-voltage conversion ratio,” *IET Power Electronics*, vol. 1, no. 3, pp. 386 – 394, 2008, doi: 10.1049/iet-pel:20070315.

[78] S. Y. Tseng, S. H. Tseng, and J. Z. Shiang, “High step-up converter associated with soft-switching circuit with partial energy processing for livestock stunning applications,” *Conference Proceedings - IPEMC 2006: CES/IEEE 5th International Power Electronics and Motion Control Conference*, vol. 2, pp. 1086–1090, 2007, doi: 10.1109/IPEMC.2006.297237.

[79] Y. M. Ye and K. W. E. Cheng, “Quadratic boost converter with low buffer capacitor stress,” *IET Power Electronics*, vol. 7, no. 5, pp. 1162–1170, 2014, doi: 10.1049/iet-pel.2013.0205.

[80] G. Palumbo and D. Pappalardo, “Charge pump circuits: An overview on design strategies and topologies,” *IEEE Circuits and Systems Magazine*, vol. 10, no. 1, pp. 31–45, Mar. 2010, doi: 10.1109/MCAS.2009.935695.

[81] K. W. E. Cheng, “New generation of switched capacitor converters,” *PESC Record - IEEE Annual Power Electronics Specialists Conference*, vol. 2, no. c, pp. 1529–1535, 1998, doi: 10.1109/pesc.1998.703377.

[82] F. L. Luo and H. Ye, “Positive output super-lift converters,” *IEEE Trans Power Electron*, vol. 18, no. 1 I, pp. 105–113, 2003, doi: 10.1109/TPEL.2002.807198.

[83] M. D. Seeman and S. R. Sanders, “Analysis and optimization of switched-capacitor DC-DC converters,” *IEEE Trans Power Electron*, vol. 23, no. 2, pp. 841–851, Mar. 2008, doi: 10.1109/TPEL.2007.915182.

[84] B. Axelrod, Y. Berkovich, and A. Ioinovici, “Switched-capacitor/switched-inductor structures for getting transformerless hybrid DC-DC PWM converters,” *IEEE Transactions on Circuits and Systems I: Regular Papers*, vol. 55, no. 2, pp. 687–696, 2008, doi: 10.1109/TCSI.2008.916403.

[85] A. Alateeq, Y. Almalaq, and M. Matin, “A switched-inductor model for a non-isolated multilevel boost converter,” *2017 North American Power Symposium, NAPS 2017*, 2017, doi: 10.1109/NAPS.2017.8107406.

[86] L. S. Yang, T. J. Liang, and J. F. Chen, “Transformerless DC-DC converters with high step-up voltage gain,” *IEEE Transactions on Industrial Electronics*, vol. 56, no. 8, pp. 3144–3152, 2009, doi: 10.1109/TIE.2009.2022512.

[87] Y. Tang, D. Fu, T. Wang, and Z. Xu, “Hybrid switched-inductor converters for high step-up conversion,” *IEEE Transactions on Industrial Electronics*, vol. 62, no. 3, pp. 1480–1490, Mar. 2015, doi: 10.1109/TIE.2014.2364797.

[88] T. Wang and Y. Tang, “Study of active network DC-DC boost converter based on switched-inductor,” *Diangong Jishu Xuebao/Transactions of China Electrotechnical Society*, vol. 29, no. 12, pp. 73–79, 2014.

[89] C. M. Lai and Y. H. Liao, “Modeling, analysis, and design of an interleaved four-phase current-fed converter with new voltage multiplier topology,” *IEEE Trans Ind Appl*, vol. 49, no. 1, pp. 208–222, 2013, doi: 10.1109/TIA.2012.2227643.

[90] Y. Zhao, X. Xiang, C. Li, Y. Gu, W. Li, and X. He, “Single-phase high step-up converter with improved multiplier cell suitable for half-bridge-based PV inverter system,” *IEEE Trans Power Electron*, vol. 29, no. 6, pp. 2807–2816, 2014, doi: 10.1109/TPEL.2013.2273975.

[91] R. J. Wai, C. Y. Lin, C. Y. Lin, R. Y. Duan, and Y. R. Chang, “High-efficiency power conversion system for kilowatt-level stand-alone generation unit with low input voltage,” *IEEE Transactions on Industrial Electronics*, vol. 55, no. 10, pp. 3702–3714, 2008, doi: 10.1109/TIE.2008.921251.

[92] H. L. Do, “Improved ZVS DC-DC converter with a high voltage gain and a ripple-free input current,” *IEEE Transactions on Circuits and Systems I: Regular Papers*, vol. 59, no. 4, pp. 846–853, 2012, doi: 10.1109/TCSI.2011.2169741.

[93] W. Li, W. Li, Y. Deng, and X. He, “Single-stage single-phase high-step-up ZVT boost converter for fuel-cell microgrid system,” *IEEE Trans Power Electron*, vol. 25, no. 12, pp. 3057–3065, 2010, doi: 10.1109/TPEL.2010.2079955.

[94] T. J. Liang, S. M. Chen, L. S. Yang, J. F. Chen, and A. Ioinovici, “Ultra-large gain step-up switched-capacitor DC-DC converter with coupled inductor for alternative sources of energy,” *IEEE Transactions on Circuits and Systems I: Regular Papers*, vol. 59, no. 4, pp. 864–874, 2012, doi: 10.1109/TCSI.2011.2169886.

[95] Y. P. Hsieh, J. F. Chen, T. J. Liang, and L. S. Yang, “Novel high step-up DC-DC converter with coupled-inductor and switched-capacitor techniques for a sustainable energy system,” *IEEE Trans Power Electron*, vol. 26, no. 12, pp. 3481–3490, 2011, doi: 10.1109/TPEL.2011.2160876.

[96] S. M. Chen, T. J. Liang, L. S. Yang, and J. F. Chen, “A boost converter with capacitor multiplier and coupled inductor for AC module applications,” *IEEE Transactions on Industrial Electronics*, vol. 60, no. 4, pp. 1503–1511, 2013, doi: 10.1109/TIE.2011.2169642.

[97] X. Hu and C. Gong, “A high voltage gain DC-DC converter integrating coupled-inductor and diode-capacitor techniques,” *IEEE Trans Power Electron*, vol. 29, no. 2, pp. 789–800, 2014, doi: 10.1109/TPEL.2013.2257870.

[98] G. C. Silveira, F. L. Tofoli, L. D. S. Bezerra, and R. P. Torrico-Bascope, “A nonisolated DC-DC boost converter with high voltage gain and balanced output voltage,” *IEEE Transactions on Industrial Electronics*, vol. 61, no. 12, pp. 6739–6746, 2014, doi: 10.1109/TIE.2014.2317136.

[99] F. L. Tofoli, D. De Souza Oliveira, R. P. Torrico-Bascopé, and Y. J. A. Alcazar, “Novel nonisolated high-voltage gain DC-DC converters based on 3SSC and VMC,” *IEEE Trans Power Electron*, vol. 27, no. 9, pp. 3897–3907, 2012, doi: 10.1109/TPEL.2012.2190943.

[100] M. Muhammad, B. Eng, and M. Eng, “High Gain Non-isolated DC-DC Converter Topologies for Energy Conversion Systems,” 2017. Accessed: May 12, 2023. [Online]. Available: http://hdl.handle.net/10443/3665

[101] Y. Song and B. Wang, “Survey on reliability of power electronic systems,” *IEEE Trans Power Electron*, vol. 28, no. 1, pp. 591–604, 2013, doi: 10.1109/TPEL.2012.2192503.

[102] W. Zhang, D. Xu, P. N. Enjeti, H. Li, J. T. Hawke, and H. S. Krishnamoorthy, “Survey on fault-tolerant techniques for power electronic converters,” *IEEE Trans Power Electron*, vol. 29, no. 12, pp. 6319–6331, 2014, doi: 10.1109/TPEL.2014.2304561.

[103] M. Rahnama, A. Vahedi, A. M. Alikhani, N. Takorabet, and B. Fazelbakhsheshi, “A novel diode open circuit fault detection in three phase rectifier based on k-means method,” in *Proceedings of the IEEE International Conference on Industrial Technology*, Institute of Electrical and Electronics Engineers Inc., Apr. 2018, pp. 600–605. doi: 10.1109/ICIT.2018.8352246.

[104] W. Li, W. Li, Y. Deng, and X. He, “Single-stage single-phase high-step-up ZVT boost converter for fuel-cell microgrid system,” *IEEE Trans Power Electron*, vol. 25, no. 12, pp. 3057–3065, 2010, doi: 10.1109/TPEL.2010.2079955.

[105] A. Khaligh, A. M. Rahimi, and A. Emadi, “Modified pulse-adjustment technique to control DC/DC converters driving variable constant-power loads,” *IEEE Transactions on Industrial Electronics*, vol. 55, no. 3, pp. 1133–1146, 2008, doi: 10.1109/TIE.2007.909757.

[106] I. Jiya, A. M. S. Ali, H. Khang, N. Kishor, and R. Ciric, “Novel Multisource DC-DC Converter for All-Electric Hybrid Energy Systems,” *IEEE Transactions on Industrial Electronics*, vol. 69, no. 12, pp. 12934–12945, Dec. 2022, doi: 10.1109/TIE.2021.3131871.

[107] S. M. Hashemzadeh, V. Marzang, S. Pourjafar, and S. Hossein Hosseini, “An Ultra High Step-Up Dual-Input Single-Output DC-DC Converter Based on Coupled Inductor,” *IEEE Transactions on Industrial Electronics*, vol. 69, no. 11, pp. 11023–11034, Nov. 2022, doi: 10.1109/TIE.2021.3123636.

[108] F. Blaabjerg, Z. Chen, and S. B. Kjaer, “Power electronics as efficient interface in dispersed power generation systems,” *IEEE Trans Power Electron*, vol. 19, no. 5, pp. 1184–1194, 2004, doi: 10.1109/TPEL.2004.833453.

[109] Z. Chen, J. M. Guerrero, and F. Blaabjerg, “A review of the state of the art of power electronics for wind turbines,” *IEEE Trans Power Electron*, vol. 24, no. 8, pp. 1859–1875, 2009, doi: 10.1109/TPEL.2009.2017082.

[110] L. Kunjuramakurup, S. M. Sulthan, M. S. Ponparakkal, V. Raj, and M. Sathyajith, “A High-Power Solar PV-fed TISO DC-DC Converter for Electric Vehicle Charging Applications,” *Energies (Basel)*, vol. 16, no. 5, Mar. 2023, doi: 10.3390/en16052186.

[111] L. W. Zhou, B. X. Zhu, and Q. M. Luo, “High step-up converter with capacity of multiple input,” *IET Power Electronics*, vol. 5, no. 5, pp. 524–531, 2012, doi: 10.1049/iet-pel.2011.0177.

[112] L. Kumar and S. Jain, “A novel dual input DC/DC converter topology,” in *PEDES 2012 - IEEE International Conference on Power Electronics, Drives and Energy Systems*, 2012. doi: 10.1109/PEDES.2012.6484424.

[113] F. Akar, Y. Tavlasoglu, E. Ugur, B. Vural, and I. Aksoy, “A Bidirectional Nonisolated Multi-Input DC-DC Converter for Hybrid Energy Storage

Systems in Electric Vehicles," *IEEE Trans Veh Technol*, vol. 65, no. 10, pp. 7944–7955, Oct. 2016, doi: 10.1109/TVT.2015.2500683.

[114] L. Solero, A. Lidozzi, and J. A. Pomilio, "Design of multiple-input power converter for hybrid vehicles," *IEEE Trans Power Electron*, vol. 20, no. 5, pp. 1007–1016, Sep. 2005, doi: 10.1109/TPEL.2005.854020.

[115] A. Hintz, U. R. Prasanna, and K. Rajashekara, "Novel Modular Multiple-Input Bidirectional DC-DC Power Converter (MIPC) for HEV/FCV Application," *IEEE Transactions on Industrial Electronics*, vol. 62, no. 5, pp. 3163–3172, May 2015, doi: 10.1109/TIE.2014.2371778.

[116] J. Qi and D. D. C. Lu, "A Preventive Approach for Solving Battery Imbalance Issue by Using a Bidirectional Multiple-Input Cuk Converter Working in DCVM," *IEEE Transactions on Industrial Electronics*, vol. 64, no. 10, pp. 7780–7789, Oct. 2017, doi: 10.1109/TIE.2017.2696497.

[117] M. Marchesoni and C. Vacca, "New dc-dc converter for energy storage system interfacing in fuel cell hybrid electric vehicles," *IEEE Trans Power Electron*, vol. 22, no. 1, pp. 301–308, Jan. 2007, doi: 10.1109/TPEL.2006.886650.

[118] B. Wang, X. Zhang, and H. B. Gooi, "An SI-MISO Boost Converter with Deadbeat-Based Control for Electric Vehicle Applications," *IEEE Trans Veh Technol*, vol. 67, no. 10, pp. 9223–9232, Oct. 2018, doi: 10.1109/TVT.2018.2853738.

[119] H. Zhang, D. Dong, M. Jing, W. Liu, and F. Zheng, "Topology Derivation of Multiple-Port DC-DC Converters Based on Voltage-Type Ports," *IEEE Transactions on Industrial Electronics*, vol. 69, no. 5, pp. 4742–4753, May 2022, doi: 10.1109/TIE.2021.3078389.

[120] C. A. Hill, M. C. Such, D. Chen, J. Gonzalez, and W. M. K. Grady, “Battery energy storage for enabling integration of distributed solar power generation,” *IEEE Trans Smart Grid*, vol. 3, no. 2, pp. 850–857, 2012, doi: 10.1109/TSG.2012.2190113.

[121] S. Rostami, V. Abbasi, N. Talebi, and T. Kerekes, “Three-port DC–DC converter based on quadratic boost converter for stand-alone PV/ battery systems,” *IET Power Electronics*, vol. 13, no. 10, pp. 2106–2118, Aug. 2020, doi: 10.1049/iet-pel.2019.1025.

[122] Q. Tian, G. Zhou, R. Liu, X. Zhang, and M. Leng, “Topology Synthesis of a Family of Integrated Three-Port Converters for Renewable Energy System Applications,” *IEEE Transactions on Industrial Electronics*, vol. 68, no. 7, pp. 5833–5846, Jul. 2021, doi: 10.1109/TIE.2020.2994864.

[123] K. Alluhaybi, I. Batarseh, and H. Hu, “Comprehensive Review and Comparison of Single-Phase Grid-Tied Photovoltaic Microinverters,” *IEEE J Emerg Sel Top Power Electron*, vol. 8, no. 2, pp. 1310–1329, Jun. 2020, doi: 10.1109/JESTPE.2019.2900413.

[124] M. Al-soeidat, “Solar Power Generation Capability and Three-Port Converters for PV-Battery Powered Applications,” 2020.

[125] G. Chen, Z. Jin, Y. Liu, Y. Hu, J. Zhang, and X. Qing, “Programmable Topology Derivation and Analysis of Integrated Three-Port DC-DC Converters with Reduced Switches for Low-Cost Applications,” *IEEE Transactions on Industrial Electronics*, vol. 66, no. 9, pp. 6649–6660, 2019, doi: 10.1109/TIE.2018.2877159.

[126] S. H. Hosseini, S. K. Haghighian, S. Danyali, and H. Aghazadeh, “Multi-input dc boost converter supplied by a hybrid PV/Wind turbine power

systems for street lighting application connected to the grid,” *Proceedings of the Universities Power Engineering Conference*, 2012, doi: 10.1109/UPEC.2012.6398632.

[127] H. Zhu, D. Zhang, B. Zhang, and Z. Zhou, “A Nonisolated Three-Port DC-DC Converter and Three-Domain Control Method for PV-Battery Power Systems,” *IEEE Transactions on Industrial Electronics*, vol. 62, no. 8, pp. 4937–4947, 2015, doi: 10.1109/TIE.2015.2393831.

[128] S. Arun, T. P. Imthias Ahamed, and Z. V. Lakaparampil, “A SEPIC-based three-port converter system using a mode-specific power flow management control for solar energy harvesting,” *Renewable Energy Focus*, vol. 44, pp. 56–74, 2023, doi: 10.1016/j.ref.2022.09.009.

[129] V. Indragandhi and A. Benitto, “Performance analysis, modeling and control of multi-port DC-DC boost converter for an integrated power generation system,” *Indian J Sci Technol*, vol. 9, no. 36, 2016, doi: 10.17485/ijst/2016/v9i36/96985.

[130] H. Wu, K. Sun, S. Ding, and Y. Xing, “Topology derivation of nonisolated three-port DC-DC converters from DIC and DOC,” *IEEE Trans Power Electron*, vol. 28, no. 7, pp. 3297–3307, 2013, doi: 10.1109/TPEL.2012.2221746.

[131] S. Rostami, V. Abbasi, N. Talebi, and T. Kerekes, “Three-port DC–DC converter based on quadratic boost converter for stand-alone PV/ battery systems,” *IET Power Electronics*, vol. 13, no. 10, pp. 2106–2118, 2020, doi: 10.1049/iet-pel.2019.1025.

[132] X. Liu and X. Wu, “A two-stage bidirectional DC-DC converter system and its control strategy,” *Energy*, vol. 266, Mar. 2023, doi: 10.1016/j.energy.2022.126462.

[133] R. V. Damodaran, H. Shareef, K. S. Phani Kiranmai, and R. Errouissi, “Two-Switch Boost Converter with Improved Voltage Gain and Degree of Freedom of Control,” *IEEE Access*, 2023, doi: 10.1109/ACCESS.2023.3249107.

[134] K. N. Thirukkuralkani, K. Srinivasan, and V. Karthikeyan, “A single switch hybrid quadratic converter for grid-integrated renewable energy system,” *International Journal of Circuit Theory and Applications*, 2023, doi: 10.1002/cta.3631.

[135] W. Liu and H. Zhang, “Cycle Skipping-Induced Bifurcation Analysis of Single-Inductor Bipolar-Output DC-DC Converters with One-Cycle Control,” *IEEE Transactions on Circuits and Systems II: Express Briefs*, 2023, doi: 10.1109/TCSII.2023.3248179.

[136] N. Zhang, G. Zhang, K. W. See, and B. Zhang, “A single-switch quadratic buck-boost converter with continuous input port current and continuous output port current,” *IEEE Trans Power Electron*, vol. 33, no. 5, pp. 4157–4166, 2018, doi: 10.1109/TPEL.2017.2717462.

[137] H. Farsizadeh, M. Gheisarnejad, M. Mosayebi, M. Rafiei, and M. H. Khooban, “An Intelligent and Fast Controller for DC/DC Converter Feeding CPL in a DC Microgrid,” *IEEE Transactions on Circuits and Systems II: Express Briefs*, vol. 67, no. 6, pp. 1104–1108, 2020, doi: 10.1109/TCSII.2019.2928814.

[138] S. Saravanan and N. Ramesh Babu, “Analysis and implementation of high step-up DC-DC converter for PV based grid application,” *Appl Energy*, vol. 190, pp. 64–72, 2017, doi: 10.1016/j.apenergy.2016.12.094.

[139] P. K. Maroti, S. Padmanaban, P. Wheeler, F. Blaabjerg, and M. Rivera, “Modified high voltage conversion inverting cuk DC-DC converter for renewable energy application,” *Proceedings - 2017 IEEE Southern Power Electronics Conference, SPEC 2017*, vol. 2018-Janua, pp. 1–5, 2018, doi: 10.1109/SPEC.2017.8333675.

[140] M. R. Banaei, H. Ardi, and A. Farakhor, “Analysis and implementation of a new single-switch buck-boost DC/DC converter,” *IET Power Electronics*, vol. 7, no. 7, pp. 1906–1914, 2014, doi: 10.1049/iet-pel.2013.0762.

[141] T. Jalilzadeh, E. Babaei, and M. Maalandish, “Generalized nonisolated high step-up DC-DC converter with reduced voltage stress on devices,” *International Journal of Circuit Theory and Applications*, vol. 46, no. 11, pp. 2053–2078, 2018, doi: 10.1002/cta.2506.

[142] T. Jalilzadeh, N. Rostami, E. Babaei, and M. Maalandish, “Ultra-step-up DC-DC converter with lowvoltage stress on devices,” *IET Power Electronics*, vol. 12, no. 3, pp. 345–357, 2019, doi: 10.1049/iet-pel.2018.5356.

[143] M. K. Nguyen, Y. C. Lim, J. H. Choi, and G. B. Cho, “Isolated High Step-Up DC-DC Converter Based on Quasi-Switched-Boost Network,” *IEEE Transactions on Industrial Electronics*, vol. 63, no. 12, pp. 7553–7562, 2016, doi: 10.1109/TIE.2016.2586679.

[144] S. Zhou, G. Zhou, X. Liu, and H. Zhao, “Dynamic Freewheeling Control for SIDO Buck Converter With Fast Transient Performance, Minimized

Cross-Regulation, and High Efficiency," *IEEE Transactions on Industrial Electronics*, vol. 70, no. 2, pp. 1467–1477, Feb. 2023, doi: 10.1109/TIE.2022.3156169.

[145] G. Chen *et al.*, "Topology derivation and analysis of integrated multiple output isolated DC-DC converters with stacked configuration for low-cost applications," *IEEE Transactions on Circuits and Systems I: Regular Papers*, vol. 64, no. 8, pp. 2207–2218, 2017, doi: 10.1109/TCSI.2017.2683506.

[146] N. Surulivel, D. Debnath, and C. Chakraborty, "A Novel Bi-directional Four-Port DC-DC Converter suitable for Bipolar DC Solar Household Integration," *IEEE Trans Power Electron*, 2023, doi: 10.1109/TPEL.2023.3249339.

[147] M. Azizi, M. Mohamadian, and R. Beiranvand, "A New Family of Multi-Input Converters Based on Three Switches Leg," *IEEE Transactions on Industrial Electronics*, vol. 63, no. 11, pp. 6812–6822, 2016, doi: 10.1109/TIE.2016.2581765.

[148] L. Kumar and S. Jain, "A multiple source DC/DC converter topology," *International Journal of Electrical Power and Energy Systems*, vol. 51, pp. 278–291, 2013, doi: 10.1016/j.ijepes.2013.02.020.

[149] H. Wu, K. Sun, L. Zhu, and Y. Xing, "An Interleaved Half-Bridge Three-Port Converter With Enhanced Power Transfer Capability Using Three-Leg Rectifier for Renewable Energy Applications," *IEEE J Emerg Sel Top Power Electron*, vol. 4, no. 2, pp. 606–616, 2016, doi: 10.1109/JESTPE.2015.2478140.

[150] K. Suresh *et al.*, “A Multifunctional Non-Isolated Dual Input-Dual Output Converter for Electric Vehicle Applications,” *IEEE Access*, vol. 9, pp. 64445–64460, 2021, doi: 10.1109/ACCESS.2021.3074581.

[151] Z. Qian, O. Abdel-Rahman, H. Al-Atrash, and I. Batarseh, “Modeling and control of three-port DC/DC converter interface for satellite applications,” *IEEE Trans Power Electron*, vol. 25, no. 3, pp. 637–649, 2010, doi: 10.1109/TPEL.2009.2033926.

[152] Q. Tian, G. Zhou, H. Li, Y. Yang, and D. Zhou, “Symmetrical Bipolar Output Isolated Four-Port Converters Based on Center-Tapped Winding for Bipolar DC Bus Applications,” *IEEE Trans Power Electron*, vol. 37, no. 2, pp. 2338–2351, Feb. 2022, doi: 10.1109/TPEL.2021.3107154.

[153] M. K. Kazimierczuk, *Pulse-width modulated DC-DC power converters*, Second edition. Chichester, West Sussex, [England: Wiley, 2016.